

**Luminescence investigation of trivalent rare earth ions in sol-gel derived SiO₂
and ZnO co-doped SiO₂:Pr³⁺.**

By

Gugu Hlengiwe Mhlongo

(MSc)

A thesis submitted in fulfillment of the requirements for the degree

PHILOSOPHIAE DOCTOR

in the

Faculty of Natural and Agricultural Sciences

Department of Physics

at the

University of Free State

Promoters: Prof. K.T. Hillie and Prof. O.M. Ntwaeaborwa

May 2011

ACKNOWLEDGEMENTS

- First and foremost, I would like to thank *God*, for giving me courage and strength during these years.
- I am deeply grateful to both my promoters, *Prof. O. M. Ntwaeaborwa* and *Prof. K. T. Hillie* for their brilliant academic guidance, encouragement, and support which made this work meaningful and a success.
- I would also like to express my sincere appreciation to *Prof H.C. Swart* for his professional support and suggestions. Most importantly I thank him for being always available whenever I needed help with the CL and AES measurements.
- I would also like to extend my deep appreciation to *Dr M.S. (Simon) Dhlamini* for his constructive discussions in this research.
- I thank *Mart-Mari Duvenhage* and *Pontsho Mbule* for their assistance and support they gave me at the UFS.
- Many thanks to the Nano-Centre staff at CSIR for their inspiration and continued support. I'm grateful to *Dr Bonex Mwakhikhunga* for his physics discussions.
- I gratefully thank *Dr R.E. Kroon* for analyzing some of the samples using synchrotron radiation in Germany.
- I'm deeply grateful to the SUPERLUMI experimental station at HASYLAB, DESY, in Germany for giving us the beam time to conduct some luminescence analysis using synchrotron radiation.
- Many thanks to *Dr Marek Guwoski* for introducing me to his former supervisor Prof. W. Ryba-Romanowski at the Institute of Low Temperature and Structure Research, in Poland.

- I also thank *Prof. W. Ryba-Romanowski* and *Dr Piotr Solarz* for assisting with the luminescence decay measurements. Above all, I thank *Piotr* for helping me with the decay curves fittings.
- I would like to extend my gratitude to my former school principal *Mr and Mrs Khambule* of *Kwa-Nxusa Secondary School* for their encouragement and inspiration.
- My special thanks to my husband to be *Sibongiseni* and our daughter *Londeka Ndimande*, for their understanding and encouragement during these years. My sincere appreciation to my parents, brothers and sisters for their moral support.
- Great thanks to both *Dept. of Science and Technology (DST)* and the *Council for Scientific and Industrial Research (CSIR)* of South Africa for funding this project.

ABSTRACT

Tb^{3+} - Pr^{3+} , Ce^{3+} - Pr^{3+} , and Eu^{3+} - Pr^{3+} ion pairs co-doped in SiO_2 were successfully synthesized using a sol gel method to produce rare earth activated oxide nanophosphors. Green emitting ZnO nanoparticles were also successfully embedded into single doped Pr^{3+} in SiO_2 matrix resulting in a red emitting $\text{ZnO}:\text{SiO}_2:\text{Pr}^{3+}$ nanocomposite. The phosphor powders were produced by drying the precursor gels at room temperature followed by annealing at 600 °C in ambient air.

Based on the X-ray diffraction results, it was found that the SiO_2 was amorphous regardless of the incorporation of Pr^{3+} , Ce^{3+} , Tb^{3+} , Eu^{3+} ions and nanocrystalline ZnO or annealing at 600 °C. The particle morphology of powder phosphors was observed from field emission scanning electron microscopy and high resolution transmission electron microscope images.

The field emission scanning electron microscopy revealed that the particles of the synthesized phosphors were mostly spherical and agglomerated. In addition, the morphology and distribution of SiO_2 nanoparticles were not influenced by the presence of different rare affected by the presence of rare-earth ions in the matrix. The high resolution transmission electron microscope on the other hand confirmed the homogenous dispersion of the rare-earth ions incorporated in the amorphous SiO_2 matrix. The presence of these ions in SiO_2 host was confirmed by the energy dispersive X-ray spectroscopy.

The energy transfer from ZnO to Pr^{3+} which was evidenced by quenching of green emission from ZnO resulting in an enhanced red emission from Pr^{3+} under both low electron beam and vacuum ultra violet excitation was demonstrated. For Pr^{3+} - Ce^{3+} ion pair, the red emission from Pr^{3+} was slowly quenched while that from Ce^{3+} was

slightly enhanced with increasing Ce^{3+} concentration. Such results indicate the energy transfer from Pr^{3+} to Ce^{3+} . In the case of $\text{SiO}_2:\text{Tb}^{3+}/\text{Eu}^{3+}$ co-doped with Pr^{3+} , the cathodoluminescence and photoluminescence intensities of $\text{Pr}^{3+}-\text{Tb}^{3+}$ and $\text{Pr}^{3+}-\text{Tb}^{3+}$ were strongly quenched with Pr^{3+} co-doping.

We also investigated the effect of beam voltage and current on the cathodoluminescence intensity from the powder phosphors as well as their cathodoluminescence intensity degradation under prolonged electron bombardment in the cathodoluminescence spectroscopy.

KEYWORDS

Energy transfer, cathodoluminescence, photoluminescence, phosphor degradation, concentration quenching.

ACRONYMS

PL	Photoluminescence
CL	Cathodoluminescence
HRTEM	High resolution transmission electron microscope
FESEM	Field emission scanning electron microscope
FTIR	Fourier transform infrared spectroscopy
XRD	X-Ray diffraction
APPHs	Auger peak-to-peak heights
EDS	Energy dispersive X-ray spectroscopy
TGA	Thermogravimetric analysis
UV-VIS	Ultra violet visible spectroscopy
VUV	Vacuum ultra violet

TABLE OF CONTENTS

ACKNOWLEDGEMENTS	ii
ABSTRACT	iv
KEYWORDS	v
ACRONYMS	v
LIST OF FIGURES	x
CHAPTER 1	1
INTRODUCTION	1
1.1 OVERVIEW	1
1.2 RESEARCH CHALLENGES	3
1.3 STUDY OBJECTIVES	4
1.4 SCOPE AND THESIS OUTLINE	5
1.5 REFERENCES	6
CHAPTER 2	9
INTRODUCTION	9
2.1 Trivalent rare earth ions	9
2.2 Semiconductor nanocrystals ‘quantum dots’	10
2.3 Application of phosphors	11
2.3.1 Field emission display (FEDs) technology	12
2.3.2 Plasma display panels (PDPs)	12
2.3.3 Basic aspects of luminescence	13
2.3.4 Cathodoluminescence (CL)	15
2.3.5 CL generation	15
2.3.6 Electron beam-phosphor interaction	16
2.3.7 CL intensity degradation in phosphor materials	18
2.3.8 Killer centres	19
2.3.9 Concentration quenching	19
2.3.10 Brightness saturation	20

2.3.11 Thermal quenching _____	20
2.3.12 Electron Stimulated Surface Chemical Reaction _____	21
2.4 Photoluminescence (PL) _____	22
2.4.1 Intrinsic luminescence _____	23
2.4.2 Extrinsic luminescence _____	23
2.5 Energy transfer process in rare earth phosphors _____	25
2.5.1 Theory of energy transfer _____	26
2.5.2 Phonon-assisted energy transfer _____	30
2.5.3 Cross-relaxation _____	31
2.5.4 Migration of excitation energy _____	31
2.6 REFERENCES _____	33
CHAPTER 3 _____	37
MATERIALS CHARACTERIZATION _____	37
3.1 INTRODUCTION _____	37
3.2 CHARACTERIZATION TECHNIQUES _____	37
3.2.1 X-Ray diffraction, XRD _____	37
3.2.2 Scanning electron microscopy, SEM _____	39
3.2.3 Transmission electron microscopy, TEM _____	40
3.2.4 Thermogravimetric analysis, TGA _____	41
3.2.5 UV-VIS spectroscopy _____	42
3.2.6 Fourier Transform Infrared (FT-IR) spectroscopy _____	43
3.2.7 Auger Electron Spectroscopy, AES _____	44
3.2.8 Photoluminescence, PL analysis _____	45
3.3 REFERENCES _____	48
CHAPTER 4 _____	49
CL PROPERTIES OF SiO₂:Pr³⁺ AND ZnO.SiO₂:Pr³⁺ NANOPOWDER	
PHOSPHORS _____	49
4.1 INTRODUCTION _____	49
4.2 EXPERIMENTAL _____	50
4.2.1 Sample preparation by sol-gel method _____	50

4.3	RESULT AND DISCUSSION	51
4.3.1	Sample structure (XRD)	51
4.3.2	Sample morphology (FESEM)	53
4.3.3	Thermal Analysis, TGA	54
4.3.4	Optical absorption and emission properties	55
4.3.5	CL degradation	65
4.4	CONCLUSION	70
4.5	REFERENCES	71
CHAPTER 5		73
	LUMINESCENCE DEPENDENCE OF Pr³⁺ ACTIVATED SiO₂ NANOPHOSPHOR ON Pr³⁺ CONCENTRATION, TEMPERATURE AND ZnO INCORPORATION	73
5.1	INTRODUCTION	73
5.2	EXPERIMENTAL	74
5.3	RESULT AND DISCUSSION	74
5.3.1	Particle morphology (HRTEM)	74
5.3.2	PL properties of Pr ³⁺ singly doped SiO ₂	77
5.4	Energy transfer from ZnO nanoparticles to Pr ³⁺ ions in SiO ₂ .	83
5.5	CONCLUSION	88
5.6	REFERENCES	90
CHAPTER 6		92
	EFFECTS OF Ce³⁺ CONCENTRATION, BEAM VOLTAGE AND CURRENT ON THE CL INTENSITY OF SiO₂:Pr³⁺-Ce³⁺ NANOPHOSPHOR	92
6.1	INTRODUCTION	92
6.2	EXPERIMENTAL	92
6.3	RESULT AND DISCUSSION	94
6.4	CONCLUSION	106
6.5	REFERENCES	107

CHAPTER 7	109
THE INFLUENCE OF Pr³⁺ CO-DOPING ON THE PL AND CL PROPERTIES OF SiO₂:Eu³⁺/Tb³⁺	109
7.1 INTRODUCTION	109
7.2 EXPERIMENTAL	109
7.2.1 Preparation of SiO ₂ : Tb ³⁺ -Pr ³⁺ and SiO ₂ : Eu ³⁺ -Pr ³⁺	109
7.3 RESULT AND DISCUSSION	111
7.3.1 Phase and structure analysis (XRD)	111
7.3.2 Elemental analysis (EDS)	111
7.3.2 PL properties of SiO ₂ :Eu ³⁺ -Pr ³⁺ and SiO ₂ :Tb ³⁺ -Pr ³⁺	112
7.3.3 CL properties of SiO ₂ : Eu ³⁺ -Pr ³⁺ and SiO ₂ : Tb ³⁺ -Pr ³⁺	120
7.4 CONCLUSION	123
7.5 REFERENCES	124
CHAPTER 8	125
SUMMARY AND CONCLUSSION	125
FUTURE PROSPECTS	127
PUBLICATIONS	128
INTERNATIONAL CONFERENCES	129
NATIONAL CONFERENCES	130

LIST OF FIGURES

Fig. 2.1: Interactions among photon, electron, and phonon: photon absorption and emission, electron excitation and decay, and phonon emission.	14
Fig. 2.2 Schematic representation of emission process in CL [22].....	17
Fig. 2.3 Electron beam penetrating a phosphor material as a function of increasing beam voltages (i.e. $A < B < C$) [20].	17
Fig. 2.4 Configurational coordinate model of a luminescent centre in a host matrix [40].	21
Fig. 2.5 Intra-atomic luminescence transitions within Eu^{3+} ion.	25
Fig. 2.6 Resonant energy transfer by the quantum mechanical exchange interaction in which the overlapping of the wavefunctions of D and A (shaded area) is considered.	27
Fig. 2.7 Coulomb interaction in a resonant energy transfer process.	29
Fig. 2.8 Phonon-assisted non-radiative transfer; ϵ is the energy mismatch.	31
Fig. 3.1 Schematic of the system for XRD measurements [1].	38
Fig. 3.2 Schematic diagram of SEM [3].	40
Fig. 3.3 Schematic diagram of HRTEM [4].	41
Fig. 3.4 Schematic diagram of TGA [5].	42
Fig.3.5 Simplified optical layout of a typical double-beam UV-Vis Spectrophotometry.	43
Fig. 3.6 Simplified layout of the FTIR system showing line path to the ATR mode.	44
Fig. 3.7 Schematic diagram of Auger spectroscopy.	45
Fig. 3.8 Block diagram of fluorescence spectroscopy.	46
Fig. 3.9 Schematic representation of the Side view of SUPERLUMI setup [5].	47
Fig. 4.1 XRD patterns of the ZnO nanoparticles and microparticles.	52
Fig.4.2 XRD patterns of SiO_2 nanoparticles, $\text{SiO}_2:\text{Pr}^{3+}$ and $\text{ZnO}:\text{SiO}_2:\text{Pr}^{3+}$ nanophosphor powders calcined at 600°C for 2hrs.	52
Fig.4.3 HRSEM images of (a) SiO_2 , (b) Pr^{3+} doped SiO_2 , and $\text{ZnO}:\text{SiO}_2:\text{Pr}^{3+}$ nanophosphor powders.	53
Fig.4.4 TGA curves of un-doped SiO_2 , $\text{SiO}_2:\text{Pr}^{3+}$ and $\text{ZnO}:\text{SiO}_2:\text{Pr}^{3+}$ phosphor gels. The samples were heated from 50°C to 950°C in N_2 atmosphere at a heating rate of $10^\circ\text{C}/\text{min}$	55
Fig. 4.5 UV-VIS absorption spectra of SiO_2 , ZnO, $\text{SiO}_2:\text{Pr}^{3+}$, and $\text{ZnO}:\text{SiO}_2:\text{Pr}^{3+}$...	56

Fig. 4.6 PL emission spectra of ZnO nanoparticles and ZnO microparticles.....	57
Fig. 4.7 CL spectra of un-doped SiO ₂ , SiO ₂ :Pr ³⁺ and ZnO.SiO ₂ :Pr ³⁺ irradiated with 2 kV, 20 μA beam of electrons in a high vacuum chamber containing 1.6 x 10 ⁻⁸ Torr.	59
Fig. 4.8 Schematic representation of energy levels diagram depicting mechanism of energy transfer from ZnO nanoparticles and possible transitions in Pr ³⁺ doped in SiO ₂	61
Fig. 4.9 CL spectra of SiO ₂ :Pr ³⁺ irradiated with (1-5 kV), 8.5 μA beam of electrons in a high vacuum chamber containing a base pressure of ~ 1.6 x 10 ⁻⁸ Torr.	62
Fig.4. 10 Maximum CL intensity of SiO ₂ :Pr ³⁺ 614 nm emission peak as a function of accelerating voltage	62
Fig.4.11 CL spectra of ZnO.SiO ₂ :Pr ³⁺ irradiated with (1-5 kV), 8.5 μA beam of electrons in a high vacuum chamber containing a base pressure of ~1.6 x 10 ⁻⁸ Torr.	63
Fig. 4.12Maximum CL intensity of ZnO.SiO ₂ :Pr ³⁺ 614 nm emission peak at different electron beam voltages.....	64
Fig 4.13 CL spectra of (a) SiO ₂ :Pr ³⁺ and (b) ZnO.SiO ₂ :Pr ³⁺ before and after electron bombardment by 2 kV, 20 μA in 1 x 10 ⁻⁷ Torr of O ₂	67
Figure 4.14AES spectra of (a) SiO ₂ :Pr ³⁺ and (b) ZnO.SiO ₂ :Pr ³⁺ before and after degradation at 2 kV, 20 μA, in 1 x 10 ⁻⁷ Torr of O ₂	68
Figure 4.15 AES peak-to-peak heights of (a) SiO ₂ :Pr ³⁺ and (b) ZnO.SiO ₂ :Pr ³⁺ at 2 kV, 20 μA, in 1 x 10 ⁻⁷ Torr of O ₂ as a function of electron dose.	69
Fig. 5.1 (a) TEM and (b) HRTEM images of the clustered ZnO nanoparticles	75
Fig. 5.2 TEM images of (a) SiO ₂ nanoparticles, (b) ZnO.SiO ₂ :Pr ³⁺ nanophosphor and the insert of HRTEM image of ZnO.SiO ₂ :Pr ³⁺	76
Fig. 5.3 Energy dispersive X-Ray spectrum of 1 mol% ZnO.SiO ₂ :0.2 mol% Pr ³⁺ phosphor.....	76
Fig. 5.4 VUV excitation spectrum and emission spectrum of 0.2 mol% Pr ³⁺ single doped SiO ₂	79
Fig. 5.5 Luminescence decay curves of the ³ P ₀ and ¹ D ₂ levels of Pr ³⁺ (0.2 mol%) in SiO ₂ obtained at 8 K. The solid black line corresponds to the experimental data and the solid red line is the fit to a single exponential.	80
Fig. 5.6 Luminescence decay curves of the ¹ D ₂ → ³ H ₄ emission for various concentrations of Pr ³⁺ (0.2 mol%) in SiO ₂	82

Fig. 5.7 Lifetimes of the $^1D_2 \rightarrow ^3H_4$ transition of Pr^{3+} (0.2 mol%) doped in SiO_2 plotted against the temperature in the 8-300 K regions.....	83
Fig. 5.8 PL emission spectra of $SiO_2:Pr^{3+}$ and $ZnO:SiO_2:Pr^{3+}$ after VUV excitation at 90 nm using synchrotron radiation.	84
Fig. 5.9 PL excitation spectra of $SiO_2:Pr^{3+}:0.2$ mol% with and without ZnO nanophosphors monitoring the emission peak at 605 nm.	85
Fig. 5.10 Luminescence decay curves of (a) $SiO_2:Pr^{3+}$, $ZnO:SiO_2:Pr^{3+}$ nanophosphors and (b) ZnO nanocrystals.	87
Fig. 5.11 Schematic energy level diagram showing the transition localized within Pr^{3+} ions and ZnO nanopartilces.	88
Fig. 6.1 HRTEM images of (a) SiO_2 nanoparticles, $SiO_2:Pr^{3+}$, and (b) $SiO_2:Pr^{3+}-Ce^{3+}$ and EDS spectra of (d) $SiO_2:Pr^{3+}$, and (e) $SiO_2:Pr^{3+}-Ce^{3+}$	95
Fig. 6.2 FTIR absorption spectra of SiO_2 , $SiO_2:Pr^{3+}$, $SiO_2:Ce^{3+}$, $SiO_2:Pr^{3+}-Ce^{3+}$ phosphor powders.	96
Fig. 6.3 CL emission spectra of SiO_2 nanoparticles irradiated with 2 kV, 8.5 μA beam of electrons in a high vacuum chamber containing 1.2×10^{-8} Torr.	97
Fig. 6.4 CL emission spectrum of $SiO_2:Ce^{3+}$ after irradiation with 2 kV, 8.5 μA beam of electrons in a high vacuum chamber containing a base pressure of 1.2×10^{-8} Torr.	98
Fig. 6.5 CL emission spectra of the $SiO_2:Pr^{3+}$ (1 mol %), $SiO_2:Ce^{3+}$ (1 mol %), and $SiO_2:Pr^{3+} - Ce^{3+}$ (0.2, 1, 1.5, 2 mol %) irradiated with 2 kV, 8.5 μA beam of electrons in a high vacuum chamber containing a base pressure of 1.2×10^{-8} Torr. The insert shows the CL intensity as a function of different Ce^{3+} concentrations.	100
Fig. 6.6 Schematic energy level diagram showing the transition localized within Pr^{3+} and Ce^{3+} ions.	101
Fig. 6.7 CL emission intensities of Ce^{3+} in $SiO_2: Pr^{3+}-Ce^{3+}$ phosphor as a function of different beam voltages.	102
Fig. 6.8 CL emission intensities of Ce^{3+} in $SiO_2: Pr^{3+}-Ce^{3+}$ phosphor as a function of different beam currents.	103
Fig. 6.9 The calculated penetration depth as a function of electron beam voltage.	104

Fig. 6.10 CL emission spectra of SiO ₂ :Pr ³⁺ ,Ce ³⁺ powder phosphors before and after exposure to 2 kV, 8.5 μA electrons in 1x10 ⁻⁷ Torr of O ₂ backfilled from the base pressure of 1.2 x10 ⁻⁸ Torr.	105
Fig. 6.11 Auger peak-to-peak heights of O and Si versus 2 kV electron dose at 1x10 ⁻⁷ Torr O ₂ backfilled from the base pressure of 1.2 x10 ⁻⁸ Torr.	105
Fig. 7.1 EDS spectra of (a) SiO ₂ :1 mol% Eu ³⁺ - 0.2 mol% Pr ³⁺ and (b) SiO ₂ :1 mol% Tb ³⁺ - 0.2 mol% Pr ³⁺	112
Fig.7.2 Emission spectra of SiO ₂ :1 mol% Eu ³⁺ and SiO ₂ :1 mol% Eu ³⁺ -0.2 mol% Pr ³⁺ nanophosphors after excitation at 395 nm at room temperature using a Xenon lamp.....	114
Fig. 7.3 Excitation spectra of SiO ₂ :1 mol% Eu ³⁺ and SiO ₂ :1 mol% Eu ³⁺ -0.2 mol% Pr ³⁺ after monitoring the emission peak at 614 nm at room temperature.	115
Fig. 7.4 Emission spectra of SiO ₂ :1 mol% Tb ³⁺ and SiO ₂ :1 mol% Tb ³⁺ -0.2 mol% Pr ³⁺ nanophosphor powders obtained after excitation at 379 nm at room temperature.....	116
Fig. 7.5 Excitation spectra of SiO ₂ :1 mol% Tb ³⁺ and SiO ₂ :1 mol% Tb ³⁺ -0.2 mol% Pr ³⁺ obtained after monitoring Tb ³⁺ emission at 543 nm at room temperature.	117
Fig. 7.6 Decay curves for the ⁵ D ₄ - ⁷ F ₅ transition of Tb ³⁺ in SiO ₂ for 0.2, 0.5, and 1 mol% concentrations of Pr ³⁺ while the Tb ³⁺ concentration was kept at 0.2 mol%.....	119
Fig. 7.7 CL spectra of SiO ₂ :1 mol% Tb ³⁺ , and SiO ₂ : 1 mol%Tb ³⁺ -0.2 mol% Pr ³⁺ samples irradiated with 2kV, 20μA beam of electrons in a high vacuum chamber containing a base pressure of ~ 1.6 x 10 ⁻⁸ Torr. The insert shows the CL intensity from SiO ₂ : Pr ³⁺ -Tb ³⁺ as a function of 0.2, 0.5, and 1 mol% Pr ³⁺ concentrations.....	120
Fig. 7.8 CL intensities of SiO ₂ :1 mol% Eu ³⁺ -0.2 mol% Pr ³⁺ and SiO ₂ :0.2 mol% Pr ³⁺ at 2kV, 20μA in 1x10 ⁻⁷ Torr, O ₂ as a function of electron dose. The insert shows the CL intensity from SiO ₂ :Pr ³⁺ -Eu ³⁺ as a function of 0.2, 0.5, and 1 mol% Pr ³⁺ concentrations.....	122

CHAPTER 1

INTRODUCTION

1.1 OVERVIEW

Considerable improvement in the field of phosphors has been made by intentionally introducing trivalent rare earth ions as luminescent centres in different host matrices to make rare earth activated phosphors [1-4]. Over the past years, rare earth based phosphors have played a key role on the operation and success of many lighting and display devices [5-8] in the lighting industry. Cathode-ray tube (CRT) screens and liquid-crystal display (LCD) are the most common display devices. However, conventional CRTs are too bulky and heavy while the LCDs are restricted by a small viewing angle and by a slow response [9-13]. Field emissive display (FED) is regarded as an excellent model of flat panel display (FPD) technology for the next generation of display technology due to their anticipated high brightness, high contrast ratio, light weight, and low-power consumption [5,13]. Plasma display panel (PDP) is another example of FPD technology which is unlike LCD as it provide a rapid response and large viewing angle for large TV displays [6,10-13] and they have dominated the display market in the last decade. Also, PDPs operate differently from FEDs, which utilize electrons to excite phosphors, since they use high-energy plasma discharge to generate UV photons that excites PDP phosphors [14-22].

The phosphor layer which consists of red (R), green (G), and blue (B) emitting rare earth phosphors serves as a crucial component in many display technologies including FEDs and PDPs [10,23]. For instance, commercial phosphor layers used in FEDs are $Y_2O_3:Eu^{3+}$ (red), $Y_3Al_5O_{12}:Tb^{3+}$ (green), and $Y_2SiO_5:Ce^{3+}$ (blue).

Numerous synthetic approaches used to prepare oxide based phosphor materials have been reported [17,24-28]. However, sol-gel method is preferable since it is relatively inexpensive, provides good control of particle size, uniform morphology, and high homogeneity. Different glasses have been used as hosts for rare earth ions to prepare phosphors using the sol-gel method [3,29,30]. Among these glasses, sol-gel derived Silica (SiO_2) glasses are regarded as good porous host matrices for metal ions or rare earth ions [29,31,32] to prepare nano or micron structured phosphors. These glasses can also encapsulate semiconductor nanoparticles such as ZnO [33], PbS [34], and CdS [35] to make light emitting nano-composites. SiO_2 has therefore emerged as a good host for rare earth ions due to its high transparency, chemical stability, dopant solubility and ease of production [36].

Trivalent rare earth ions can be co-doped in a glassy SiO_2 matrix for enhanced emission of light as a result of energy transfer from one ion to the other. For example, Yun et al [37] observed the emission intensity of Eu^{3+} in the Eu^{3+} - Tb^{3+} co-doped SiO_2 phosphor to be four times more than that of the Eu^{3+} singly doped phosphor. This was attributed to energy transfer from Tb^{3+} to Eu^{3+} . Energy transfer was also reported by Ntwaeaborwa et al [36] between Ce^{3+} and Tb^{3+} in SiO_2 . Also, if semiconductor nanocrystals “quantum dots” are incorporated into rare earth activated glass matrix, energy can be transferred from the quantum dots to luminescent centres resulting in enhanced luminescence due to sensitizing effects of the quantum dots. Yu et al [38], Bang et al [33] and Hayakawa et al [39] reported enhanced luminescence efficiency due to energy transfer between ZnO and CdS to Eu^{3+} doped SiO_2 , respectively.

1.2 RESEARCH CHALLENGES

An overwhelming contribution to the development of rare earth activated phosphors for possible application in FEDs and PDPs has been successfully made [1-3,5,7,8,17,19,25,27]. Even though microsized traditional sulphide phosphors for FEDs have demonstrated high luminous efficiency and high chromaticity [1,9,40] they are still faced with one major challenge that their CL intensity degrades drastically under standard operating conditions (low voltage and high current densities) required for FEDs. It has also been indicated that desorption of sulfur and formation of non-luminescent oxide layers on the surface takes place simultaneously with the CL intensity degradation [41-43]. Research focus has now shifted to nanosized oxide phosphors which are emerging as possible candidates to replace microsized traditional sulphide phosphors. The main reason for such interest on oxide nanophosphors is that they have demonstrated high chemical and high thermodynamic stability under high current densities, high-vacuum pressures as well as elevated temperatures [44].

Despite the fact that PDPs are currently commercially available, there are still some problems that must be solved which hinder their performance. One of them is that phosphors tend to degrade under strong energetic VUV photons excitation. In addition, the phosphors brightness has been found to slightly decrease when a PDP is in operation as the plasma directly bombards the electrodes and phosphor. This has been found to result on the contamination of a phosphor by outgassing from the barrier rib and the other layers of the device which then leads to further phosphor degradation reducing the lifetime of the display [10]. In order to improve the panel luminous efficiency, both the luminous efficiency of phosphors and the discharge

VUV production efficiency must be increased since the luminescence of many phosphors remarkably decrease under a strong excitation energy exposure [10,19].

In search for oxide phosphors with high luminous efficiency and yet stable under standard operating conditions of both PDPs and FEDs, researchers have explored energy transfer between the semiconductor nanoparticles and rare earth ions co-doped in a same matrix. Energy transfer between a pair of non-identical trivalent rare earth ions has also been an interesting topic lately. This is regarded as the most important and attractive way of improving the luminescence efficiency of the rare earth activated oxide phosphor. Considering the fact that improvements over the past years have yielded phosphor materials with improved quantum yield [10,20-22,45], these phosphors have not yet been perfected hence further development is still required. Moreover, a deep insight into their intensity degradation including the mechanisms involved still need to be investigated further.

1.3 STUDY OBJECTIVES

- To investigate the CL properties of $\text{ZnO.SiO}_2:\text{Pr}^{3+}$ and the luminescence dependence of $\text{SiO}_2:\text{Pr}^{3+}$ on Pr^{3+} concentration, annealing temperature, and ZnO incorporation.
- Study the effects of Ce^{3+} concentration, beam voltage and current on the CL intensity of $\text{SiO}_2:\text{Pr}^{3+}-\text{Ce}^{3+}$.
- Study the influence of Pr^{3+} co-doping on the CL and PL properties of SiO_2 doped Eu^{3+} and Tb^{3+} .
- Investigate the degradation of $\text{SiO}_2:\text{Pr}^{3+}$, $\text{ZnO.SiO}_2:\text{Pr}^{3+}$, and $\text{SiO}_2:\text{Pr}^{3+}-\text{Ce}^{3+}$ nanophosphor powders.

1.4 SCOPE AND THESIS OUTLINE

Chapter 2 provides background information on trivalent rare earth ions, semiconductor nanocrystals, and luminescence processes including CL and PL which are discussed in detail as they are the basis for this study. Detailed information on energy transfer mainly in rare earth activated phosphors is also provided in this chapter.

Chapter 3 provides a summary of characterization techniques that were used in this study.

Cathodoluminescence properties of $\text{SiO}_2:\text{Pr}^{3+}$ and $\text{ZnO}:\text{SiO}_2:\text{Pr}^{3+}$ nanophosphor powders synthesized by sol-gel method are discussed in *chapter 4*.

In *chapter 5*, luminescence dependence of Pr^{3+} activated SiO_2 nanophosphor on Pr^{3+} concentration, temperature, and ZnO incorporation are presented.

Chapter 6 deals with the dependence of Ce^{3+} concentration, beam voltage and current on the CL intensity of $\text{SiO}_2:\text{Pr}^{3+}-\text{Ce}^{3+}$ nanophosphor.

Chapter 7 presents the results on influence of Pr^{3+} co-doping on the PL and CL properties of $\text{SiO}_2:\text{Eu}^{3+}/\text{Tb}^{3+}$ emission.

Chapter 8 is about concluding remarks on the overall study and suggestions for possible future studies.

1.5 REFERENCES

- [1] P. Psuja, D. Hreniak, and W. Strek, *J. Nanomater.* 81350 (2007)
- [2] H. L. Li, Z. L. Zhang, and J. H. Hao, *Mater. Sci. Eng. 1* (2009) 012010
- [3] G. Lakshminarayana, J. Qiu, *J. Alloys Compd.* 476 (2009) 470-476
- [4] E. J Bosze, G. A. Hirata, L. E. Shea-Rohwer, J. McKittrick, *J. Lumin.* 104 (2003) 47-54
- [5] C.R Ronda, T. Justel, H. Nikol, *J. Alloys Compd.* 669 (1998) 275-277
- [6] M. T. Anderson, R. J. Walko, and M. L. F. Phillips, Phosphors for flat panel emissive displays, *97th Annual Meeting of the American Ceramic Society* (1995)
- [7] L. Q. Minh, W. Strek, T. K. Anh, and K. Yu, *J. Nanomater.* 48312 (2007)
- [8] M. Nazarov, J. H. Kang, D. Y. Jeon, S. Bukesov, T. Akmaeva, *Opt. Mater.* 27 (2005) 1587–1592
- [9] L. E. Shea, *Electrochem. Soc. Interface- Summer* (1998)
- [10] J-H. Lee, D .N. Liu, S-T. Wu, Introduction to Flat Panel Displays, *John Wiley & Sons: Chichester* (2008)
- [11] L. E. Tannas, W. E. Glenn, and J. W. Doane, Flat-Panel Display Technologies, *Noyes Publications: New Jersey* (1995)
- [12] S. Y. Shionoya, W.M. Yen, Phosphor Handbook, *CRC Press LLC: Boca Raton, Florida* (1999)
- [13] A. A Talian, K. A. Dean, J. E. Jaskie, *Solid State Electron.* 45 (2001) 963-976
- [14] C. Ronda, *J. Lumin.* 72-74 (1997) 49-54
- [15] E. van der Kolk, P. Dorenbos, and C. W. E. Van Eijk, *J. Phys.: Condens. Matter.* 13 (2001) 5471-5486

- [16] X.-J. Wang, S. Huang, L. Lu, W. M. Yen, A. M. Srivastava, A. A. Setlur, *Opt. Comm.* 195 (2001) 405-410
- [17] L. Bo, S. Chau-Shu, Q. Ze-Ming, T. Ye, *Chin. Phys. Lett.* 22 (2005) 2677
- [18] Fujitsu General America, Incl., Plasma Display Panel vs Liquid Crystal Display, An Overview of Consumer Benefits for Home Theater Applications (2003)
- [19] C. Ozakazi, M. Shiiki, T. Suzuki, K. Suzuki, *J. Lumin.* 87-89 (2000) 1280-1282
- [20] Z. Zhang, Y. Wang, J. Zhang, *Mater. Lett.* 62 (2008) 846-848
- [21] C.-H. Kim, H. Eok Kwon, C.-H. Park, Y.-J. Hwang, H.-S. Bae, B.-Y. Yu, C.-H. Pyun, G.-Y. Hong, *J. Alloys Compd.* 311 (2000) 33-39
- [22] T. Jüstel, H. Nikol, and C. Ronda, *Angew. Chem. Int. Ed.* 37 (1998) 3084 -3103
- [23] C. E. Hunt, and A. G. Chakhovski, *J. Vac. Sci. Technol. B* 15[2] (1997) 516-519
- [24] Q.Y. Zhang, X.Y. Huang, *Prog. Mater. Sci.* 55 (2010) 353-427
- [25] Q. Pang, J. Shi, and M. Gong, *J. Am. Ceram. Soc.*, 90 [12] (2007) 3943-3946
- [26] A. Biswas, H.N. Acharya, *Mater. Res. Bull.* 32, [11] (1997) 1551-1557
- [27] H. Yang, Y.-S. Kim, *J. Lumin.* 128 (2008) 1570-1576
- [28] Y.C. Kang, S.B. Park, I.W. Lenggoro, K. Okuyama, *J. Phys. Chem. Sol.* 60 (1999) 379-384
- [29] M. Fassoli, A. Vedda, A. Lauria, F. Moretti, E. Rizzelli, N. Chiodini, F. Meinardi, M. Nikil, *J. Non-Cryst. Solids* 355 (2009) 1140-1144
- [30] A. Ravi Kumar, N. Veeraiah, B. Appa Rao, *J. Lumin.* 75 (1997) 57-62
- [31] C. F Song, M. K. Lu, P. Yang, D. Xu, D. R. Yuan, G. J. Zhou, F. Gu, *Mater. Sci. & Eng.* B97 (2003) 64-67
- [32] W. Streck, J. Legendziewicz, E. Lukowiak, K. Maruszewski, J. Sokolnicki, A.A. Boiko, M. Borzechowska, *Spectrochim. Acta Part A* 54 (1998) 2215-2221
- [33] J. Bang, H. Yang, and P.H. Holloway, *J. Chem. Phys.* 123 (2005) 084709

- [34] M. S. Dhlamini, J.J. Terblans, O.M. Ntwaeaborwa and H.C. Swart, *Surf. Rev. Lett.* 14 [4] (2007) 697-701
- [35] R. Reisfeld, M. Gaft, T. Saridarov, G. Panczer, M. Zelner, *Mater. Lett.* 45 (2000) 154-156
- [36] O. M. Ntwaeaborwa, H. C. Swart, R. E. Kroon, P. H. Holloway, J. R. Botha, *J. Chem. Phys. Sol.* 67 (2006) 1749-1753
- [37] H. X. Yun, F. J. Jun, Z. Dekani, B. J. Tao, R. Z. Yu, H. Xun, *Chin. Sci. Bull.* 52 (2007) 444-449
- [38] Y. Yu, Y. Wang, D. Chen, P. Huang, E. Ma, F. Bao, *J. Nanotechnol.* 2008, 19, 055711
- [39] T. Hayakawa, S. T. Selvan, M. Nogami, *J. Sol-Gel Sci. Tech.* 19 (2000) 779-783
- [40] S. Tan, P. Yang, C. Li, W. Wang, J. Wang, M. Zhang, X. Jing, J. Lin, *Solid State Sci.* 12 (2010) 624-629
- [41] H. C. Swart, L. Oosthuizen, P. H. Holloway, G. L. P. Berning. *Surf. Interface Anal.* 26 (1998) 337-342
- [42] B. L. Abrams, W. J. Thomas, J. S. Bang, and P. H. Holloway, *Rev. Adv. Mater. Sci.* 5 (2003) 139-146
- [43] P. H. Holloway, T. A. Trottier, J. Sebastian, S. Jones, X.-M. Zhang, J.-S. Bang, *J. Appl. Phys.* 88 (2000)
- [44] X. Liu, J. Lin, *Solid State Sci.* 11 (2009) 2030-2036
- [45] H-C. Lu, H-K. Chen, T-Y. Tseng, W-L. Kuo, M.S. Alam, B-M. Cheng, *J. Electron. Spectrosc. Related Phenom.* 144-147 (2005) 983-985

INTRODUCTION

A luminescent material or phosphor consists of a host lattice usually intentionally doped with impurities. Phosphors are usually in the form of powders but in some cases, thin films. The impurities that are intentionally doped into the host matrix are referred to as activator ions. In phosphors, the absorption of excitation energy takes place via either on the host lattice or on activator ions. The transfer of energy via the host matrix is also possible. In most cases, the emission in phosphors usually originates from activator ions. The activator ions possess energy levels that can be populated by direct excitation or indirectly by energy transfer. Furthermore, the host matrix should be transparent enough to enable the transfer of visible light to the surface of the phosphor. A large number of phosphor materials based on rare earth ions have dramatically improved the performance of the devices in which they are applied. The basic information on trivalent rare earth ions will be provided in the next section.

2.1 Trivalent rare earth ions

In most cases, the emission from the rare earth ions is due to optical transitions within the $4f^n$ configuration (e.g. Tb^{3+} ($4f^8$), and Eu^{3+} ($4f^7$)). The $4f$ orbital lies inside the ion and therefore it is well shielded from the surroundings by the filled $5s^2$ and $5p^6$ orbitals so that the $4f$ electrons are less influenced by the environment of the lanthanide ion [1-3]. As a result, the $f-f$ emission spectra consist of sharp and narrow lines. Broad emission bands have also been observed for a number of rare earth ions (e.g. Ce^{3+}). In this case, emission corresponds to $5d-4f$ optical transitions. There are four trivalent rare earth ions that were used in this study. These are Praseodymium

(Pr³⁺), Terbium (Tb³⁺), Europium (Eu³⁺), and Cerium (Ce³⁺). Pr³⁺ is a trivalent rare earth ion which has a complex energy level diagram consisting of several metastable multiplets (i.e. ³P_{0,1,2}, ¹D₂, and ¹G₄) which provide the possibility of simultaneous emissions in the blue, green, orange, red, and IR regions depending on the host matrix [4]. In the case of Eu³⁺, the main emission lines occur between the ⁵D₀ level to the ⁷F_J multiplets while in Tb³⁺, the main emission lines occur between the ⁵D₄ to ⁷F_J multiplets. Blue emission from this ion is also known to occur from the ⁵D₃ level to ⁷F_J multiplets. Ce³⁺ on the other hand is a broad band emitter whose 4f configuration consists of only two multiplets: the ground state ²F_{5/2} and the excited state ²F_{7/2}, which are about 2000 cm⁻¹ apart [2].

2.2 Semiconductor nanocrystals ‘quantum dots’

When electrons are confined to a small domain such as a nanoparticle whose diameter is ≤ 10 nm, the system is then called a “quantum dot”. It is believed that when the nanocrystals particle size is reduced, the energy level develops discrete orbits from the continuum, and the energy bandgap increases showing a quantum confinement effect. Quantum confinement effect may be defined as the enlargement of the semiconductor bandgap due to smaller particle size [5,6]. This phenomenon is normally caused by localization of electrons and holes in a confined environment resulting in observable quantization of the energy levels of the electrons and holes. Such aspect of bandgap engineering has led to intense activities to investigate nanocrystals with a wide variety of experimental probes [5,7]. Semiconductor nanocrystals with large absorption cross-section and broad excitation spectrum could act as sensitizers to promote active rare earth ions emission by harvesting the excitation photon energy and then transferring it to the rare earth ions [7].

2.3 Application of phosphors

Phosphor materials can be found in a broad range of everyday applications such as cathode ray tubes (CRTs). CRT technology has dominated displays ever since its creation. However, competitors have entered the market as the need for lighter, less bulky, portable displays has increased. This therefore has strongly promoted the development of new flat panel displays (FDPs). Non-emissive liquid crystal displays (LCDs) which are one of more common displays used mainly for laptop computers [8] came into full-scale production in the 1970s. This display technology is composed of organic molecules (liquid crystals) which exhibit crystal like properties but are liquid at operating temperatures [9,10]. Inorganic and organic light emitting diodes (LEDs), plasma display panels (PDPs), e-beam pumped laser projectors, electroluminescence displays (ELDs), vacuum-fluorescence displays (VFDs), and field emission displays (FEDs) are classified under emissive FDPs technology. LEDs are organic devices whose light is generated through electron-hole recombination upon the application of a voltage and are typically III-V type semiconductor devices [10]. PDPs are associated with fluorescence lamps since a vacuum ultraviolet (VUV) excites the phosphors [8,9]. VFDs and FEDs on the other hand are regarded as CRTs derivatives, except that VFDs function at very low voltages (20-100 V) and produce a broadly diffused electron-beam which then bombards the layered phosphor segments selectively. While EL involves the application of a strong electric field across a thin film phosphor which then generates hot electrons that impact-excite the luminescent centre [9].

2.3.1 Field emission display (FEDs) technology

The FED technology is very promising and much research has been conducted to bring them to the market place to compete with/replace CRTs [11,12]. Such interest arose due to its potential to provide displays with high brightness, high contrast ratio, light weight, and low-power consumption. Both FEDs and CRTs require electron bombardment to produce cathodoluminescence. However, these two technologies differ in a sense that FEDs operate at low voltages (300 V to 10 kV) and much higher current densities (100 μ A) while CRT operates at 25-30 kV and low current densities [11,13,14]. Just like in a VFD or CRT, the image in a FED is produced by impinging electrons which are generated by sharp emitters onto a phosphor coated screen [11,12]. Phosphors used in FEDs must not be only efficient at low voltages, but must also be resistant to Coulombic aging and saturation at high current densities.

2.3.2 Plasma display panels (PDPs)

Unlike LCD which is restricted to a small viewing angle and by a slow response, PDP provides a rapid response and a large viewing angle [15]. Hence, is regarded as the most promising candidate for large TV displays. PDP operates similar to fluorescence lamps [9,16] except that it uses neon or xenon gasses instead of mercury and argon used in fluorescent lamps. Neon and xenon gasses generate peak wavelengths at 147 and 173 nm in the vacuum ultraviolet (VUV) spectral region [9,17,18]. The red, green, and blue PDP phosphors absorb this strong energetic VUV radiation from inert gas plasma and re-radiate the energy as visible light to produce colours that appear in screen.

2.3.3 Basic aspects of luminescence

Luminescence emission in a solid material (phosphor) occurs as a result of radiative electronic transition in which an electron jumps from a higher energy state to a lower one with the difference in energy released as photons (light emission). However, for such process to take place, the electron must first be excited into a higher energy state by some energy from an external source. The return to the ground state has two paths: radiative decay and non-radiative decay. When an excited electron decays by emitting photons, which is luminescence emission, the process is then called radiative decay. Non-radiative decay is when an excited electron decays to the ground state by emitting phonons. In such a case, the absorbed energy is dissipated as heat in the system, as a result no emission is observed. These two processes compete with each other. However, an efficient phosphor suppresses the non-radiative decay and converts most of the absorbed excitation energy into photons [4]. These processes are indicated in figure 2.1 which shows the interaction processes among photon, electron, and phonons in rare earth activated phosphors.

Generally, in most rare earth based phosphors, the luminescence processes begins with absorption of energy on $4f-4f$ transition by electrons. In most phosphor materials, the emission occurs at lower energy than the absorbed energy due to losses that occur during the relaxation process. The difference between the maximum of the lowest excitation band and that of the emission band is called Stokes shift.

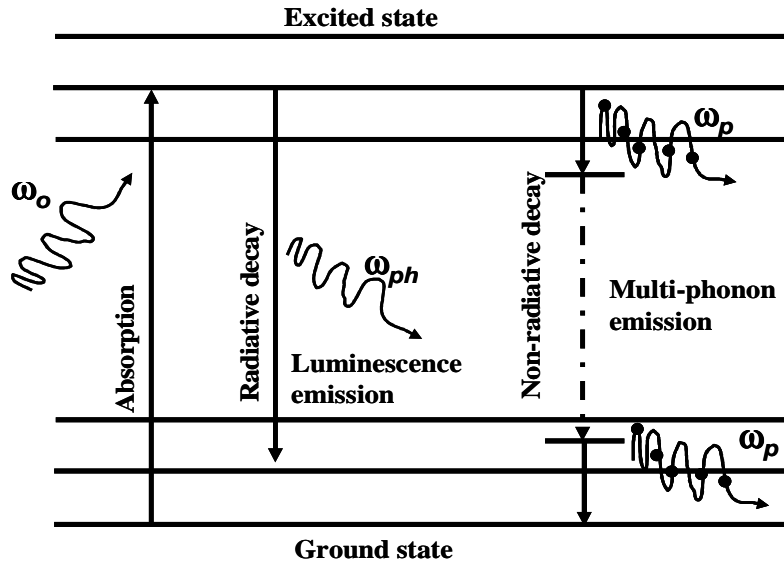


Fig. 2.1: Interactions among photon, electron, and phonon: photon absorption and emission, electron excitation and decay, and phonon emission.

Luminescent phenomena exists in two different forms namely, fluorescence and phosphorescence. Fluorescence is the luminescence process whereby the emission stops immediately after the excitation source has ceased while during phosphorescence process the light emission continues for several seconds, minutes or even hours after the excitation source has ceased. Also, fluorescence has many categories. This categorization was invented to differentiate between the various luminescent excitation methods. For example, if energy is produced by a short-wavelength light i.e. UV or visible light the phenomenon is known as photoluminescence (PL). Cathodoluminescence (CL) occurs when a beam of electrons is used as means of excitation. Electroluminescence (EL) is produced when direct generation of light is caused by application of an electric field to a material. Other luminescence processes include Thermoluminescence where light emission is caused by thermal excitation. Ionoluminescence, is used to describe luminescence

produced from excitation with positive or negative ions. Triboluminescence is when light emission is generated from friction and physical impact. In this study our focus will be on the PL for PDPs and CL for FEDs, these processes will therefore be discussed in detail.

2.3.4 Cathodoluminescence (CL)

In general, CL can be defined as emission in a form of visible light following a series of processes beginning with the interaction between primary electron beam and a luminescent material (phosphor). CL emission is the last of several processes which follow the initial penetration of primary electron beam into a phosphor. This emission is produced when there's enough energy produced by the primary beam to excite the secondary electrons to their ground state via suitable radiative transitions from a specific luminescent centre in the host matrix of the phosphor. Moreover, not all the primary beam energy is converted into light as most of CL materials are never 100 % efficient.

2.3.5 CL generation

When a phosphor material is exposed to energetic electrons, a huge number of free carriers (free electrons and free holes) are produced along the path of the incident electron. The generation of electron-hole pairs in semiconductors under irradiation by energetic electrons occurs through impact ionization. The electron-hole pair generation rate G (s^{-1}) for semiconductors is given by [19]

$$G = EI_b(1 - \eta) / qE_i \quad (2.1)$$

Here E is the energy of the primary electron beam, I_b is the electron-beam current E_i is the average energy required to create an electron hole pair [$E_i = 2.8E_g + E$, where

0.5 eV $<E'< 1.0$ eV reflects phonon participation [19], q is the electronic charge and η is the back-scattered electron coefficient that is dependent on the material and beam voltage.

2.3.6 Electron beam-phosphor interaction

When the primary beam bombard a phosphor material, part of the electron beam penetrates through the phosphor while the other part of the beam is ejected back through the surface due to elastic scattering events with the positively charged nuclei of the surface ions. The ejected electrons are called primary backscattered electrons. These electrons and particularly their energy are lost to the CL process. The remaining electrons penetrate into the phosphor and undergo a series of elastic and inelastic collisions and scattering event which results in their energy loss. These scattering processes lead to a cascade-like process which generates secondary electrons, which, in turn, produces more secondary electrons [20]. Hundreds of free electrons and free holes are also produced along with the production of backscattered and secondary electrons. All these processes provide different information on the material [21]. Figure 2.2 depicts the typical energy spectrum in front of the surface indicating secondary electrons (i.e. at 50 eV and below) Auger electrons, scattered primary electrons (i.e. energy loss electrons) and primary backscattered electrons [22].

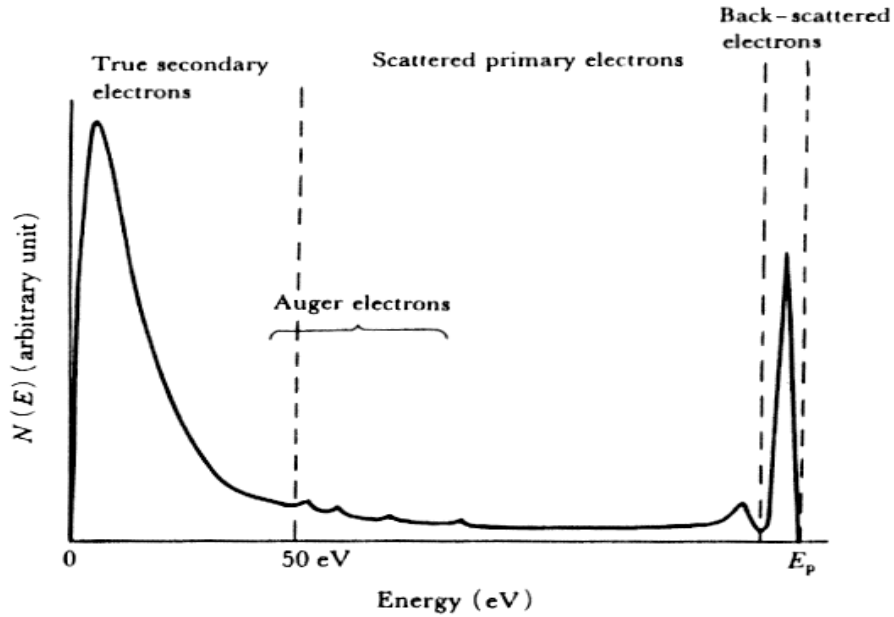


Fig. 2.2 Schematic representation of emission process in CL [22].

In most cases, the electron beam penetration depth into a phosphor material varies with the primary electron beam energy. Ehrenberg and Franks in 1983 observed the path of the primary beam energy [20]. The emission profile is shown in figure 2.3. From this profile, it can be seen that a narrow entrance channel of primary electron changes to an almost spherical region as the beam energy increases [20]. The interaction volume is closer to the surface at lower beam energies due to a higher scattering cross section and less energy to lose [10,20,23].

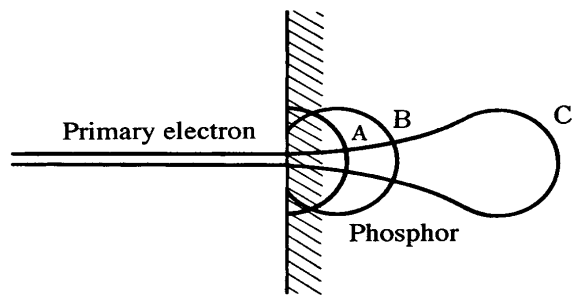


Fig. 2.3 Electron beam penetrating a phosphor material as a function of increasing beam voltages (i.e. $A < B < C$) [20].

Electron penetration and energy dissipation in solids or phosphor materials has been an interesting subject of research [10,20,23-28]. Beam current and voltage are the main parameters that affect the CL response of a phosphor. It is a known fact that the penetration of beam electrons into a phosphor surface or a particular specimen is determined by the electron beam energy. The higher the electron energy, the greater is the penetration depth. Most researchers have observed the increase in phosphor CL intensity with increasing accelerating voltage and beam current [24,26,28]. This has been often attributed to deeper penetration of electron beam into the phosphor surface and the larger electron beam current density. The electron penetration depth can be estimated using the following empirical formula:

$$L(\text{\AA}) = 250(A/\rho)(E/Z^{1/2})^n, \quad n = 1.2/(1 - 0.9 \log_{10} Z) \quad (2.2)$$

E is the anode voltage (keV) [27].

2.3.7 CL intensity degradation in phosphor materials

CL intensity degradation of phosphors can be defined as quenching of luminescence efficiency during a prolonged electron-beam bombardment. The luminescence quenching mechanism has been studied by many researchers in many ways [14,29]. There are four different kinds of effects that are known to contribute to the reduction of the CL efficiency of phosphors. These are: “killer” or “quencher” centres, brightness saturation, concentration and thermal quenching. These will be explained in detail in the next section. The CL intensity of phosphors has been reported to significantly degrade under prolonged electron beam exposure [29-33].

2.3.8 Killer centres

Killers are defects caused by incidental impurities (contamination) and inherent lattice defects that reduce the luminescence intensity of a phosphor [10]. The atoms and molecules adsorbed at the surface of a phosphor may reduce luminescence by producing a non-luminescent layer when they react with ambient vacuum species. The Killer centres exist in two types, namely, the bypassing and the resonance energy transfer type. The bypassing type is known to compete with activator ions in capturing free carriers by so allowing them to recombine non-radiatively. This type can only take place when free electrons and free holes are produced in the conduction band and valance band, respectively. The resonance energy transfer takes away the energy from the activator ion through resonance energy transfer. It occurs at any time and doesn't require the presence of free carriers to reduce the luminescence [20].

2.3.9 Concentration quenching

If the concentration of an activator is too high that it exceeds its optimum concentration, the emission of the phosphor is reduced [34-38]. This phenomenon is called concentration quenching. The quenching starts to occur at a certain concentration, for which there is a sufficient reduction in the average distance between these centres to favour energy transfer [35]. Concentration quenching is ascribed to pairing or aggregation of the activator ions allowing some of them to act as killer centres thus creating a non-radiative pathway. Some researchers have ascribed concentration quenching effect to energy transfer from one ion to another and finally to an energy sink [34,37]. This strongly suggests that concentration quenching related to interaction allows the absorbed excitation energy to reach

particular quenching centres such that the critical concentration depends on the probability of the transfer.

2.3.10 Brightness saturation

Generally, saturation of luminescence occurs when an excitation level is too high. In CL, this process is normally observed when a brightness maximum is reached, even as the current density is increased. There are three possible reasons that have been proposed as the main cause of this process: Firstly, ground state depletion whereby most or all of the luminescent centres are already in the excited state leading to a lack of ground state centre able to accept energy from free carriers [20]. The second reason involves the Auger effect. In this case, the process involves the elastic collision between a free electron and an excited electron at luminescent centre. During such process, the electron is expelled into the conduction band causing a de-excitation of the luminescent centre [22]. The third possible reason is the thermal quenching. This process will be explained in the next section.

2.3.11 Thermal quenching

Thermal quenching is defined as a decrease of luminescence intensity with increasing temperature [10,23,39]. This is usually due to the local heating by energetic electrons or photons. This process is known to occur at high temperatures when thermal vibrations of atoms surrounding luminescent center transfer energy away from the center leading to a non-radiative recombination, and a subsequent dissipation of the excess energy as phonons in the host lattice [32].

The configurational coordinate model of a luminescent centre presented in figure 2.4 can be used to describe the thermal quenching process [40]. In this model, the energies of luminescent centres both in the ground state and excited state are

represented by U_g and U_e , respectively. When the system is thermally excited, it undergoes a vertical transition from ground state to the excited state. This vertical transition causes the system to immediately adapt to the new equilibrium situation by changing the atomic configuration from B to the new equilibrium A along the curve U_e , with energy dissipated as phonons. In a short space of time the system may then undergo a radiative transition from A to D followed by the slower rearrangement of the atomic configuration from D to O along U_g with excess energy dissipated as heat. High temperatures cause the luminescent center to be thermally activated from point A to C along U_e and then thermally released from C to O on the ground state.

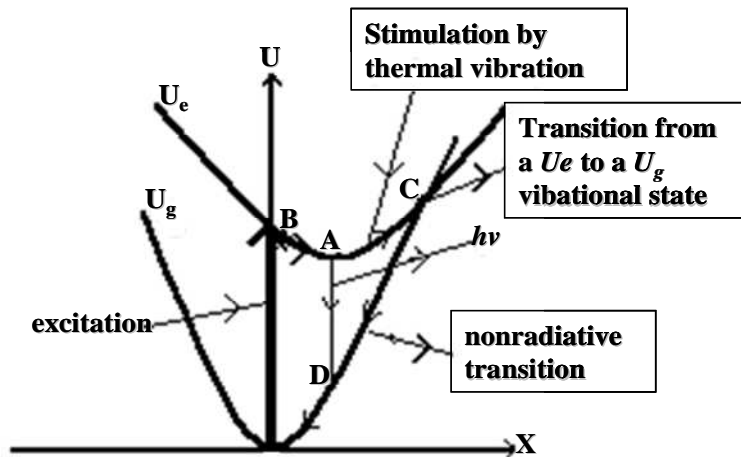


Fig. 2.4 Configurational coordinate model of a luminescent centre in a host matrix [40].

2.3.12 Electron Stimulated Surface Chemical Reaction

Extensive research performed on the CL degradation of phosphors resulted in the proposal of Pfanhls law which describes the rate of degradation of CL intensity and development of an electron stimulated surface chemical reaction (ESSCR) model [14,32,33,41]. The Pfanhl law is given by:

$$I(N) = \frac{I_0}{(1 + CN)}, \quad (2.3)$$

where I is the aged CL intensity, I_0 is the initial CL intensity, N is the number of electrons per unit area and C is the burn parameter which is equal to the inverse of the number of electrons per unit area required to reduce the intensity to half its original value. This model predicts that the CL degradation is depended upon the type of gas in the vacuum, gas pressure, beam voltage and electron (coulombic) dose [14,32].

According to the ESSCR mechanism for the CL intensity degradation of ZnS based phosphors, the reactive gas molecules adsorb on the surface of the ZnS. These molecules are then dissociated by the electron beam from molecular species to reactive atomic species resulting in the formation of a ZnO surface layer and a volatile SO_2 with the consequent loss of CL intensity [31]. The formation of the non-luminescent ZnO surface layer decreases the energy loss in ZnS and subsequently the CL intensity. It was concluded that the non-luminescent traps compete with the CL process and cause a reduction in CL brightness. A mathematical model of an electron stimulated surface chemical reaction (ESSCR) model was invented by Holloway et al [42]. This model shows the relationship between the CL intensity degradation and the depletion of sulphur from the surface of ZnS:Cu,Al,Au and ZnS:Ag,Cl phosphor powders.

2.4 Photoluminescence (PL)

PL in solid phosphor materials (i.e in semiconductor, organic and inorganic insulators) is a process in which luminescence is stimulated by interaction of photons with a material. This process is classified in terms of the nature of the electronic

transitions producing it. PL is classified into two types, namely, intrinsic and extrinsic luminescence.

2.4.1 Intrinsic luminescence

There are three kinds of intrinsic luminescence: (i) band-to-band luminescence, (ii) exciton luminescence, and (iii) cross-luminescence. Band-to-band luminescence refers to luminescence owing to the band-to-band transitions whereby an electron in the valence band recombines with the hole in the conduction band. This process can be observed at relatively high temperatures in very pure crystals. At low temperature it is transformed to exciton luminescence. An exciton can be defined as a composite particle of an excited electron and a hole interaction with one another. Owing to the recombination of the electron with the hole, it moves in a crystal passing on energy and produces luminescence. Cross-luminescence on the other hand is produced when an electron recombines with a hole in the outer most core band. This kind of luminescence only occurs when the energy difference between the top valence band and that of the outer most core band is smaller than the bandgap energy, otherwise an Auger process takes over.

2.4.2 Extrinsic luminescence

Extrinsic luminescence is the process in which luminescence is produced by intentionally doped impurities or defects in the host lattice. These impurities are known as “activators” in phosphor host materials systems. Emission features of the phosphor are characteristic of the particular activator that is present or incorporated in a host matrix. For example, $\text{Y}_2\text{O}_3:\text{Eu}^{3+}$ is the well known red emitting phosphor which is used in colour television screens. The red emission from this phosphor is primarily characteristic of the impurity ion (Eu^{3+}) itself, not the host lattice. Radiative

transitions that are observed from this ion occur between the excited and ground state of the Eu^{3+} and the impurity levels exists within the bandgap of the host lattice.

When a phosphor is excited with UV or VUV radiation, a series of processes can take place leading to emission of either phonons or photons. These processes are described in section 2.3.3. These transitions or relaxations occur between a higher energy state, E^* , and a lower empty energy state, E_0 . The energy or wavelength of the emitted photon can be represented by [43].

$$hv = hc/\lambda = E^* - E_0 \quad (2.4)$$

$$\text{Where } \lambda = \frac{1.2398}{E} \quad (2.5)$$

There are two types of extrinsic luminescence: un-localized and localized type. In the un-localized type, the electrons and holes are involved in the luminescence process. While in the localized type, the luminescence excitation and emission processes are restricted in a localized activator ion or luminescence centre. Various kinds of metallic impurities intentionally incorporated in ionic crystals or semiconductors usually generate localized luminescent centres. Figure 2.5 shows energy level diagram of luminescence transitions within Eu^{3+} ion. Based on this energy level diagram, the absorbed excitation energy promotes transitions to higher excited levels resulting in non-radiative transitions to the $^5\text{D}_{0,1,2,3}$ states. This is followed by radiative transitions to the $^7\text{F}_{0,1,2,3}$ state.

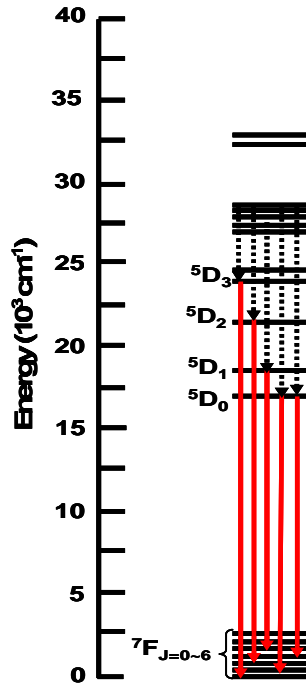


Fig. 2.5 Intra-atomic luminescence transitions within Eu^{3+} ion.

2.5 Energy transfer process in rare earth phosphors

The improved luminescence efficiency from the phosphor can be achieved via energy transfer between the sensitizer (donor) and the acceptor. The study of energy transfer between a pair of identical or non identical rare earth ions has been done by several researchers [44-46]. This includes energy transfer between (i) broad-band and a narrow-line emitters and visa versa, (ii) as well as non identical narrow-line emitters [4]. On the other hand the semiconductor nanocrystals, "quantum dots", have also attracted a lot of attention as they are considered as another good choice as sensitizing centres for radiative relaxation of activator ions since their excitation cross sections are very high due to the efficient band-to-band absorptions. In such a case the enhanced luminescence of rare earth ions is achieved by efficient energy transfer from semiconductor quantum dot (sensitizer) to an activator ion i.e. trivalent rare earth ion [47,48]. The efficiency of radiative transfer relies on how efficiently the activator

fluorescence is excited by the sensitizer emission. However, this requires a significant spectral overlap of the emission line of the sensitizer (donor) and the absorption line of the emitter (acceptor) for energy transfer to take place. In the case of lack of spectral overlap, energy transfer can take place via resonance condition (equal energy difference between the energy levels of the sensitizer and the donor) and/or phonon mediated processes.

2.5.1 Theory of energy transfer

The theory of energy transfer resonance derived by Dexter has revealed that two luminescence centres, a Donor and an Acceptor (A and D) within a certain distance, R with a certain interaction (i.e. exchange or multipole-multipole interaction) may be in resonance and transfer excitation energy from one (donor) to another (acceptor). For near neighbours the energy transfer is possible through the exchange interaction while for interactions over separation of 20 \AA between the donor and acceptor, usually the multipolar interaction takes over. The distance R between the two must be shorter than the critical distance R_c which is approximately twice the radius of a sphere. R_c can be practically calculated using the relation given by:

$$R_c \approx 2 \left(\frac{3V}{4\pi X_c N} \right)^{1/3} \quad (2.6)$$

where X_c represent the critical concentration at which the quenching occurs, V is the volume of the sphere, N is the Z ions in the unit cell [37,38].

When an energy donor D and an acceptor A are close enough that their electronic wavefunctions overlap each other as shown in figure 2.6, the excitation energy of the sensitizer D can be transferred to an acceptor A via exchange

interaction. The rate of energy transfer between a donor and an acceptor due to this interaction as derived by Dexter is as follows:

$$P_{DA}(ex) = 2\pi \left| \langle a'b | H_{DA} | ab' \rangle \right|^2 \int f_D(E) f_A(E) dE \quad (2.7)$$

where D and A are the donor and acceptor, respectively. The integral denotes the spectral overlap between the donor emission and the acceptor absorption, the factors, $f_D(E)$ and $f_A(E)$ represent the normalized shape of the donor emission and acceptor absorption spectra, respectively while the matrix elements can be expressed as a function of the donor and acceptor, so that the energy transfer probability depends upon the distance between the donor and acceptor.

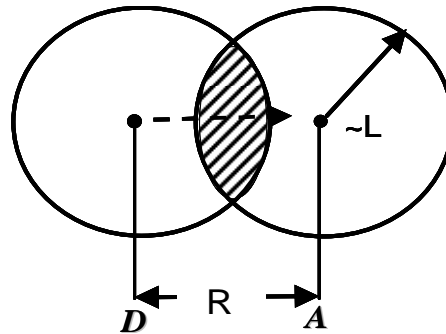


Fig. 2.6 Resonant energy transfer by the quantum mechanical exchange interaction in which the overlapping of the wavefunctions of D and A (shaded area) is considered.

Inokati and Hirayama [49] then used the exchange interaction to develop a quantitative theory of energy transfer and predicted time dependence of fluorescence decay in such coupling. According to their approach, the S ion is surrounded by a set of A ions at distance R_K . During energy transfer, the environment of excited A changes with time resulting in a non-exponential decay which for exchange interaction is described by:

$$I = I_0 \exp \left[\frac{-t}{\tau_A} - \gamma^{-3} \frac{C}{C_0} g \left(\frac{e^{\gamma t}}{\tau_A} \right) \right] \quad (2.8)$$

where τ_A the decay time of the pure donor, C is the acceptor concentration and is defined by:

$$C = 3N / (4\pi R V^3) \quad (2.9)$$

and C_0 represent the critical transfer concentration of an acceptor which is defined by $C_0 = (3/4\pi R_0^3)$, here R_0 and γ are constants related to Dexter quantities by

$$\gamma = 2 R_0 / L \quad (2.10)$$

R_0 representing the critical distance at which the probabilities for radiative and non-radiative transfers are equal. Equation 2.8 predicts an initial decay which is mainly due to donors with nearest acceptors, while the slower portion of fluorescence decay is dominated by the contributions of the more distant acceptors [49].

It is known that non-radiative energy transfer from one ion to another takes place via exchange or multipole-multipole interaction. However, for multipole interactions, it is assumed that the interaction is of the electric dipole-dipole (dd), electric dipole-quadrupole (dq) or electric quadrupole-quadrupole (qq) type. Figure 2.7 shows the two centres which are in close proximity separated by distance R with the electrostatic interaction. The energy transfer rate as derived by Dexter for dd type is given by:

$$P_{DA}(dd) = \frac{3c^4 \hbar^4 \sigma_A}{4\pi^4 \tau_D R^6} \int \frac{f_D(E) F_A(E)}{E^4} dE \quad (2.11)$$

while for dq mechanism is:

$$P_{DA}(dq) = \frac{135\pi\alpha c^8 \hbar^9}{4n^6 \tau_D R^8} \int \frac{f_D(A)F_A(E)}{E^8} dE \quad \alpha = 1.266 \quad (2.12)$$

where R represent the separation between D and A , n denote the refractive index of the crystal, σ_A is the absorption cross-section of A , and τ_D represent the radiative lifetime of D .

When the acceptor ions are distributed randomly with various distances from a donor in a host matrix, the emission decay curve of the donor D becomes non-exponential. The non-exponential decay give the possibility to determine the nature of ion-ion interaction i.e. dd , dq or qq type. Considering the number of activator ions randomly distributed in a sphere around a sensitizer such that the activator concentration is constant when the volume of the sphere and the number of activator ions considered goes into infinity, Inokuti and Hirayama [49] derived a model for dd , dq and qq coupling. In this model the experimental decay curve is described by:

$$I = \exp \left[-\frac{t}{\tau_A} - \Gamma \left(1 - \frac{3}{s} \right) \frac{C}{C_0} \left(\frac{t}{\tau_A} \right)^{\frac{3}{s}} \right] \quad (s = 6, 8, 10) \quad (2.13)$$

Here Γ is the gamma function while equals to 6, 8, 10 for dd , dq , and qq , respectively.

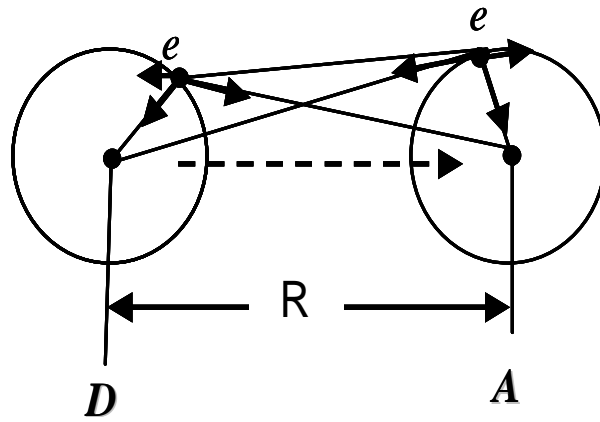


Fig. 2.7 Coulomb interaction in a resonant energy transfer process.

2.5.2 Phonon-assisted energy transfer

Phonon assisted energy transfer is a process in which the mismatch of energy between the donor and acceptor is compensated by simultaneous emission and absorption of one or more phonons [50]. Non-resonant energy transfer can also occur by assistance of phonons not unless the difference between the ground state and the excited state is large. In a case where two rare earth ions are with different excited states, as indicated in figure 2.8, the probability for energy transfer must drop to zero, where the overlap integral $\int f_D(E)f_A(E)dE$ vanishes [51]. It has been experimentally discovered that energy transfer can occur without phonon-broadened electronic overlap provided that the overall energy conservation is maintained by production or annihilation of phonons. However, for smaller energy mismatch, energy transfer assisted by one or two phonons can occur. Then when the energy transfer occurs between the levels of a donor and an acceptor in which the energy mismatches as high as several thousand reciprocal centimetres, then the multiphonon process needs to be taken into considerations. Based on Miyakawa-Dexter's theory, the probability of phonon-assisted transfer (*PAT*) may be expressed by:

$$W_{PAT}(\Delta E) = W_{PAT}(0)e^{-\beta\Delta E} \quad (2.14)$$

ΔE represent the energy gap between the electronic levels of donor and acceptor ions while β is a parameter determined by the strength of electron-lattice coupling as well as by the nature of the phonon involved [52]. The evidence of occurrence of non-resonant energy transfer between various trivalent rare earth ions doped in yttrium oxide was reported by Yamada *et al.* [52]. It was shown that the phonons of about 400

cm^{-1} which produce the highest intensity in the vibronic side bands of yttrium oxide contribute dominantly to the phonon-assisted process.

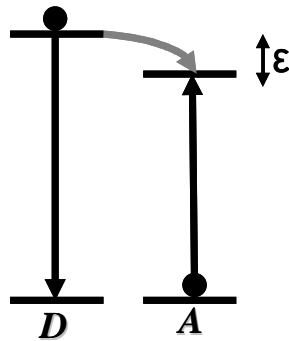


Fig. 2.8 Phonon-assisted non-radiative transfer; ϵ is the energy mismatch.

2.5.3 Cross-relaxation

Cross relaxation is an energy transfer process between identical ions. In a case like that, the same kind of ion is both a sensitizer and an activator. The rare earth ions often show this kind of energy transfer due to their complicated energy level structure. Cross-relaxation may occur between the same rare earth ions, in this case this process becomes a major problem for quenching at higher concentrations. It can also occur between identical rare earth ions which happen to have two pairs of energy levels separated by the same amount. The two bandgap energies may be equal or can be matched by one or two phonons. This process has been observed in many ions and it is a dominating factor in non-radiative relaxations especially at high concentrations.

2.5.4 Migration of excitation energy

Relaxation of excitation energy by migration is a multistep process involving the resonant energy transfer from one ion to another of the same species in a random walk manner and finally to the acceptor which act as a quenching centre. Migration of energy from one donor to another has been found to be more favourable at low acceptor concentration as proposed by Botden *et al.* [44] taking into account for

concentration quenching of fluorescence. When the concentration of two ions is comparable and especially in the rare earth ions where the Stoke's shift is small, the S→S transfer may be even more rapid than the S→A transfer due to the resonant condition. As a result the excitation energy may then migrate among the sensitizer ions before passing to the activator thus decreasing the effective S→A distance. Diffusion of electronic states over donor is one process which increases the transfer efficiency. The migration of energy may also be treated as diffusion or a hopping process as described in detail by Yokota and Tanimoto [53].

2.6 REFERENCES

- [1] R. Reisfeld, *Mater. Sci.*, 20 (2002)
- [2] K. Binnemans, C. Gorller-Walrand, *Chem. Phys. Lett.* 235 (1995) 163-174
- [3] G.H. Dieke, *Spectra and Energy Levels of Rare Earth Ions in Crystals*,
Interscience Publishers: New York (1968)
- [4] G. Blasse, and B.C. Grabmaier, *Luminescent Material*, *Springer: Berlin* (1994)
- [5] A. D. Yoffe, *Adva. Phys.*, 42 [2] (1993) 173-262
- [6] A. P. Alivisatos, *Science*, 271 (1996) 933
- [7] J. Bang, H. Yang, and P. H. Holloway, *J. Chem. Phys.* 123 (2005) 084709
- [8] J-H. Lee, D. N. Liu, S-T. Wu, *Introduction to Flat Panel Displays*, *John Wiley & Sons: Chichester* (2008)
- [9] S. Y. Shionoya, W. M. Yen, *Phosphor Handbook*, *CRC Press LLC: Boca Raton, Florida* (1999)
- [10] L. E. Tannas, W. E. Glenn, and J. W. Doane, *Flat-Panel Display Technologies*,
Noyes Publications: New Jersey (1995)
- [11] L. E. Shea, *Electrochem. Soc. Interface- Summer* (1998)
- [12] A. A Talian, K. A. Dean, J. E. Jaskie, *Solid-State Electron.* 45 (2001) 963-976
- [13] P. Psuja, D. Hreniak, and W. Streck, *J. Nanomater.* (2007) 81350
- [14] B. L. Abrams, W. J. Thomas, J .S. Bang, and P. H. Holloway, *Rev. Adv. Mater. Sci.* 5 (2003) 139-146
- [15] C-H. Kim, II Eok Kwon, C-H. Park, Y-J. Hwang, H-S. Bae, B-Y. Yu, C-H. Pyun, G-Y. Hong, *J. Alloys Compd.* 311 (2000) 33-39
- [16] C. R Ronda, T. Justel, H. Nikol *J. Alloys Compd.* 669 (1998) 275-277
- [17] Z. Zhang, Y. Wang, J. Zhang, *Mater. Lett.* 62 (2008) 846-848

- [18] H-C. Lu, H-K. Chen, T-Y. Tseng, W-L. Kuo, M.S. Alam, B-M. Cheng, *J. Electron Spectrosc. Related Phenom.* 144-147 (2005) 983-985
- [19] D. R. Vij, *Luminescence of Solids*, Plenum Press: New York and London (1998)
- [20] G. F. J. Garlick, *J. Appl. Phys.* 13 (1962)
- [21] B. Dierre, X. Yuan and T. Sekiguchi, *Sci. Techn. Adv. Matter.* 11 (2010) 043001
- [22] B. L. Abrams, PhD thesis, University of Florida (2001)
- [23] W. Ehrenberg, and D. E. N. King, *Proc. Phys. Soc.* 81 (1963) 751-766
- [24] V. Kumar, V. Mishra, S. S. Pitale, I.M. Nagpure, E. Coetsee, O.M. Ntwaeaborwa and H.C. Swart, *J. Appl. Phys.*, 107 [12] (2010) 123533
- [25] R. J. Bieringer, *Phys. Rev.* 142 [2] (1965) 551-554
- [26] W. Chen, H. Liang, X. Ding, Y. Liu, Q. Su, *Appl. Phys. B* 102 (2011) 699–704
- [27] C. Fredman, *Phys. Rev.* 117 (1960) 455-459
- [28] G. Li, Z. Wang, M. Yu, Z. Quan, J. Lin, *J. Solid State Chem.* 179 (2006) 2698-2706
- [29] D. B. M. Klassen, and D. M. De Leeuw, *J. Lumin.* 37 (1987) 21-28
- [30] O.M. Ntwaeaborwa, H.C. Swart, R.E. Kroon, P.H. Holloway, J.R. Botha, *J. Chem. Phys. Sol.* 67 (2006) 1749-1753
- [31] O.M. Ntwaeaborwa, K.T. Hillie, and H.C. Swart, *Phys. Status Solidi C* 1 [9] (2004) 2366-2371
- [32] H.C. Swart, K.T. Hillie and A.P. Greeff, *Surf. Interface Anal.* 32 (2001) 110-113
- [33] S. H. Shin, D. Y. Jeong, and K. S. Suh, *Jpn J. Appl. Phys.* 40 (2001)
- [34] C. de Mello Donega, A. Meijerink, and G. Blasse, *J. Appl. Spectrosc.* 62 [4] (1995)
- [35] J. L. Ferrari, A. M. Pires, M. R. Davolos, *Mater. Chem. Phys.* 113 (2009) 587-590

- [36] Y. Satoh, H. Najafov, S. Ohshio and H. Saitoh, *Adv. Tech. Mater. Mater. Process.* 17, [1] (2005), 43-46
- [37] X. Zhang, X. Qiao, H. J. Seo, *Curr. Appl. Phys.* 11 (2010) 442-446
- [38] Q. Pang, J. Shi, and M. Gong, *J. Am. Ceram. Soc.* 90 (2007) 3943-3946
- [39] G. E. Gosnell, C. J. Wetteland, J. R. Tesmer, M. G. Hollander, D. W. Cooke, I. V. Afanasyev, K. E. Sickafus, *Nucl. Instr. Meth. Phys. Res. B* 241 (2005) 563-567
- [40] K.T Hillie, PhD thesis, University of Free State (2001)
- [41] H.C. Swart, and K.T. Hillie, *Surf. Interface Anal.*, 30 (2001) 383-386
- [42] P. H. Holloway, T. A. Trottier, J. Sebastian, S. Jones, X.-M. Zhang, J.-S. Bang, *J. Appl. Phys.* 88 (2000)
- [43] C. R. Brundle, C. A. Evans and S. Wilson, *Encyclopedia of Materials Characterization, Manning Publications Incorporated: Greenwich, Connecticut.*
- [44] T. F. Soules, R. L. Bateman, R. A. Hewes, and E. R. Kreidler, *Phys. Rev. B* 7 (1973) 1657-1667
- [45] H. B. Tripathi, A. K. Agarwal, H. C. Kandpal, and R. Belwal, *Solid State Commun.* 28 (1978) 807-814
- [46] P. Solarz, W. Ryba-Ramanowski, *Radiat. Meas.* 42 (2007) 759-762
- [47] J. Bang, H. Yang, and P. H Holloway, *J. Chem. Phys.* 123 (2005) 084709
- [48] R. Reisfeld, M. Gaft, T. Saridarov, G. Panczer, M. Zelner, *Mater. Lett.* 45 (2000) 154-156
- [49] M. Inokuti and F. Hirayama, *J. Chem. Phys.* 43 (1965) 1978-1989
- [50] X. L. Ruan, and M. Kaviani, *J. Appl. Phys.* 97 (2005) 104331
- [51] Q.Y Zhang, X.Y Zhang, *Prog. Mater. Sci.* 55 (2010) 353-427)

- [52] R. Reisfeld, Excited States and Energy Transfer from Donor Cations to Rare Earths in the Condensed Phase, *Springer: Berlin* (2006)
- [53] M. Yokota and O. Tanimoto, *J. Phys. Soc. Jpn*, 22 (1967) 779-784

MATERIALS CHARACTERIZATION

3.1 INTRODUCTION

Particle morphology, elemental composition, and structure of the phosphors were studied using scanning electron microscopy (SEM), transmission electron microscopy (TEM), energy dispersive spectrometer (EDS), and X-Ray diffraction (XRD), respectively. The thermal analyses were performed in an N₂ atmosphere using the Thermogravimetric analysis (TGA) technique. The optical properties were studied by Fourier Transform Infrared (FTIR) spectrometer and UV-VIS spectrometer. Luminescent properties were studied using a fluorescence spectroscopy and the data was collected both at room temperature and in a liquid nitrogen temperature. The synchrotron radiation using SUPERLUMI setup at DESY LAB was also used to do PL analysis. The CL data were recorded using an Ocean Optics S2000 spectrometer attached to an ultra high vacuum chamber of the Physical Electronics PHI 549 Auger spectrometer.

3.2 CHARACTERIZATION TECHNIQUES

3.2.1 X-Ray diffraction, XRD

X-ray diffraction (XRD) is a popular and powerful technique for determining crystal structure of materials. During XRD analysis, a collimated X-Ray beam of a specific known wavelength is directed to the sample and the angles at which the beam is diffracted are measured. The crystalline phase of a material can also be identified by examining the diffraction pattern. The widths of the diffraction lines are closely related to the size, size distribution, defects, and strain in nanocrystals. As the size of the nanocrystal decreases, the line width is broadened due to loss of long range order

relative to the bulk. The average crystallite size, D , can be estimated from the broadened peaks by using the Debye-Scherrer equation which is given by:

$$D = \frac{k\lambda}{\beta \cos \theta} \quad (3.1)$$

Where β is the full width at half maximum of a diffraction line located at angle θ while λ is the X-Ray diffraction wavelength. In this study, the XRD measurements were conducted using a PANalytical X'Pert PRO diffractometer. The schematic diagram of the XRD system is shown in figure 3.1.

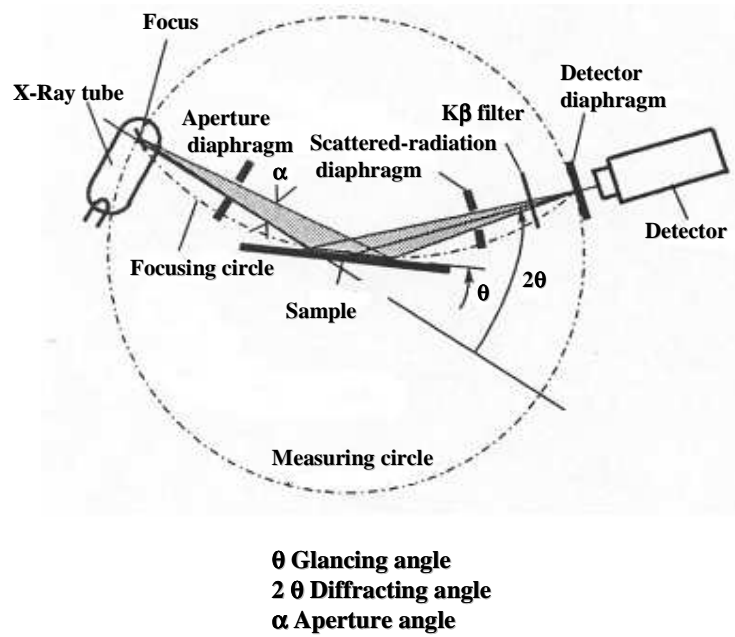


Fig. 3.1 Schematic of the system for XRD measurements [1].

3.2.2 Scanning electron microscopy, SEM

Scanning electron microscopy (SEM) is the most useful tool for imaging the surfaces of almost any material. It uses an electron beam to obtain high levels of magnification and resolution for imaging. The image resolution offered by SEM depends not only on the property of the electron probe, but also on the interaction of the electron probe with the specimen. Interaction of an incident electron beam with the specimen produces secondary electrons or backscattered electrons, with energies typically smaller than 50 eV [2]. Additionally, x-rays are also ejected when an incident electron beam strikes a sample, and these are characteristic of the atoms of the sample. The energies of the x-rays can be characterized by an energy dispersive x-ray spectroscopy (EDS) if the x-ray spectrometer is attached. Field Emission SEM produces high resolution images that can be used to examine defects, surface morphology, stains, grain size, particle distribution, porosity in materials as well as coatings. This technique provides outstanding image resolution, unique image contrast and a large depth of field. In this study, the SEM images of the phosphor powders were obtained from the JEOL-JSM 7500F Field Emission Scanning Electron Microscope (FESEM). Figure 3.2 shows the schematic diagram of the scanning electron microscope.

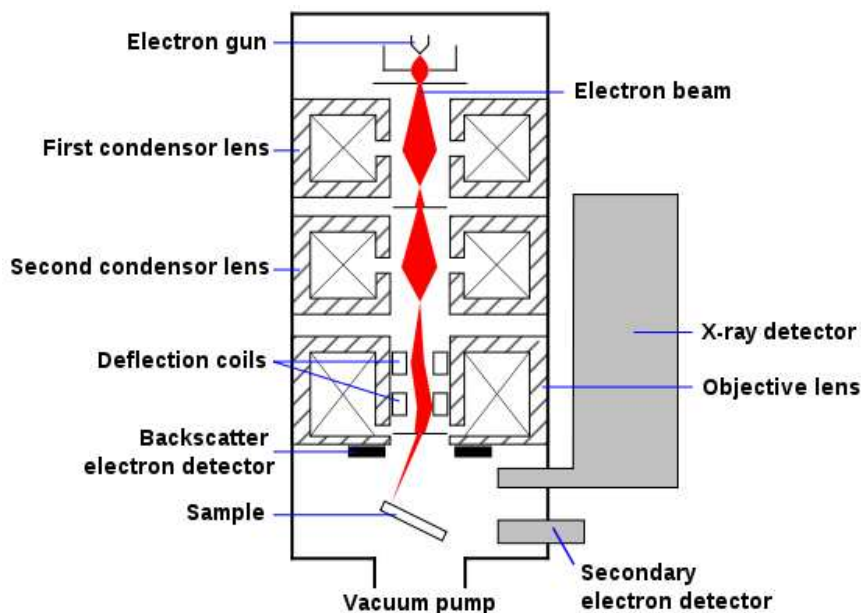


Fig. 3.2 Schematic diagram of SEM [3].

3.2.3 Transmission electron microscopy, TEM

Transmission electron microscopy (TEM) is a high spatial resolution characterization tool. A high spatial resolution TEM has the capability to directly image atoms in crystalline specimens at resolutions close to 0.1 nm, smaller than interatomic distance. An electron beam can also be focused to a diameter smaller than ~ 0.3 nm, allowing quantitative analysis from a single nanocrystal. This type of analysis is extremely important for characterizing materials at a length scale from atoms to hundreds of nanometers. TEM can be used to characterize nanomaterials to obtain information about particle size, shape, crystallinity, and interparticle interaction. If this technique is equipped with EDS, elemental identification through measurements of characteristic X-Ray energies can be done. In the current study, the JEOL-Jem 2100 HRTEM was used to analyze structure and the particle morphology of powder phosphors. In Figure 3.3, the schematic diagram of the TEM is presented.

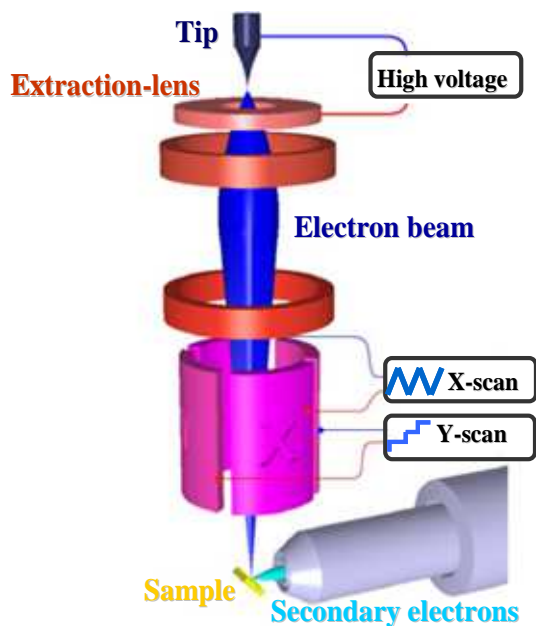


Fig. 3.3 Schematic diagram of HRTEM [4].

3.2.4 Thermogravimetric analysis, TGA

The mostly used thermal analysis includes differential thermal analysis (DTA), differential scanning calorimetry (DSC), and thermogravimetric analysis (TGA). DTA and DSC are used to monitor the heat flow to and from a sample and to or from a reference as a function of temperature or time while the sample is subjected to a controllable temperature program, respectively. The TGA is a very unique technique which is monitored as a function of temperature or time by means of the mass of the sample. TGA was used in this study to determine phase formation, decomposition, thermal stability, and sintering behavior of the phosphor gels. Figure 3.4 shows the schematic representation of the TGA technique which was used in this study.

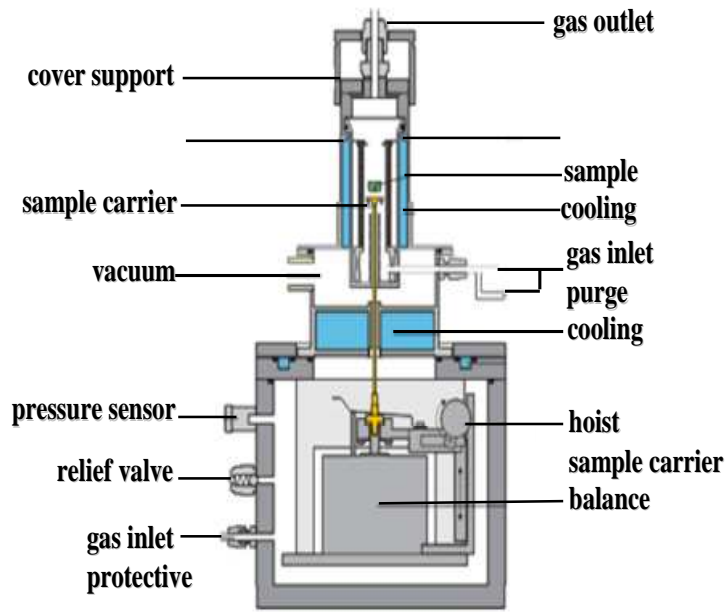


Fig. 3.4 Schematic diagram of TGA [5].

3.2.5 UV-VIS spectroscopy

UV/Vis spectrophotometry is a technique which measures the intensity of light passing through a sample (I), and compares it to the intensity of light before it passes through the sample (I_0). The ratio I/I_0 is called the transmittance, and is usually expressed as a percentage (% T). The absorbance, A , is based on the transmittance:

$$A = -\log(\%T/100\%) \quad (3.2)$$

The UV-Vis spectrometer can also be configured to measure reflectance. UV-Vis spectrophotometer can be either single beam or double beam [6]. In the current study, the Lamda 750S UV-VIS spectrophotometry was used to study the absorption properties of the phosphor samples. Figure 3.5 shows the schematic diagram of a double-beam UV-Vis spectrophotometry.

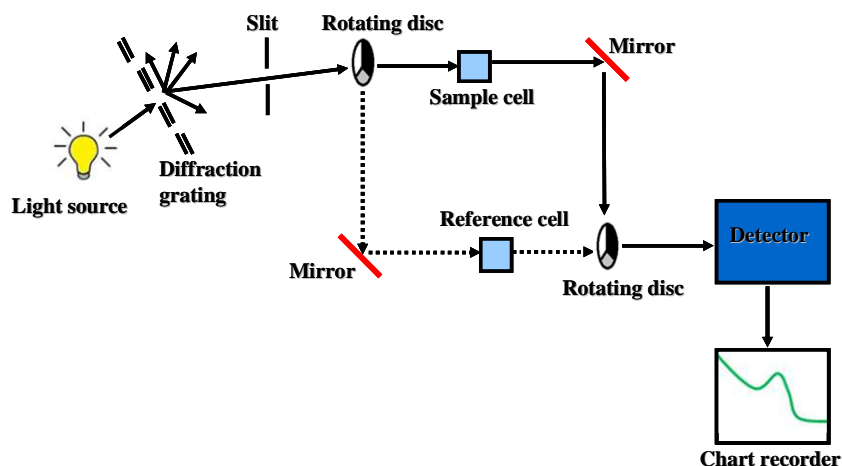


Fig. 3.5 Simplified optical layout of a typical double-beam UV-Vis Spectrophotometry.

3.2.6 Fourier Transform Infrared (FT-IR) spectroscopy

Fourier Transform-Infrared Spectroscopy (FTIR) is an excellent technique which is mainly used to identify organic and in some cases inorganic materials. The spectra of FTIR provide information about the specific molecular structures present. When a material is excited with infrared photons, absorbed IR radiation usually excites molecules into a higher vibrational state. The wavelength of light absorbed by a particular molecule is a function of the energy difference between the at-rest and excited vibrational states. The wavelengths that are absorbed by the sample are characteristic of its molecular structure. Attenuated total reflection (ATR) infrared spectroscopy is a special form of reflectance FTIR where the IR radiation makes several passes through the ATR crystal and with each pass a relatively thin layer of the adjacent sample is analyzed [7]. The FTIR measurements were conducted using a spotlight 400 FTIR imaging system shown in figure 3.6.

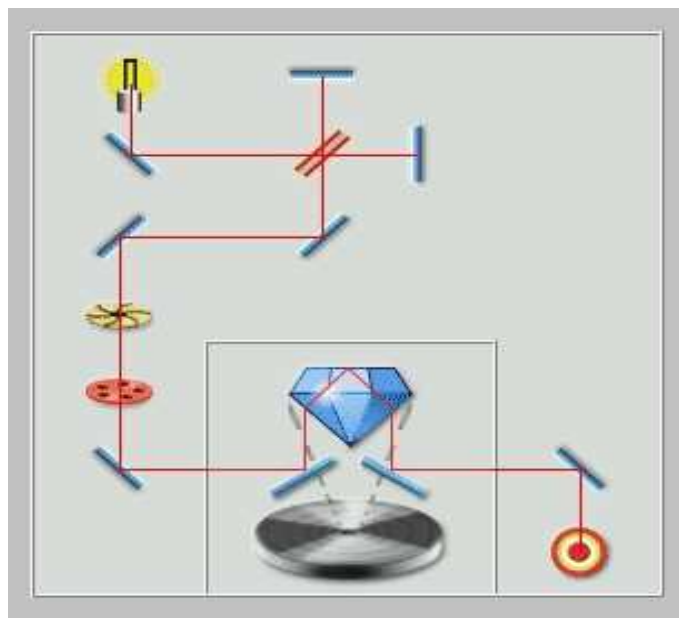


Fig. 3.6 Simplified layout of the FTIR system showing line path to the ATR mode.

3.2.7 Auger Electron Spectroscopy, AES

Auger electron spectroscopy, AES, is a very sensitive technique used to investigate elements, elemental composition and defects. All elements can be detected with this technique except H and He [7]. AES is based on the measurement of the kinetic energies of the emitted Auger electrons. It can also be used for depth profiling in order to analyze elemental chemistry beneath the initial surface region and this is achieved by using the primary beam together with the ion beam.

During the Auger process, the high-energy primary electron hits and releases an electron from the core level thus ionising the atom. In order for this atom to reorganize itself to a lower energy state, an electron from the higher level will drop to the lower level to fill the vacancy caused by the released electron. The excess energy released in this transition is either emitted as a photon or given to another electron in the higher level. If the energy is sufficient, this electron can be ejected from the

surface and detected as an Auger secondary electron. Due to the specific energy levels involved in the transition and the energy of the detected Auger electron, the atom from which the electron was ejected can be identified. The changes in the chemical composition of the surface during degradation are thus easily monitored with the Auger electron spectroscopy. The PHI model 549 Auger spectrometer was used in this study and figure 3.7 shows the schematic representation of this technique.

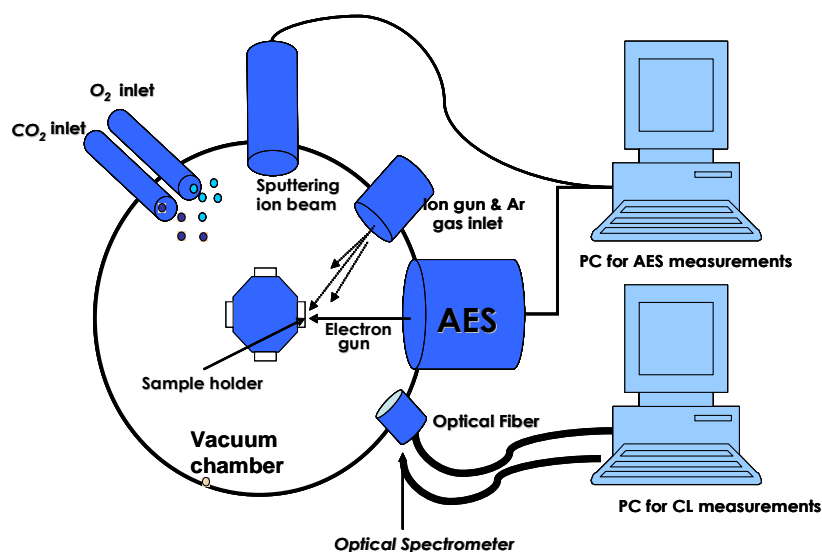


Fig. 3.7 Schematic diagram of Auger spectroscopy.

3.2.8 Photoluminescence, PL analysis

In PL spectroscopy, photoemission is measured following excitation of the sample with a fixed wavelength of light. Photoluminescence reflects the electronic transition from the excited state to the ground state, the valence band. Since PL is a “zero-background” experiment, it is much more sensitive, by approximately 1000 times, than UV-visible absorption measurements [8]. In this work, the PL analyses were conducted using an LS 55 fluorescence spectrometer. The block diagram of fluorescence spectrophotometry is shown in figure 8.

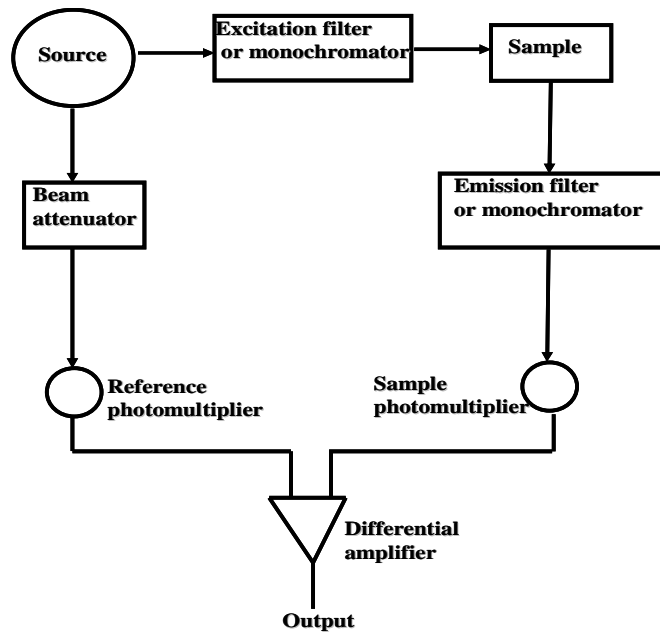


Fig. 3.8 Block diagram of fluorescence spectroscopy.

In addition, a SEPERLUMI setup at the Hamburger Synchrotronstrahlungslabor (HASYLAB), *Deutsches Elektronensynchrotron (DESY)* in Hamburg, Germany was used for PL measurements. The SUPERLUMI is a setup for luminescence spectroscopy with synchrotron radiation (SR) excitation at HASYLAB. The setup is optimized for selective excitation in the vacuum ultraviolet (VUV) spectral range and for luminescence analysis from the VUV to the near infrared (IR) [9]. The setup which was used is shown schematically in Fig.3.9.

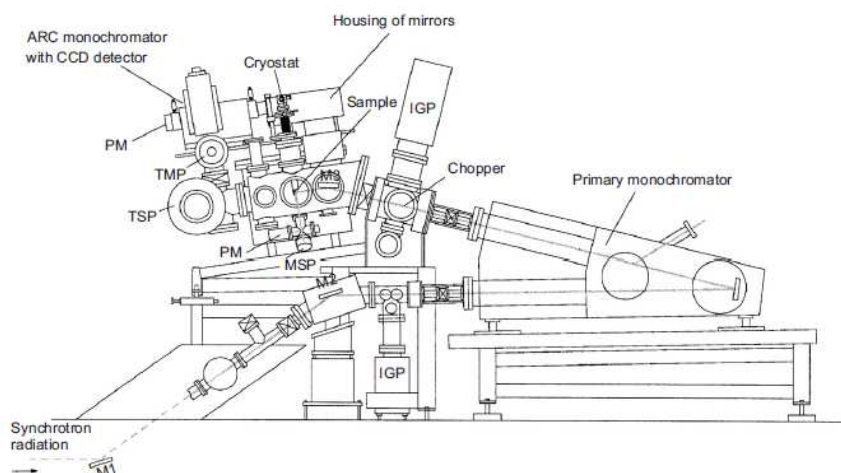


Fig. 3.9 Schematic representation of the Side view of SUPERLUMI setup [5].

The lifetime measurements were conducted using an optical parametric oscillator (OPO Continuum Surelite) pumped by third harmonic Nd:YAG laser source as an excitation source. The decay signals were detected and stored out with a Tektronix TDS 3052 digital oscilloscope. The measurements were carried out at liquid-helium temperatures using a cryostat (CF-1204 Oxford Instruments) on a continuous flow mode.

3.3 REFERENCES

- [1] J. R. Connolly, for EPS400-002, Introduction to X-Ray Powder Diffraction, *Springer* (2007)
- [2] C. P. Poole, F. J. Owens, Introduction to Nanotechnology, *John Wiley & Sons, Inc.* (2003)
- [3] Sri D. Suneel, Industrial Production Engineering: special nano materials, characterization and tools.
- [4] T. L. Kirk, U. Ramsperger, L. G. De Pietro, H. Cabrera, T. Bähler, Near field emission SEM, *ETH Zurich: D-PHYS* (2009)
- [5] NETZSCH, www.netzsch-thermal-analysis.com/en/products
- [6] B. M. Tissue, <http://www.files.chem.vt.edu/chem-ed/spec/spectros.html> (2000)
- [7] Evans Analytical Group, Auger Electron Spectrometry Theory Tutorial: <http://www.cea.com/tutorial.htm> (2001).
- [8] J. Zhang, C. D. Grant, Optical and dynamic properties of undoped and doped semiconductor nanocrystals, *World Scientific Publishers Co, Pty. Ltd.*
- [9] G. Zimmerer, *Radiat. Meas.* 42 (2007) 859-864

CL PROPERTIES OF $\text{SiO}_2:\text{Pr}^{3+}$ AND $\text{ZnO}:\text{SiO}_2:\text{Pr}^{3+}$ **NANOPOWDER PHOSPHORS****4.1 INTRODUCTION**

The devotion that has been dedicated to Pr^{3+} has provided an excellent understanding of the main features of this ion. Depending on the host matrix, Pr^{3+} can emit efficiently in the blue, green, orange, red and near infrared (NIR) regions [1-3]. The Pr^{3+} ion has been studied in numerous hosts including crystals [4-6], and glasses [1-2, 7-16]. Phosphors with high luminous efficiency and thermal stability are regarded as the best candidates for application in FED technology. One of the problems that affect the performance of FEDs and limits their commercialization is degradation of the phosphors at high current density under prolonged electron bombardment. In particular, sulphide based phosphor which are widely used in display technology have been found to degrade drastically under prolonged electron beam bombardment [18]. On the other hand, oxide based phosphors have been reported to be more chemically and thermodynamically stable under high current densities, high vacuum pressures as well as at elevated temperatures [19]. As a result, research interest in the development and investigation of oxide phosphors, as possible candidates to replace sulphide based phosphors in low voltage FEDs, has increased considerably lately.

In this chapter, the CL properties of SiO_2 , $\text{SiO}_2:\text{Pr}^{3+}$ and $\text{ZnO}:\text{SiO}_2:\text{Pr}^{3+}$ phosphor powders and their CL intensity degradation mechanisms are discussed.

These phosphors are evaluated for possible applications in low voltage field emission display.

4.2 EXPERIMENTAL

4.2.1 Sample preparation by sol-gel method

4.2.1.1 ZnO nanocrystals

The preparation of colloidal solutions of ZnO nanoparticles in alcohols has been investigated in the past two decades [19-20]. To obtain a sol of ZnO nanocrystals, 0.459 g $\text{Zn}(\text{CH}_3\text{COO})_2 \cdot 2\text{H}_2\text{O}$ was dissolved in 30 ml of boiling absolute ethanol and stirred for ~ 1 hour to form a transparent solution and cooled in ice water. A 0.2 g of NaOH dissolved in 10 ml of absolute ethanol at room temperature in an ultrasonic bath was cooled in ice water and added dropwise to the ethanol suspension of Zn^{2+} under vigorous stirring. The resulting clear sol was kept at room temperature for 24 hours to allow nucleation and growth of nanoparticles followed by centrifuging and washing repeatedly with heptane to remove unwanted Na^+ and CH_3COO^- ions. The resulting ZnO precipitate was either re-dispersed in ethanol or dried in an oven at 90 °C for 2 hours.

4.2.1.2 $\text{SiO}_2\text{:Pr}^{3+}$ and $\text{ZnO}\cdot\text{SiO}_2\text{:Pr}^{3+}$ phosphor powders

Pr^{3+} doped SiO_2 samples were prepared using a sol-gel process from a starting mixture of tetraethyl orthosilicate ($\text{Si}(\text{OC}_2\text{H}_5)_4$), or TEOS, de-ionized water, ethanol, nitric acid (HNO_3) as a catalyst, and $\text{Pr}(\text{NO})_3 \cdot 6\text{H}_2\text{O}$. The mixture of 0.05 mol of TEOS, 0.1 mol of H_2O , 0.1 mol of ethanol, and 0.145 mol of dilute nitric acid was stirred at room temperature for 1 hour to get a clear solution followed by slow addition of 1 mol% of $\text{Pr}(\text{NO})_3 \cdot 6\text{H}_2\text{O}$ dissolved in 5 ml of ethanol and stirred for 30

minutes. The resulting $\text{SiO}_2\text{Pr}^{3+}$ (1 mol%) sol was divided into two parts. The first part was transferred into a petri dish for drying and the second part was combined with the ethanol suspension of 1 mol% of ZnO nanoparticles with vigorous stirring at room temperature for 1 hour. The gels were dried at room temperature for eight days, ground using a mortar and pestle and then heat treated at 600 °C for 2hrs in ambient air.

4.3 RESULT AND DISCUSSION

4.3.1 Sample structure (XRD)

Figure 4.1 shows the XRD patterns of the ZnO nanoparticles and the standard ZnO micro-particles powders corresponding to the well known wurtzite hexagonal structure of ZnO. The broadening of the ZnO diffraction peaks is attributed to the smaller particle sizes. The average crystallite size of the ZnO nanoparticles estimated from Scherrer's equation was ~ 4 nm. With or without the Pr^{3+} and the ZnO nanoparticles, SiO_2 was amorphous even after annealing at 600 °C for 2 hours (see figure 4.2). This is probably due to the relatively low concentration of Pr^{3+} and the ZnO nanoparticles and/or high amorphous scattering background from the SiO_2 matrix [21]. In addition, this may also indicate that the ZnO and Pr^{3+} ions are well dispersed in the SiO_2 matrix and remained small even after annealing. The presence of the Pr^{3+} and ZnO nanoparticles in the phosphor powders (not shown) was confirmed by EDS.

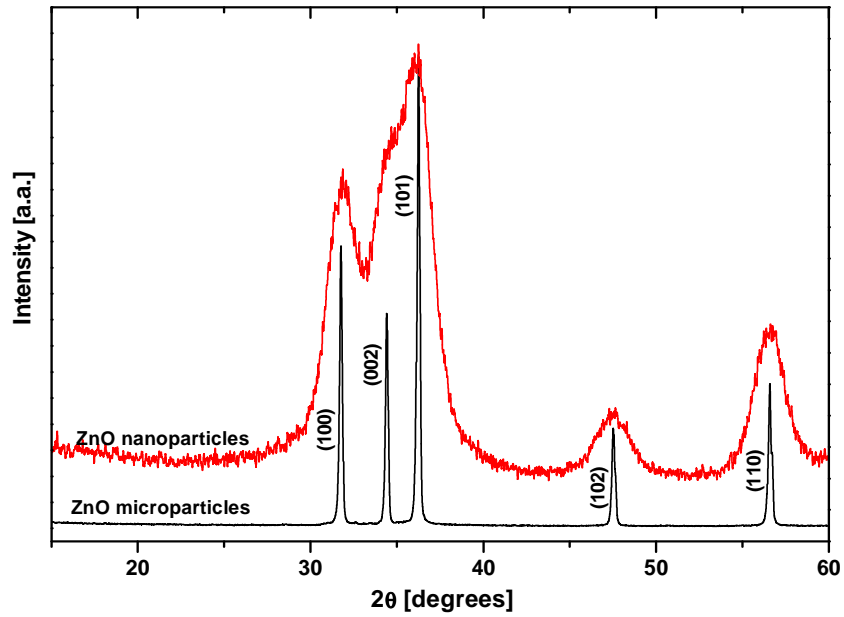


Fig. 4.1 XRD patterns of the ZnO nanoparticles and microparticles.

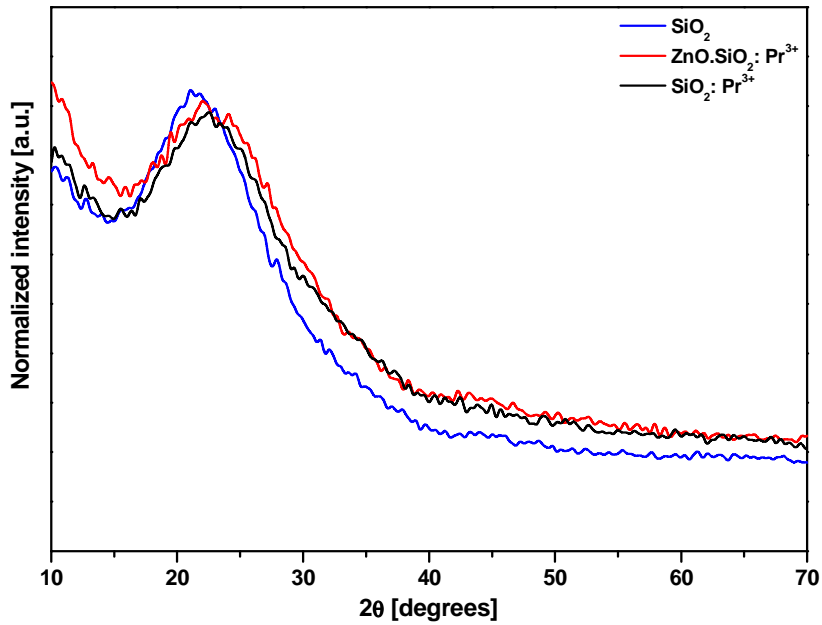


Fig. 4.2 XRD patterns of SiO_2 nanoparticles, $\text{SiO}_2:\text{Pr}^{3+}$ and $\text{ZnO}:\text{SiO}_2:\text{Pr}^{3+}$ nanophosphor powders calcined at 600°C for 2hrs.

4.3.2 Sample morphology (FESEM)

The FESEM images in figures 4.3 (a), (b), and (c) illustrate the particle morphologies of the SiO_2 , $\text{SiO}_2:\text{Pr}^{3+}$ and $\text{ZnO}:\text{SiO}_2:\text{Pr}^{3+}$ nanopowders calcined at 600°C for 2hrs. The images revealed that the particles were agglomerated and mostly spherical in shape with an average particle size in the range of ~ 20 to 30 nm in diameter.

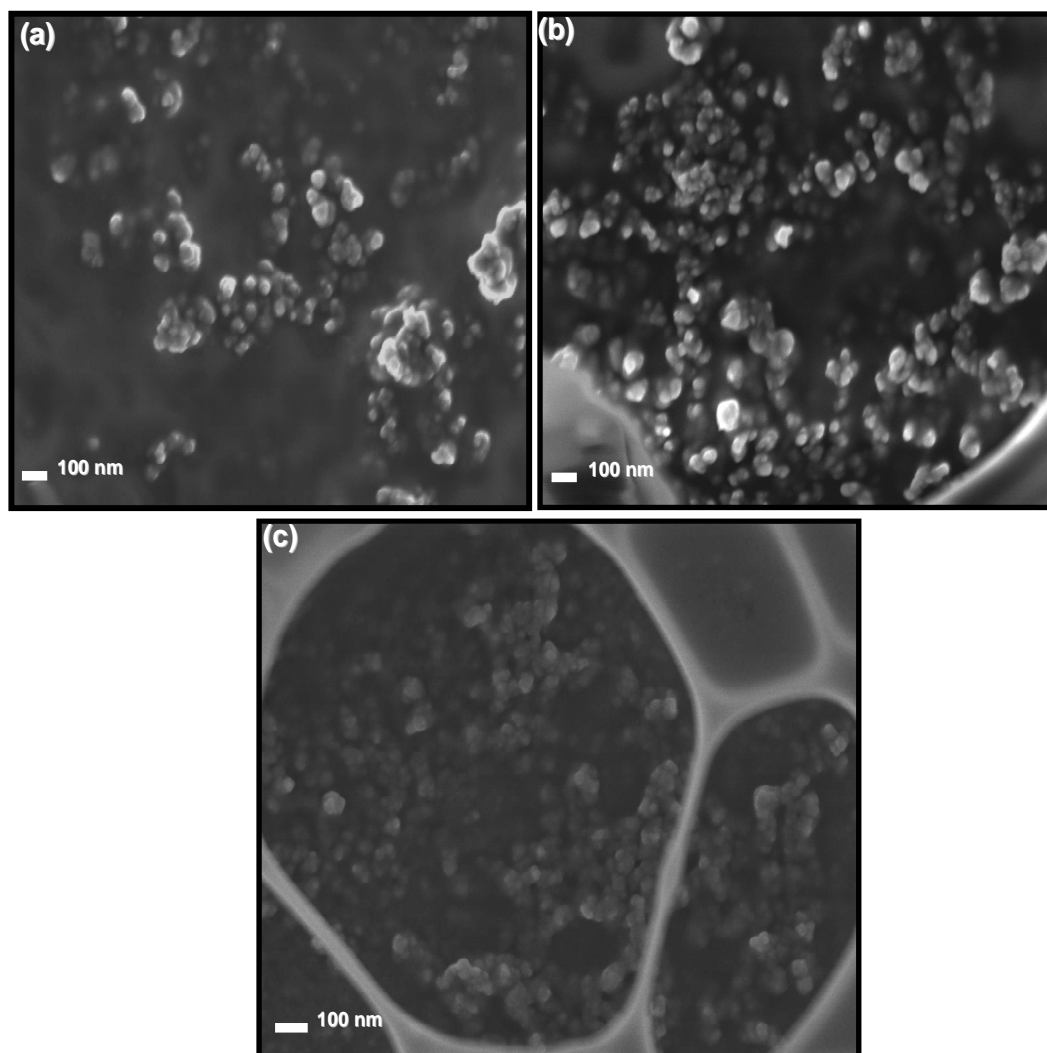


Fig. 4.3 HRSEM images of (a) SiO_2 , (b) Pr^{3+} doped SiO_2 , and $\text{ZnO}:\text{SiO}_2:\text{Pr}^{3+}$ nanopowders.

4.3.3 Thermal Analysis, TGA

The TGA curves of SiO_2 , $\text{SiO}_2:\text{Pr}^{3+}$ and $\text{ZnO}:\text{SiO}_2:\text{Pr}^{3+}$ are presented in figure 4.4. The first weight loss was observed at temperatures between $50\text{ }^\circ\text{C}$ and $130\text{ }^\circ\text{C}$ and it can be ascribed to loss of physically adsorbed water and ethanol [22]. The second weight loss at $250\text{ }^\circ\text{C}$ to $600\text{ }^\circ\text{C}$ corresponds to relaxation of silica network and oxidation of residual organics. The weight loss was shown to decrease as the temperature exceeded $600\text{ }^\circ\text{C}$ until stable phases formed at $\geq 900\text{ }^\circ\text{C}$. The total weight loss for SiO_2 , $\text{SiO}_2:\text{Pr}^{3+}$ and $\text{ZnO}:\text{SiO}_2:\text{Pr}^{3+}$ was $\sim 19\%$, $\sim 25\%$, and $\sim 22\%$, respectively. It can be seen that the rate of weight loss was faster in Pr^{3+} and/or ZnO doped SiO_2 samples. This could be due to enlargement in the pore volume and surface area of gels with introduction of 1 mol% of Pr^{3+} and 1 mol% of ZnO nanoparticles in the SiO_2 matrix.

Biswas *et al.* [22] reported an increase in total weight loss with increasing Pr^{3+} content (i.e. 22 %, 29 %, and 32 % for SiO_2 , $\text{SiO}_2:\text{Pr}^{3+}$ (5 wt %), and $\text{SiO}_2:\text{Pr}^{3+}$ (10 wt %), respectively). Naturally, the gels are microporous and consist of large number of internal silanol groups. When the gel is heat treated, the pores collapse gradually as temperature increases and convert to pore-free materials similar to silica gels [5]. As a result, the hydrogen-bonded silanol groups release water to produce Si-O-Si bonds, and then the steam gives rise to foaming of densified gels which occurs at elevated temperatures as reported by Biswas *et al.* [22].

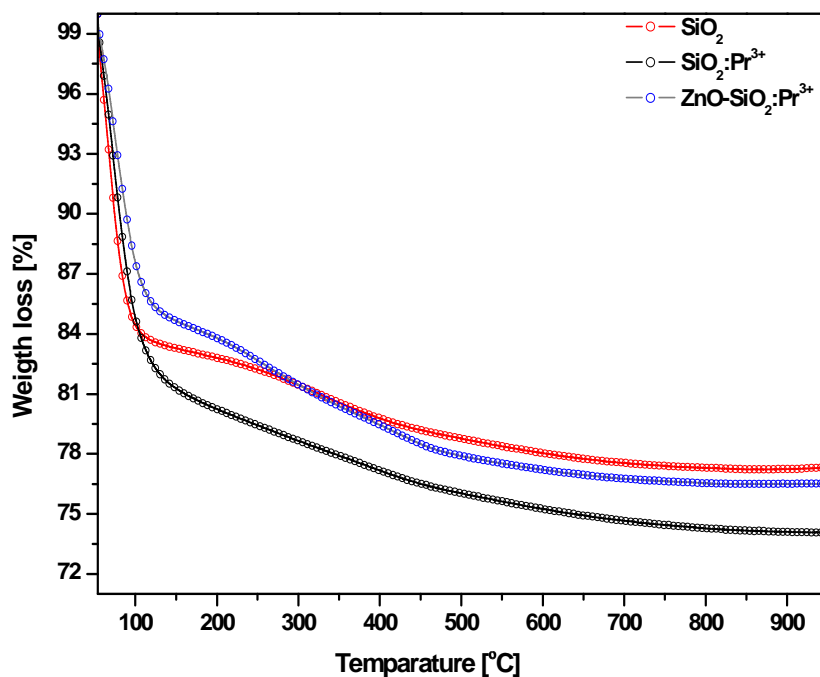


Fig. 4.4 TGA curves of un-doped SiO₂, SiO₂:Pr³⁺ and ZnO:SiO₂:Pr³⁺ phosphor gels. The samples were heated from 50 °C to 950 °C in N₂ atmosphere at a heating rate of 10 °C/min.

4.3.4 Optical absorption and emission properties

The optical absorption spectrum of Pr³⁺ doped and un-doped SiO₂ are presented in figure 4.5. The Pr³⁺ doped SiO₂ revealed four bands in the UV-VIS region all originating from ground state ³H₄ to several excited states of the Pr³⁺ ions. These absorption bands are assigned to ³H₄→³P (*J* = 0, 1, 2), ¹I₆ and ¹D₂ 4*f*² intra-configurational electric dipole transitions of the Pr³⁺. These compare very well with the results reported by several researchers [1,2,8,14-16].

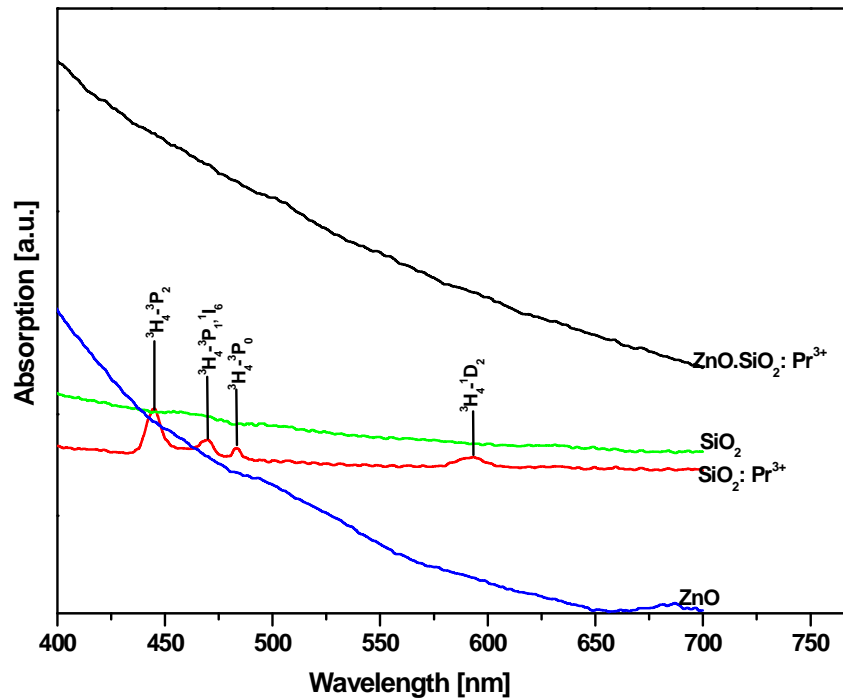


Fig. 4.5 UV-VIS absorption spectra of SiO₂, ZnO, SiO₂: Pr³⁺, and ZnO.SiO₂: Pr³⁺.

PL emission spectra of ZnO nanoparticles and ZnO microparticles dispersed in ethanol after excitation at 325 nm is shown in figure 4.6. The green emission from ZnO nanoparticles associated with recombination of delocalized electrons at singly occupied oxygen vacancies with deep trapped holes [21] was observed at 517 nm. This emission is red shifted from the defects emission of ZnO microparticles at 470 nm which is in good agreement with the results of Ntwaeaborwa *et al.* [21]. It was also noticed that the green emission from the ZnO nanoparticles at 517 nm was more intense compared to that of micron-sized ZnO particles and this is a result of the increase in the surface area-volume ratio due to smaller particle size which could increase the density of surface defects states in ZnO [23].

Direct bandgap emission which can be due to recombination of excitonic centres in ZnO was also observed in both ZnO microparticles and ZnO nanoparticles at 380 nm and 365 nm respectively except that one for ZnO nanoparticles was blue-shifted to lower wavelengths (higher energies) than that of micron-sized ZnO particles. This behaviour could be due to widening of the ZnO nanoparticles bandgap due to quantum confinement of charge carriers in the restricted volume of smaller particles [23].

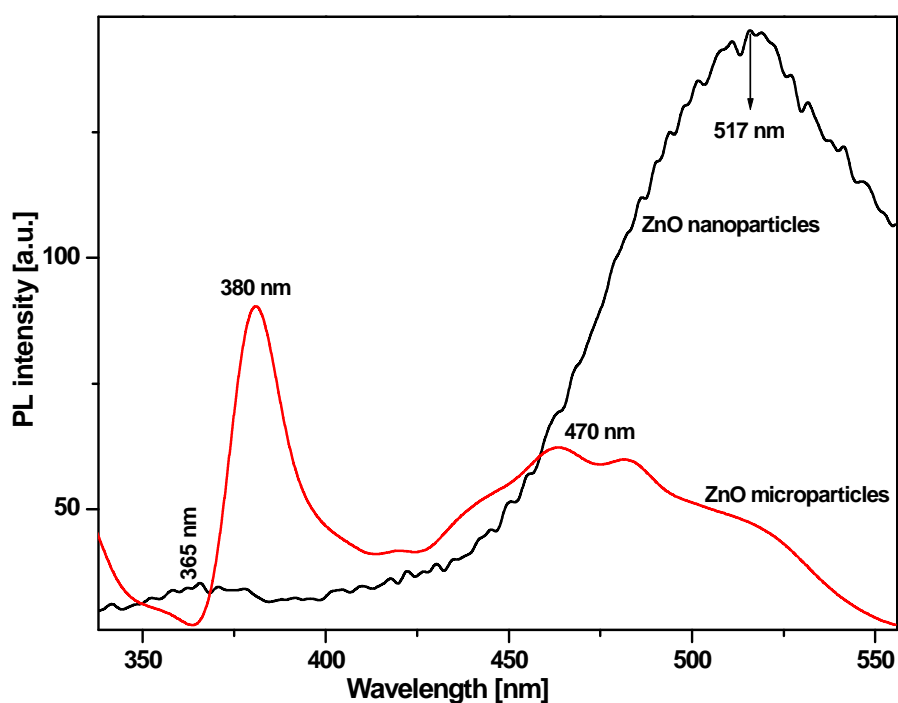


Fig. 4.6 PL emission spectra of ZnO nanoparticles and ZnO microparticles.

The CL spectra of the SiO_2 , $\text{SiO}_2:\text{Pr}^{3+}$, and $\text{ZnO}:\text{SiO}_2:\text{Pr}^{3+}$ nanophosphor powders excited by 2 kV electrons, at 20 μA current density in a high vacuum chamber at a base pressure of $\sim 1.6 \times 10^{-8}$ Torr are shown in figure 4.7. The CL spectrum of SiO_2 showed the emission peak at 445 nm. This peak can be either due to structural defects in the SiO_2 network or charge transfer between O and Si atoms [24].

The characteristic emission peaks with maximum emission at 614 nm that can be associated with transitions in Pr^{3+} were observed from both $\text{SiO}_2:\text{Pr}^{3+}$ and $\text{ZnO}:\text{SiO}_2:\text{Pr}^{3+}$ samples. This emission can be assigned to the transitions originating from the $^3\text{P}_0$ and $^1\text{D}_2$ energy levels to the $^3\text{H}_{(J=6,5,4)}$ and $^3\text{F}_{(J=2,3,4)}$ energy levels all localized in the $4f^2$ intra-configuration of the Pr^{3+} ions. The first two peaks located at 488 nm and 510 nm are associated with the $^3\text{P}_0 \rightarrow ^3\text{H}_4$ transition. Issasi *et al.* [25] reported three stark components from this transition when Pr^{3+} is doped in ZrO_2 . This is followed by a broad emission peak with a dominant emission at 614 nm which is assigned to the $^3\text{P}_0 \rightarrow ^3\text{H}_6$ transition. The shoulders at 590 nm, 635 nm, and 661 nm correspond to $^1\text{D}_2 \rightarrow ^3\text{H}_4$, $^1\text{D}_2 \rightarrow ^3\text{H}_5$, and $^3\text{P}_0 \rightarrow ^3\text{F}_2$ transitions, respectively.

The assignment of these peaks compares well with the fluorescence spectra reported by Annapurna *et al.* [9] and Rai *et al.* [2] for Pr^{3+} doped tellorite glasses. The overlay of the two transitions ($^3\text{P}_0 \rightarrow ^3\text{H}_6$ and $^1\text{D}_2 \rightarrow ^3\text{H}_4$) in Pr^{3+} doped glasses was also observed by Annapurna *et al.* [9]. In order to explain the overlay of both emission transitions, Annapurna *et al.* [9] conducted the decay lifetime measurements of the excited states of the $^3\text{P}_0$ and $^1\text{D}_2$ levels and found that the $^3\text{P}_0$ excited state decayed faster than the $^1\text{D}_2$. This suggests that the luminescence is from the $^1\text{D}_2$ level. According to the observation of Lakshminayana *et al.* [1], the $^3\text{P}_0$ excited state decayed slower than the $^1\text{D}_2$. The reason for such differences may be that the decay time measurements of the rare earths excited states differ from host to host since they strongly depend on the host lattice's phonon energies.

Lakshminarayana *et al.* [1] ascribed the absence of the luminescence from $^1\text{D}_2$ to the large energy gap between the $^3\text{P}_0$ and $^1\text{D}_2$ ($\sim 3858.5 \text{ cm}^{-1}$) resulting in a very small multiphonon non-radiative relaxation from $^3\text{P}_0$ to $^1\text{D}_2$. Such decay lifetime

measurements were not conducted in the present work. The last peak in the NIR region centred at 995 nm is assigned to the $^1D_2 \rightarrow ^3F_4$ transition. However, the peak position is different from the observation of Biswas *et al.* [22]. The defects emission from ZnO nanoparticles at 517 nm was not observed from ZnO.SiO₂:Pr³⁺ emission spectrum. The main emission peak from Pr³⁺ remained stable at 614 nm from both SiO₂:Pr³⁺ and ZnO.SiO₂:Pr³⁺ samples.

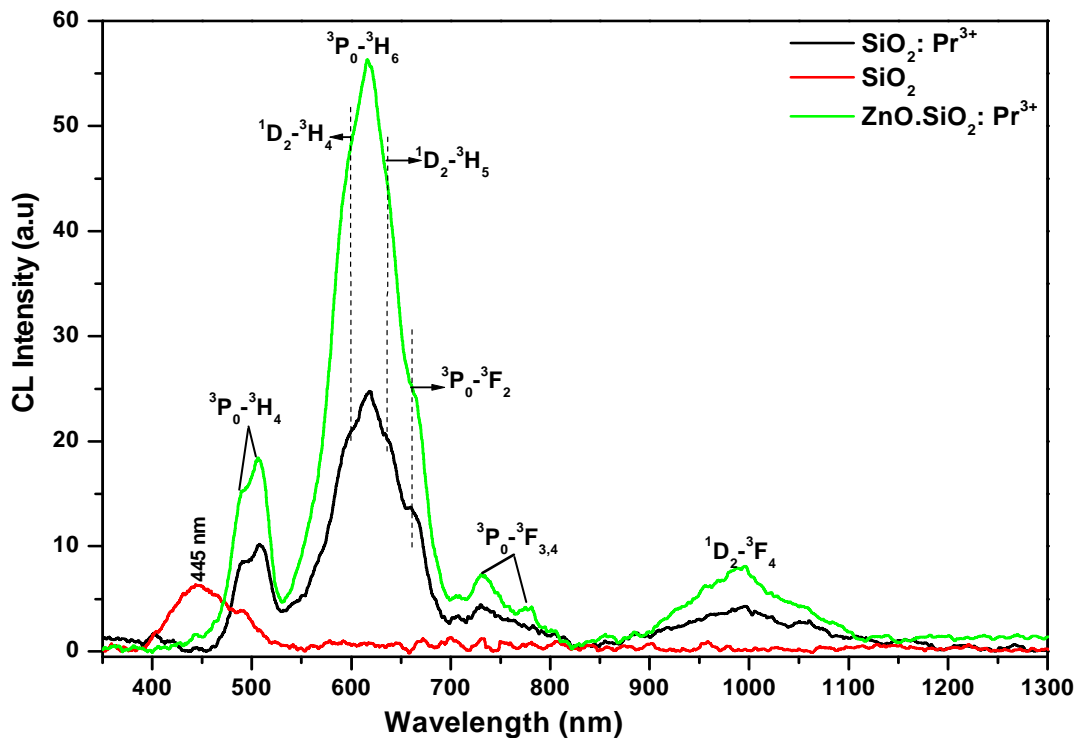


Fig. 4.7 CL spectra of un-doped SiO₂, SiO₂:Pr³⁺ and ZnO.SiO₂:Pr³⁺ irradiated with 2 kV, 20 μA beam of electrons in a high vacuum chamber containing 1.6×10^{-8} Torr.

This confirms that incorporation of the ZnO nanoparticles did not change the radiative process of Pr³⁺ and this further suggest that the ZnO nanoparticles were well dispersed in the SiO₂ matrix [21]. It can also be observed that the blue emission from the host SiO₂ was also suppressed. The increase in the CL intensity of the 614 nm

peak as a result of incorporation of ZnO nanoparticles suggests that energy was transferred from the ZnO nanoparticles to Pr^{3+} ions.

The energy transfer phenomenon between donors and acceptors in phosphors has been long known. This mechanism involves two luminescent centres, a Donor and an Acceptor (A and D) separated by a distance R with a certain interaction (i.e. exchange or multipole-multipole interaction) [3]. For instance, in $\text{ZnO}:\text{SiO}_2:\text{Pr}^{3+}$ the energy transfer takes place from a broad band emitter which is ZnO nanoparticles to a narrow-line absorber Pr^{3+} . This kind of process is only possible for nearest neighbours in the host lattice as reported by Blasse *et al.* [3]. For energy transfer process to occur between the energy donor (ZnO) and acceptor (Pr^{3+}), the distance R between the two must be shorter than the critical distance R_c (the critical distance at which ZnO emission dominates over energy transfer). This therefore means that 1 mol% of ZnO nanoparticle embedded in SiO_2 with 1 mol% of Pr^{3+} has sufficiently short distance for energy transfer to occur. The corresponding energy levels showing possible radiative transitions localized within the Pr^{3+} ion and energy transfer mechanism from ZnO nanoparticles to Pr^{3+} are presented schematically in figure 4.8. The enhancement of CL intensity at 614 nm with ZnO incorporation due to energy transfer process could be due to the fact that the defects states in the ZnO bandgap are filled by bandgap absorption and relaxation to the defects states of ZnO. The energy is therefore transferred possibly by phonon-mediated processes to the $^3\text{P}_0$ state of the Pr^{3+} ion via photoemission from ZnO and complete photocapture by Pr^{3+} , hence the enhanced Pr^{3+} emission was observed [26].

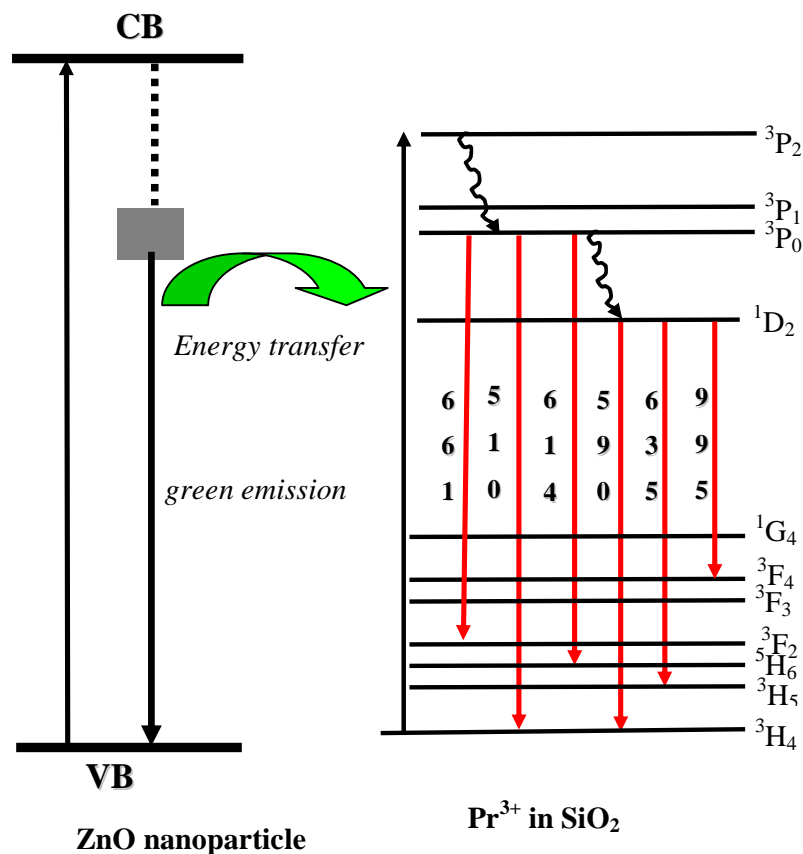


Fig. 4.8 Schematic representation of energy levels diagram depicting mechanism of energy transfer from ZnO nanoparticles and possible transitions in Pr³⁺ doped in SiO₂.

The CL spectra of SiO₂:Pr³⁺ nanophosphor powders irradiated at different accelerating beam voltages (1 to 5 kV) and 8.5 μA in a high vacuum chamber with a base pressure of ~ 1.6 x 10⁻⁸ Torr are shown in figure 4.9. From this figure, it can be seen that with increasing beam voltage from 1 to 5 kV, the CL intensity of the main emission peak at 614 nm first increased continuously up until it reached maximum at 4 kV, then decreased at 5 kV. This is clearly presented in figure 4.10 where the CL intensity is plotted against different accelerating voltages.

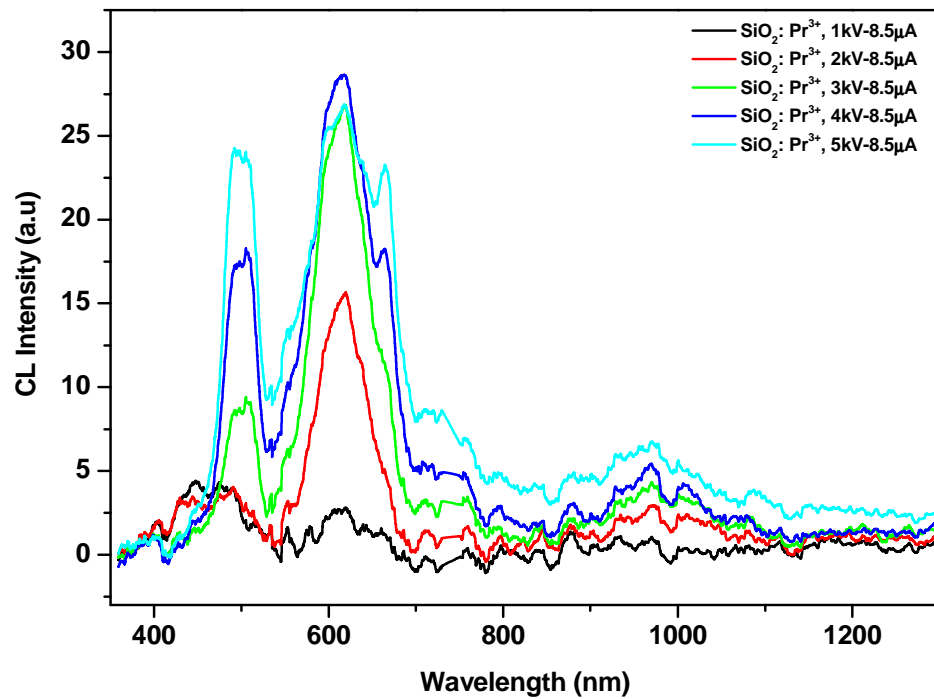


Fig. 4.9 CL spectra of $\text{SiO}_2:\text{Pr}^{3+}$ irradiated with (1-5 kV), $8.5 \mu\text{A}$ beam of electrons in a high vacuum chamber containing a base pressure of $\sim 1.6 \times 10^{-8}$ Torr.

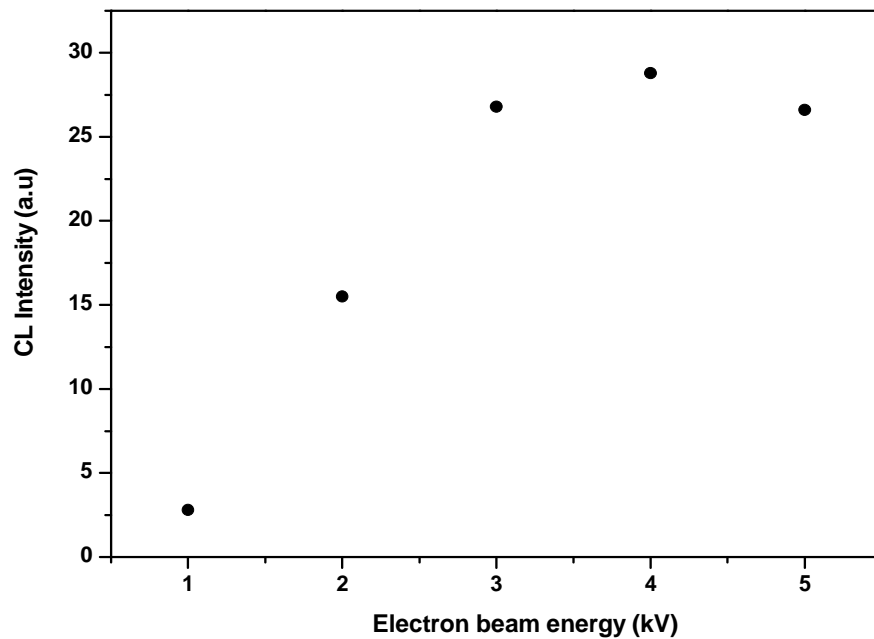


Fig. 4.10 Maximum CL intensity of $\text{SiO}_2:\text{Pr}^{3+}$ 614 nm emission peak as a function of accelerating voltage

Figure 4.11 shows the CL spectra of ZnO:SiO₂:Pr³⁺ nanophosphor powders at an irradiation of different accelerating beam voltages (1 to 5 kV) and 8.5 μA in a high vacuum chamber with a base pressure of ~ 1.6 x 10⁻⁸ Torr. An increase in the CL intensity of the 614 nm peak from ZnO:SiO₂:Pr³⁺ with increasing beam voltage from 1 to 3 kV and its decrease as the voltage was further increased to 4 and 5 kV was observed (see figure 4.12). This further confirms that energy was transferred from ZnO to Pr³⁺.

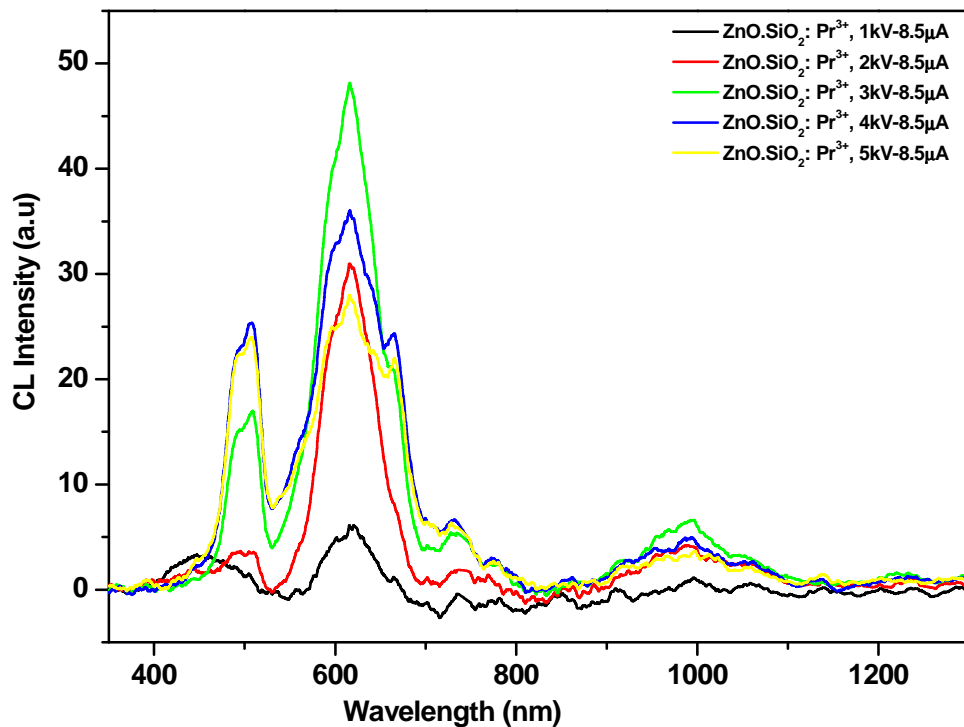


Fig.4.11 CL spectra of ZnO:SiO₂:Pr³⁺ irradiated with (1-5 kV), 8.5 μA beam of electrons in a high vacuum chamber containing a base pressure of ~1.6 x 10⁻⁸ Torr.

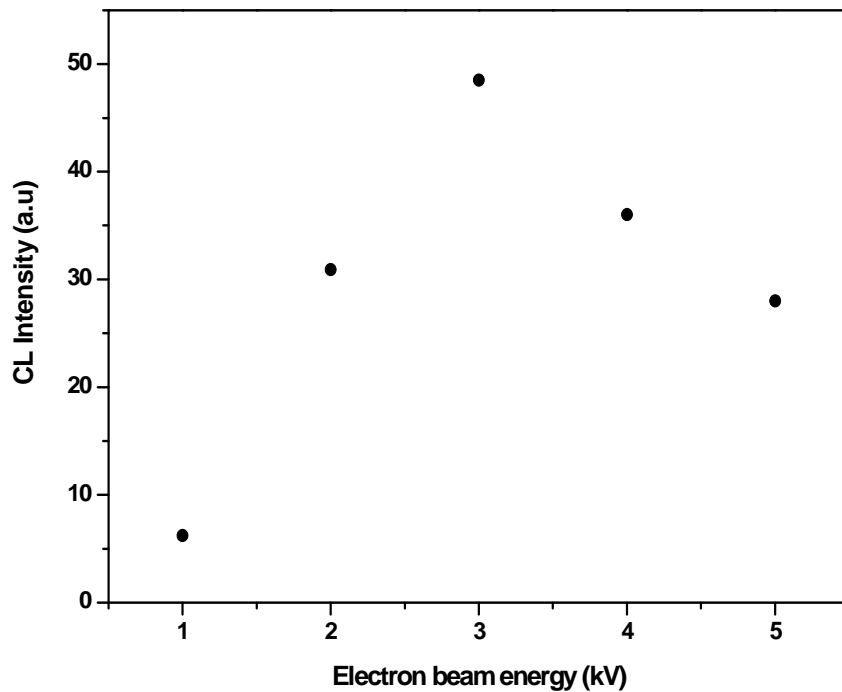


Fig. 4.12 Maximum CL intensity of ZnO:SiO₂:Pr³⁺ 614 nm emission peak at different electron beam voltages.

The CL intensity plotted as a function of electron beam energy follow the same trend as the electron impact ionization cross-section for an atom [27]. The intensity will first increase and then decrease with an increase in electron energy depending on the interaction of the electron with the atom. The decrease at higher energies are however more severe than expected, local heating beneath the beam and quenching due to charging are not excluded at higher energies [27]. The decrease in CL intensity of the main emission peak at 614 nm observed from both phosphors (SiO₂:Pr³⁺ and ZnO:SiO₂:Pr³⁺) with increasing beam voltage can be tentatively explained by thermal quenching which occurs at high temperatures. When the beam voltage increases, the local heating by energetic electrons occurs, and thus temperature also increases which can cause thermal quenching.

During thermal quenching, the thermal vibrations of atoms surrounding an activator ion transfers the energy away from the activator ion at high temperatures resulting in non radiative recombination and a subsequent depletion of the excess energy as phonons in the host lattice. The thermal quenching mechanism is clearly explained by the configuration co-ordinate model [28] in chapter 2.

4.3.5 CL degradation

The CL spectra from the $\text{SiO}_2:\text{Pr}^{3+}$ phosphor and the $\text{ZnO}:\text{SiO}_2:\text{Pr}^{3+}$ phosphor before and after electron bombardment at an irradiation of 2 kV, 20 μA in an O_2 pressure of 1×10^{-7} Torr backfilled from a vacuum base pressure of 1.6×10^{-8} Torr are shown in figure 4.13 (a) and (b), respectively. As shown in figures 4.13 (a) and (b), the CL intensity of the 614 nm peak was quenched completely as a result of 2kV electron bombardment.

The Auger spectra of $\text{SiO}_2:\text{Pr}^{3+}$ and $\text{ZnO}:\text{SiO}_2:\text{Pr}^{3+}$ phosphors before and after degradation indicated in figure 4. 14 (a) and (b) revealed the Auger peaks of Si (79 eV), C (267 eV) and O (505 eV), respectively. It was noticed that with prolonged electron bombardment of the SiO_2 , the Auger peak intensity of Si and O decreased while that of adventitious C completely disappeared. The similar observation was reported by Ntwaeaborwa *et al.* [29]. Thomas *et al.* [30] reported the decrease in the Auger peak intensities of Si and O and the appearance of a new Auger peak located at ~ 92 eV associated with elemental Si. Ntwaeaborwa *et al.* [29] and Thomas *et al.*[30] reported that, the elemental Si in the SiO_2 compound can be shifted from higher energy (92 eV) to lower energy (75-80 eV), and this can be attributed to the change in the density of states and some relaxation effects involved. In the current study, we observed a slight Si peak shift towards higher energy. Dhlamini *et al.* [31], assigned

the change in Si peak shape before and after degradation to the development of the extra peaks of SiO_x ($0 < x < 2$) by the electron bombardment. These extra SiO_x peaks were confirmed by XPS.

Figure 4.14 (a) and (b) show the changes in the Auger peak-to-peak heights (APPH's) of Si, O, and C from $\text{SiO}_2:\text{Pr}^{3+}$ and $\text{ZnO}:\text{SiO}_2:\text{Pr}^{3+}$ phosphors, respectively, together with the CL intensity as a function of coulomb dose during 2 keV, 20 μA electron bombardment at 1×10^{-7} Torr of O_2 backfilled from a vacuum base pressure of 1.6×10^{-8} Torr. It was noticed that the concentration of adventitious C on the surface was very small in both figures 4.15 (a) and (b). The electron bombardment resulted in the decrease in O peak intensity while those of Si and C remained almost unchanged. The decrease in CL intensity as a result of electron bombardment was also observed from both $\text{SiO}_2:\text{Pr}^{3+}$ and $\text{ZnO}:\text{SiO}_2:\text{Pr}^{3+}$ phosphors as indicated in figure 4.14 (a) and (b). The correlation between the decrease of CL intensity and of the Auger peak intensity from O was recognized from this observation. Based on previous reports, this can be due to desorption of O from the surface following the electron-beam dissociation of SiO_2 [29].

Ntwaeaborwa *et al.* [29], Dhlamini *et al.* [31] attributed desorption of O_2 from the surface to electron stimulated surface chemical reactions (ESSCR). With prolonged electron bombardment, it is reported that the Si-O bonds are broken and free oxygen is released as ions following a reaction with dissociated species (eg C, H, or O) from vacuum ambient gasses (e.g) H_2O , O_2 , and CO_2 [2129, 31]. The ESSCR mechanism can also result in reduction of the radiative efficiency of the activators as it can cause incorporation of O iso-electronic traps in the near surface region. In the present results we could not observe the new Auger peak associated with elemental Si

at 92 eV in the Auger spectra after an electron of 27 C/cm^2 as documented by Thomas *et al.* and it could be that the desorption of oxygen resulted in the formation of an oxygen-deficient surface dead layer of SiO_x , where $x < 2$ consistent with the data reported in ref [29].

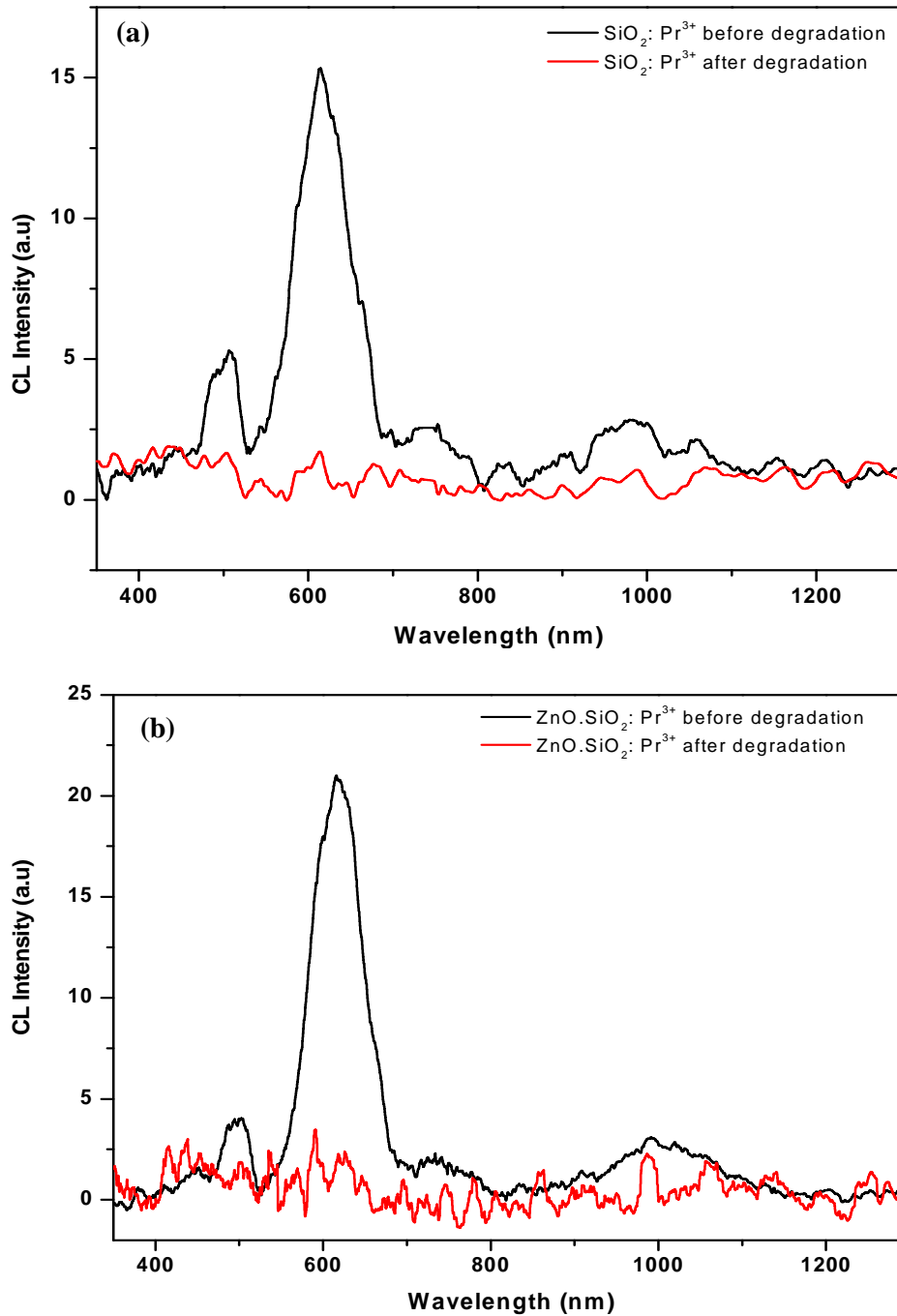


Fig 4.13 CL spectra of (a) $\text{SiO}_2:\text{Pr}^{3+}$ and (b) $\text{ZnO}.\text{SiO}_2:\text{Pr}^{3+}$ before and after electron bombardment by 2 kV, 20 μA in 1×10^{-7} Torr of O_2 .

It is therefore reasonable to conclude that the SiO_x dead layer formed on the surface could be the main reason for degradation of the CL intensity of the $\text{SiO}_2:\text{Pr}^{3+}$ and $\text{ZnO}:\text{SiO}_2:\text{Pr}^{3+}$ phosphors.

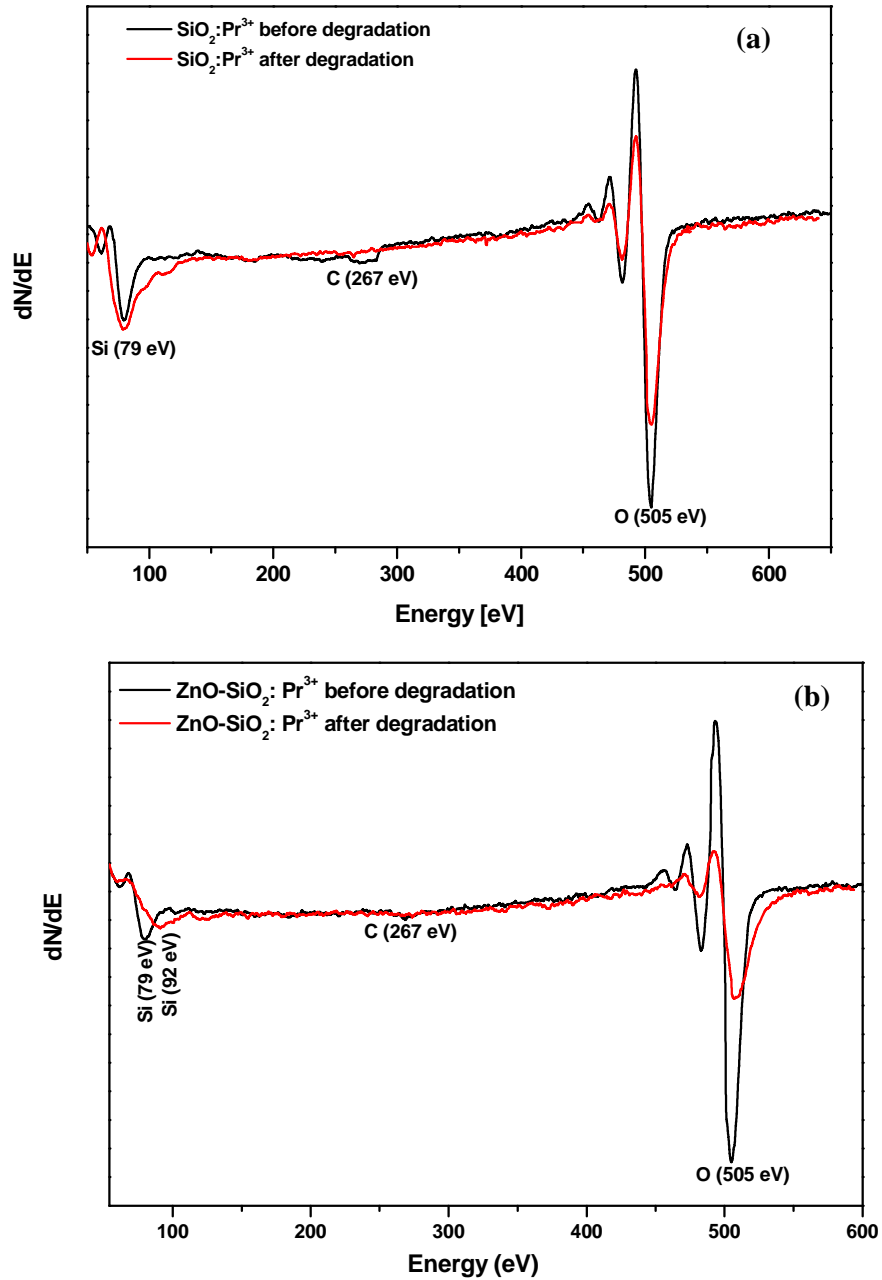


Figure 4.14 AES spectra of (a) $\text{SiO}_2:\text{Pr}^{3+}$ and (b) $\text{ZnO}:\text{SiO}_2:\text{Pr}^{3+}$ before and after degradation at 2 kV, 20 μA , in 1×10^{-7} Torr of O_2 .

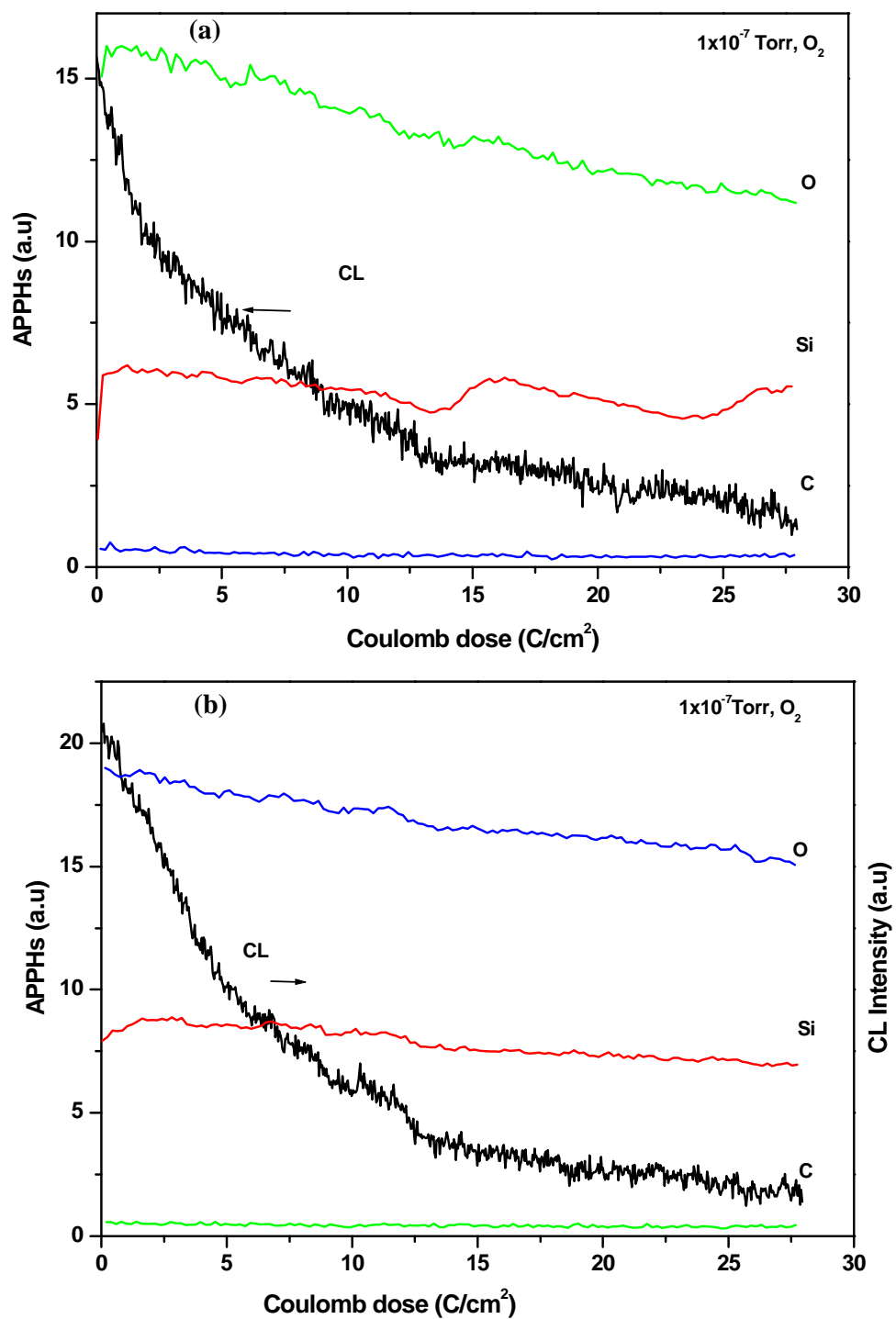


Figure 4.15 AES peak-to-peak heights of (a) SiO₂:Pr³⁺ and (b) ZnO.SiO₂:Pr³⁺ at 2 kV, 20 μA, in 1 × 10⁻⁷ Torr of O₂ as a function of electron dose.

4.4 CONCLUSION

The ZnO nanoparticles with an average crystallite size of ~ 4 nm as estimated from Scherrer's equation were successfully incorporated in Pr^{3+} doped SiO_2 nanophosphor using a sol gel method. Enhanced red emission centred at 614 nm attributed to ${}^3\text{P}_0 \rightarrow {}^3\text{H}_6$ transition of Pr^{3+} was obtained from $\text{ZnO}:\text{SiO}_2:\text{Pr}^{3+}$. The green emission from ZnO at ~ 530 nm was completely suppressed due to the non-radiative transfer of energy from ZnO to Pr^{3+} . The effect of the beam voltage in the CL intensity from both $\text{SiO}_2:\text{Pr}^{3+}$ and $\text{ZnO}:\text{SiO}_2:\text{Pr}^{3+}$ was demonstrated. The degradation mechanism of the CL intensity of $\text{SiO}_2:\text{Pr}^{3+}$ and $\text{ZnO}:\text{SiO}_2:\text{Pr}^{3+}$ phosphor powders was discussed.

4.5 REFERENCES

- [1] G. Lakshminarayana, J. Qiu, *J. Alloys Compd.* 476 (2009) 470-476
- [2] V. K. Rai, K. Kumar, S. B Rai, *Opt. Mater.* 29 (2009) 873-878
- [3] G. Blasse, B.C. Grabmaier, *Luminescent Materials*, Springer:Verlag, Berlin (1994)
- [4] E. Pinel, P. Boutnaud, R. Mahiou, *J. Alloys Compd.* 374 (2004) 165-168
- [5] R. Balda, M. Voda, M. Al-Saleh, J. Fernandez, *J. Lumin.* 97 (2002) 190-197
- [6] M.A. Gusowski, G. Dominiak-Dzik, P. Solarz, R. Lisiecki, W. Ryba-Romanowski, *J. Alloys Compd.* 438 (2007) 72-76
- [7] W. Seeber, E.A. Downing, L. Hesselink, M.M. Fejer, D. Ehrt, *J. Non-Cryst. Solids* 189 (1995) 218-226
- [8] W. Strek, J. Legendziewicz, E. Lukowiak, K. Maruszewski, J. Sokolnicki, A.A. Boiko, M. Borzechowska, *Spectrochim. Acta Part A* 54 (1998) 2215-2221
- [9] K. Annapurna, R. Chakrabarti, S. Buddhudu, *J. Mater. Sci* (2007) 42: 6755-6761
- [10] Z. Mazurak, W.A. Pisarski, J. Gabrys-Pisarska, and M. Zelechower, *Phys. Status Solidi B* 237 [2] (2003) 581-591
- [11] L. Del Longo, M. Ferrari, E. Zanghellini, M. Bettinelli, J.A. Capobianco, M. Montagna, F. Rossi, *J. Non-Cryst. Solids* 231 (1998) 178-188
- [12] A. Ravi Kumar, N. Veeraiah, B. Appa Rao, *J. Lumin.* 75 (1997) 57-62
- [13] X-jun Wang, S.H. Huang, R. Reeves, W. Wells, M.J. Dejneka, R.A. Meltzer, W.M. Yen, *J. Lumin.* 94-95 (2001) 229-233
- [14] G. De, A. Licciulli, M. Nacucchi, *J. Non-Cryst. Solids* 201 (1996) 153-158
- [15] A.A. Boiko, E.N. Poddenezhny, E. Lukowiak, W. Strek, J. Sokolnicki, and J. Legendziewicz, *J. Appl. Spectrosc.* 62 [4] (1995)
- [16] A. Biswas, S. Chakrabarti, H.N. Acharya, *Mater. Sci. Eng.* B49 (1997) 191-196

- [17] H.C Swart and A.P. Greeff, *Surf. Interface Anal.* 2004, 36: 1178-1180
- [18] [20] P. Psuja, D. Hreniak, and W. Strek, *J. Nanomater.* (2007) 81350
- [19] P.V. Kamat, B. Patrick, *J. Phys. Chem.* 96 (1992) 6829-6834
- [20] A. Van Dijken, J. Makkinje, A. Meijerink, *J. Lumin.* 92 (2001) 323-328
- [21] O.M. Ntwaeaborwa, and P.H. Holloway, *J. Nanotechnol.* 16 (2005) 865-868
- [22] A. Biswas, H.N. Acharya, *Mater. Res. Bull.* 32 [11] (1997) 1551-1557
- [23] M.S. Dhlamini, O.M. Ntwaeaborwa, H.C. Swart, J.M. Ngaruiya, K.T. Hillie, *Physica B* 404 (2009) 4409-4410
- [24] C. de Mello Donega, A. Meijerink, and G. Blasse, *J. Appl. Spectrosc.* 62, [4] (1995)
- [25] J. Isasi-Marin, M. Perez-Estebanez, C. Diaz-Guera, J.F. Castillo, V. Correcher, and M.R. Cuervo-Rodriguez, *J. Phys. D: Appl. Phys.* 42 (2009) 075418
- [26] J. Bang, H. Yang, and P.H. Holloway, *J. Chem. Phys.* 123 (2005) 84709
- [27] H.C. Swart, L. Oosthuizen, P.H. Holloway, and G.L.P Berning, *Surf. Interface Anal.* 26 (1998) 337-342
- [28] H.C. Swart, K.T. Hillie and A.P. Greeff, *Surf. Interface Anal.*, 32 (2001) 110-113
- [29] O.M. Ntwaeaborwa, H.C. Swart, R.E. Kroon, P.H. Holloway, J.R. Botha, *J. Chem. Phys. Sol.* 67 (2006) 1749-1753
- [30] S. Thomas, *J. Appl. Phys.* 45 [1] (1974)
- [31] M.S. Dhlamini, J.J. Terblans, O.M. Ntwaeaborwa and H.C. Swart, *Surface Rev. Lett.* 14 [4] (2007) 697-701

**LUMINESCENCE DEPENDENCE OF Pr³⁺ ACTIVATED
SiO₂ NANOPHOSPHOR ON Pr³⁺ CONCENTRATION,
TEMPERATURE AND ZnO INCORPORATION****5.1 INTRODUCTION**

Self-quenching of the luminescence from the ¹D₂ or ³P₀ emitting levels of Pr³⁺ is a commonly observed phenomenon and because of that it has been a challenge to optimize the luminescence efficiency resulting from transitions in these levels. A few reasons which could lead to this quenching effect are: (i) multiphonon relaxation, (ii) cross relaxation within Pr³⁺ ion pairs, and (iii) energy migration to quenching centres [1]. The last two processes depend on the Pr³⁺ concentration.

Much interest has also been focused on semiconductor nanocrystals, "quantum dots", as they are considered as another good choice as sensitizing centres for radiative relaxation of activator ions since their excitation cross sections are very high due to the efficient band-to-band absorptions. Rare earth ions doped glass matrices containing semiconductor nanocrystals prepared by the sol-gel method have been previously reported [2,3,4]. The enhanced luminescence of rare earth ions was achieved by efficient energy transfer from semiconductor quantum dot to rare earth ions. This may lead to enhanced luminescence efficiency which is good for PDP technology. In the present chapter, we report the enhanced emission of Pr³⁺ induced by energy transfer from ZnO nanoparticles incorporated in situ in sol-gel silica. Luminescence decay curves measurements were also performed to determine the lifetimes of the ¹D₂ state of Pr³⁺ at different temperatures. The effects of temperature

on the 1D_2 multiplet lifetime as well as the self-quenching of 1D_2 emission with increasing Pr^{3+} concentration were investigated. The possible mechanism of energy transfer between ZnO and Pr^{3+} in SiO_2 host is also discussed.

5.2 EXPERIMENTAL

The phosphor powders were produced using the experimental procedure presented in chapter 4.2.

The excitation and emission spectra of the $SiO_2:Pr^{3+}$ and $ZnO:SiO_2:Pr^{3+}$ phosphor powders were recorded at the Deutsche Elektronen Synchrotron (DESY) in Hamburg, Germany using the setup at SUPERLUMI experimental station of HASYLAB. Lifetime measurements were obtained using an optical parametric oscillator (OPO Continuum Surelite) pumped by third harmonics of Nd:YAG laser as an excitation source. The decay signals were detected, and stored with a Tektronix TDS 3052 digital oscilloscope. The measurements were carried out at liquid-helium temperatures using a cryostat (CF-1204 Oxford Instruments) on a continuous flow mode. PL spectra from the micro- and nano-sized ZnO particles suspended in ethanol were recorded using a LS 55, Fluorescence spectrometer.

5.3 RESULT AND DISCUSSION

5.3.1 Particle morphology (HRTEM)

Figure 5.1 (a) shows the transmission electron microscopy (TEM) image of ZnO nanoparticles. Shown in the image is an agglomeration of hexagonal particles. The estimated average size of the particles was 4 nm in diameter. Fig. 5.1 (b) presents the high resolution (HRTEM) image which shows the bands in different directions indicating that individual particles were randomly distributed. Also, the lattice fringes of the hexagonal ZnO were clearly shown in this image. Further analysis on this

image resulted in a measured d -spacing of 2.6 \AA which corresponds to the ZnO (110) plane.

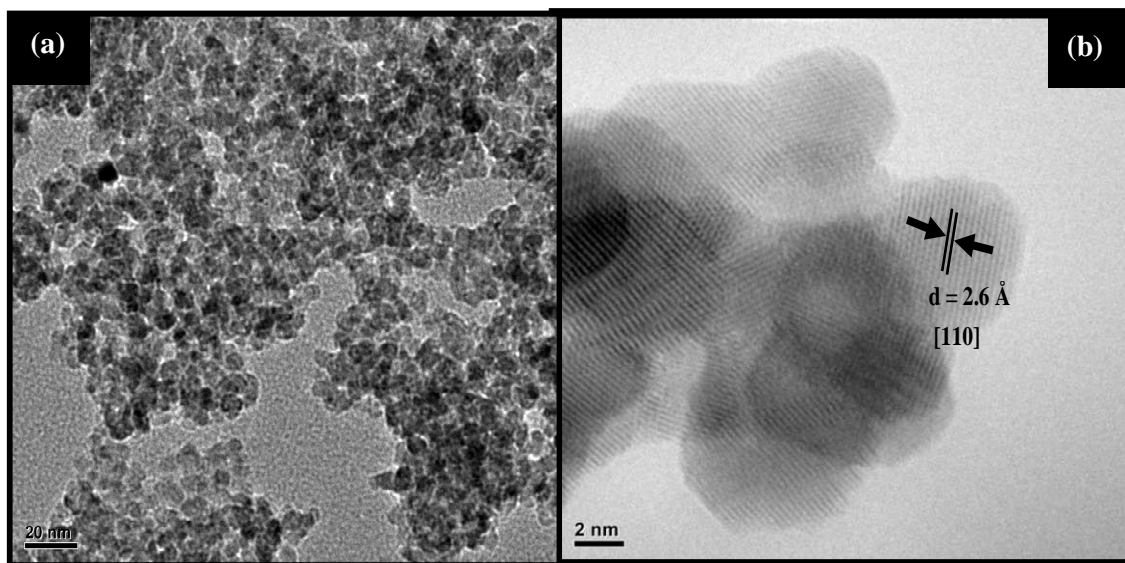


Fig. 5.1 (a) TEM and (b) HRTEM images of the clustered ZnO nanoparticles

The presence of clusters of doped ions or particles incorporated in amorphous silica matrix was confirmed by the EDS and TEM data. Figure 5.2 (a) is the TEM image of amorphous SiO_2 . The field emission scanning electron microscopy image showed that SiO_2 was constituted by an agglomeration of spherical particles (see fig. 4.3). Figure 5.2 (b) shows the TEM image of $\text{ZnO}:\text{SiO}_2:\text{Pr}^{3+}$. It shows relatively small particles homogeneously distributed in amorphous SiO_2 . The insert of figure 5.2 (b) shows that these particles were spherical with sizes ranging from 2 – 10 nm in diameter. As confirmed by the EDS data in figure 5.3, the particles in the TEM image of figure 5.2 (b) composed of Si, O, Zn, and Pr elements. This confirms the successful incorporation of Pr^{3+} and ZnO nanoparticles in the SiO_2 host. Similar results were reported by Yu *et al.* [5] when they observed a uniform dispersion of particles of Eu^{3+} and ZnO co-doped in SiO_2 .

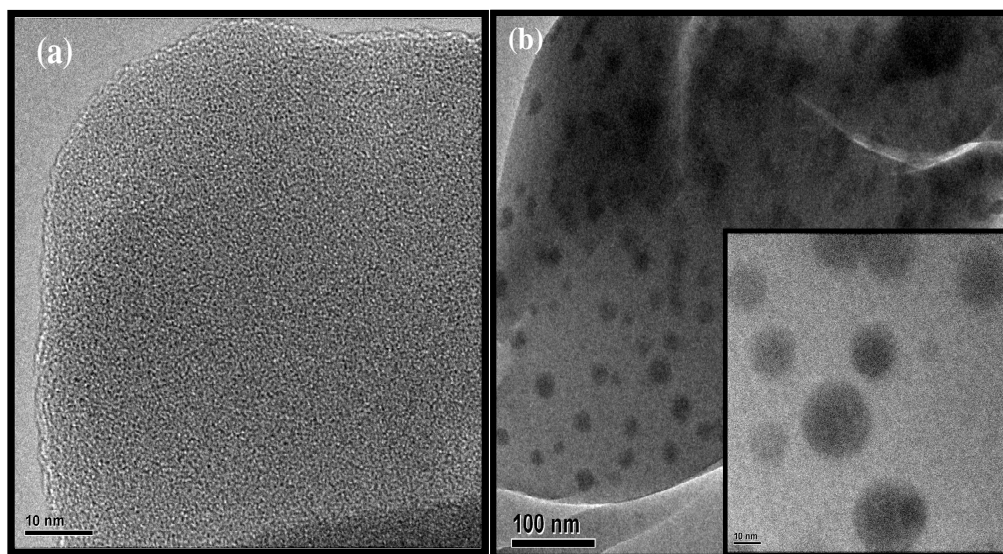


Fig. 5.2 TEM images of (a) SiO₂ nanoparticles, (b) ZnO.SiO₂:Pr³⁺ nanophosphor and the insert of HRTEM image of ZnO.SiO₂:Pr³⁺.

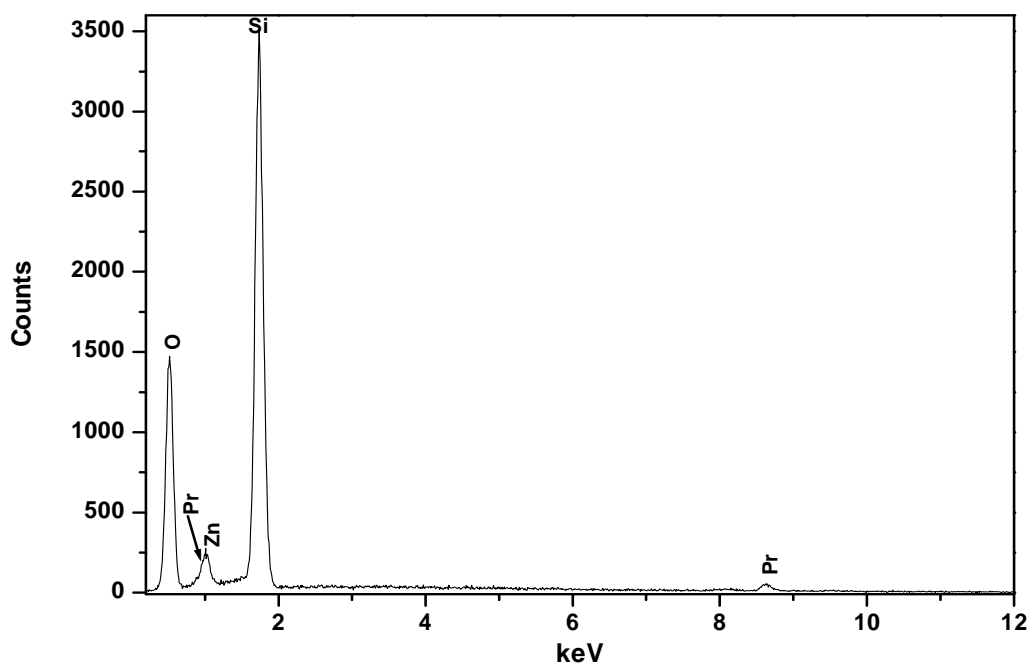


Fig. 5.3 Energy dispersive X-Ray spectrum of 1 mol% ZnO.SiO₂:0.2 mol% Pr³⁺ phosphor.

5.3.2 PL properties of Pr³⁺ singly doped SiO₂

In principle, there are two types of emission transitions from Pr³⁺ that can occur with VUV excitation, namely, inter-configurational $4f5d \rightarrow 4f^2$ or intra-configurational $4f^2 \rightarrow 4f^2$. The energetic location of the $4f5d$ states relative to the 1S_0 state strongly depends on a host. If the lowest $4f5d$ state lies below the 1S_0 state, the high energetic excitation will stimulate the broad emission from the lowest $4f5d$ state, which is parity-allowed inter-configurational $4f5d \rightarrow 4f^2$ transition. For example, Vink *et al.* [6] reported the strong emission bands in the UV region from 200 to 300 nm due to parity-allowed $4f^15d^1 \rightarrow 4f^2$ transitions of Pr³⁺ for CaSO₄:Pr³⁺ phosphor after VUV excitation at 190 nm. According to Vink *et al.* [6], such results suggest that the $4f^15d^1$ levels lie below the 1S_0 level. However, when Pr³⁺ was doped in SrSO₄ and BaSO₄ systems, the narrow emission peak around 400 nm from 1S_0 level was observed and this suggests that the $4f^15d^1$ levels lie above the 1S_0 level.

The PL excitation and emission spectra of SiO₂:0.2 mol% Pr³⁺ are presented in figure 5.4. The excitation spectrum was measured monitoring Pr³⁺ emission at 605 nm using synchrotron radiation. This spectrum shows the weak bands around spectral region between 140 and 240 nm. These bands can be ascribed to transitions from the $4f^2$ ground state to the lowest $4f5d$ sublevels of Pr³⁺ considering the fact that the Pr³⁺ \rightarrow O²⁻ charge transfer transitions which might occur appear at substantially short wavelengths. The assignment of these bands compares well with the results of Ryba-Romanowski *et al.* [7], van der Kolk *et al.* [8], Fu *et al.* [9], Ivanovskikh *et al.* [10], and Bo *et al.* [11] for Pr³⁺ doped in different host matrices. The excitation efficiency increases again below 100 nm for excitation at 90 nm. This agrees well with the observation of Ivanovskikh *et al.* [10] where they found the excitation efficiency

$\text{Ca}_3\text{Sc}_2\text{Si}_3\text{O}_{12}:0.2\%\text{Pr}^{3+}$ to significantly increase for excitation at 75 nm while it was very weak in the spectral region between 85 to 160 nm.

The first broad emission peak centred at 309 nm in the UV spectral region presented in the emission spectrum in figure 5.4 corresponding to the parity-allowed transitions from the lowest excited state of the $4f^2$ configuration to the ${}^3\text{H}_{4,5,6}$ and ${}^3\text{F}_2$ of the $4f^2$ configuration was observed [7,8,12]. These results are in good agreement with the results of You *et al.* [12] for Pr^{3+} doped in YBO_3 system. This blue emission peak is followed by emission peaks in the orange, red and IR region which can be assigned to transitions originating from the ${}^3\text{P}_0$ and ${}^1\text{D}_2$ levels to the ${}^3\text{H}_{4,5,6}$ and ${}^3\text{F}_{2,3,4}$. The broad band which was observed in the region of 600 to 630 nm with prominent red emission peak centred at 605 nm can be assigned to ${}^1\text{D}_2 \rightarrow {}^3\text{H}_4$ transition of Pr^{3+} .

The small shoulders around 614 and 660 nm correspond to the ${}^3\text{P}_0 \rightarrow {}^3\text{H}_6$ and ${}^3\text{P}_0 \rightarrow {}^3\text{F}_2$ transitions, respectively. The assignment of these emission peaks compares well with the results reported by Annapurna *et al.* [13] and Rai *et al.* [14] for Pr^{3+} doped in tellorite glasses. The emission peaks centred at 890 and 1005 nm corresponds to the ${}^1\text{D}_2 \rightarrow {}^3\text{F}_2$ and ${}^1\text{D}_2 \rightarrow {}^3\text{F}_{3,4}$ transitions. These were also reported by Biswas *et al.* [15] for Pr^{3+} doped in SiO_2 around 884 and 1060 nm.

Figure 5.5 (a) and (b) shows the luminescence decay curves of Pr^{3+} (${}^3\text{P}_0 \rightarrow {}^3\text{H}_6$ and ${}^1\text{D}_2 \rightarrow {}^3\text{H}_4$ transitions) emission. The lifetimes computed from the decay curve data obtained using the first order exponential fitting were 1.8 μs and 179 μs for ${}^3\text{P}_0$ and ${}^1\text{D}_2$, respectively. It is obvious from these results that the ${}^3\text{P}_0$ level of Pr^{3+} decays faster than the ${}^1\text{D}_2$ level, hence its lifetime was much shorter. Similar results were reported by Balda *et al.* [2] and Annapurna *et al.* [13]. Such results confirm the existence of the simultaneous emissions from ${}^3\text{P}_0$ and ${}^1\text{D}_2$ levels [2, 13].

The self-quenching of the 1D_2 luminescence of Pr^{3+} has been observed in many Pr^{3+} doped systems including crystals and glasses [1-3]. The luminescence decay curves of the 1D_2 level were also recorded as a function of different Pr^{3+} concentrations in SiO_2 at room temperature as shown in figure 5.6. The 1D_2 level was directly excited in order to avoid the overlap in emission from the 1D_2 and 3P_0 states which occurs when exciting into the 3P_J states.

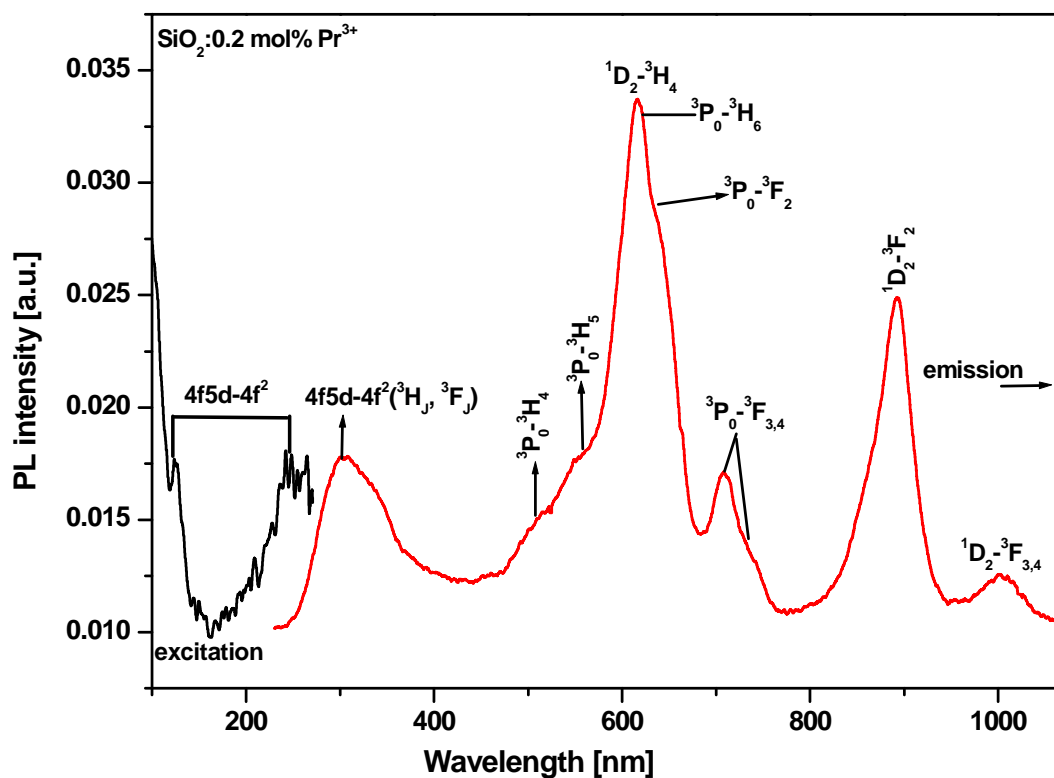


Fig. 5.4 VUV excitation spectrum and emission spectrum of 0.2 mol% Pr^{3+} single doped SiO_2 .

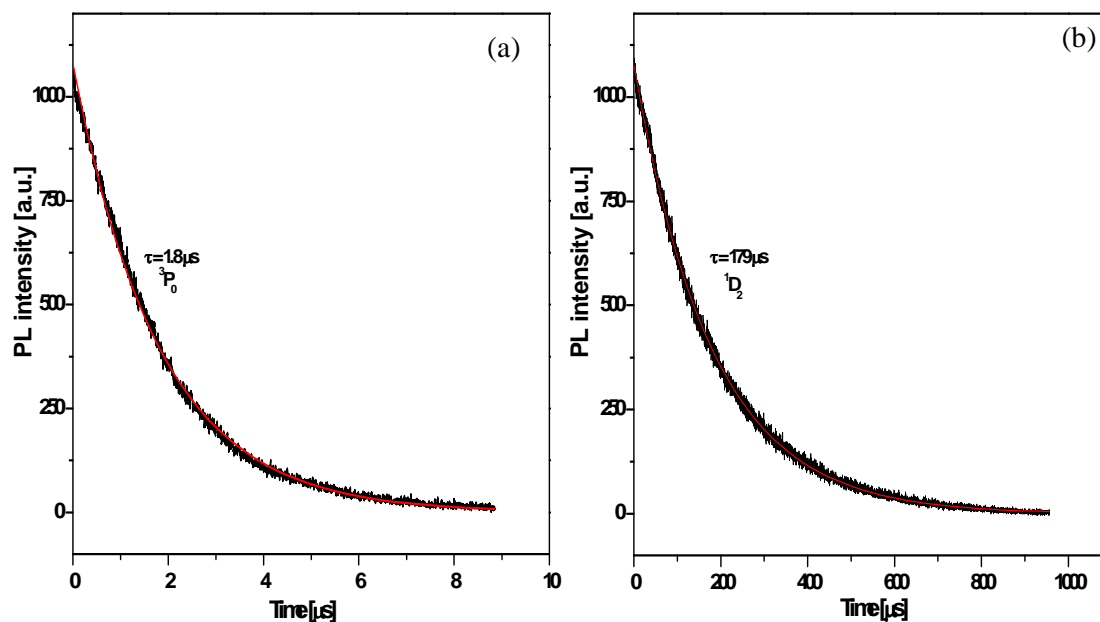


Fig. 5.5 Luminescence decay curves of the 3P_0 and 1D_2 levels of Pr^{3+} (0.2 mol%) in SiO_2 obtained at 8 K. The solid black line corresponds to the experimental data and the solid red line is the fit to a single exponential.

It was noticed that the fluorescence intensity from the $Pr^{3+} \ ^1D_2 \rightarrow \ ^3H_4$ emission decayed slowly for 0.05, 0.1, and 0.2 Pr^{3+} concentrations and the lifetimes computed from the decay curves using a single exponential fitting were 138, 141, and 144 for 0.05, 0.1, and 0.2, respectively. However, when the Pr^{3+} concentration was further increased to 0.5 mol%, the $Pr^{3+} \ ^1D_2 \rightarrow \ ^3H_4$ emission decayed faster to a great extent with the lifetime of 123 μs . Similar observations have been previously reported [1, 3]. Del Longo *et al.* [1] reported the lifetime decrease of the 1D_2 level with increasing Pr^{3+} concentration (0.5, 1, and 2 %) in zinc borate glass.

Balda *et al.* [2] also reported the shortening of lifetimes of the 1D_2 level with increasing Pr^{3+} concentration (0.1, 0.5, and 1 mol%) in fluorophosphates glass. The characteristic decay process of the 1D_2 emitting level of Pr^{3+} ions is governed by a sum of probabilities for several competing processes, namely, radiative decay, non-radiative decay by multi-phonon relaxation, and non-radiative decay by energy transfer to the Pr^{3+} ions [3]. Due to the large energy gap between the 1D_2 and 1G_4

energy levels, the non-radiative ${}^1D_2 \rightarrow {}^1G_4$ multi-phonon relaxation is expected to be small [1-3]. Furthermore, the concentration dependence may indicate that in the depopulation of the 1D_2 state, the energy transfer processes are dominant over multi-phonon processes involving a single ion. In highly concentrated systems, ion-ion interaction brings about cross relaxation among Pr^{3+} ions and migration of the excitation energy from one Pr^{3+} ion to another through energy transfer processes among Pr^{3+} ions and finally to a quenching centre thus leading to self-quenching of luminescence [2,7,16,17]. This process in particular becomes efficient when the energy levels structure of luminescent ions allows for cross-relaxation process.

However, if the rate of migration of excitation energy is small with respect to cross-relaxation rate, the luminescence decay curves are no longer exponential as documented by Ryba-Romanowski *et al.* [7]. In a case where excitation migration energy is fast, the donor-acceptor system becomes more uniform while the luminescence decay curves follow the single exponential time dependence. In the current results, the single exponential luminescence decays were recorded with 0.05, 0.1, 0.2 and 0.5 mol% Pr^{3+} concentrations in SiO_2 samples suggesting that the rate of excitation energy migration is higher than the rate of cross-relaxation processes involved.

Migration of the excitation energy through resonance energy transfer among Pr^{3+} ions and finally to the quencher centre could therefore be the main reason for concentration quenching of fluorescence leading to fast lifetime decrease Pr^{3+} concentrations above 0.2 mol%.

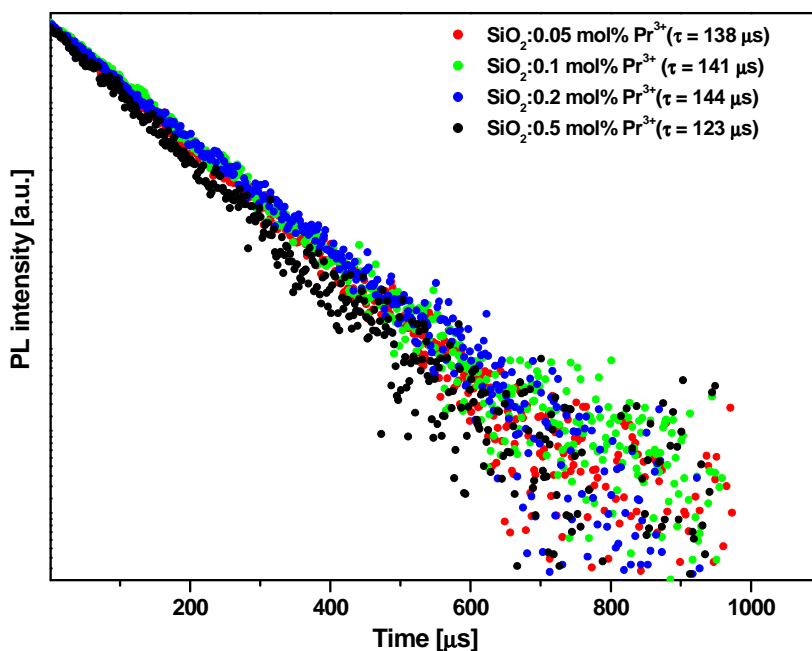


Fig. 5.6 Luminescence decay curves of the ${}^1D_2 \rightarrow {}^3H_4$ emission for various concentrations of Pr^{3+} (0.2 mol%) in SiO_2 .

Figure 5.7 shows the decay curves of luminescence originating from the 1D_2 level collected when the temperature was varied from 8 to 300 K under direct excitation of the 1D_2 using a pulsed laser. As shown in the figure, the luminescence decay curves followed the single exponential with the 1D_2 lifetime gradually decreasing from 179 μs at 8 K to 148 μs at 300 K. Temperature dependence of the 1D_2 lifetime has previously been reported [2-4,16].

The temperature dependent process is predicted when the condition of resonance is satisfied for transitions originating in thermally populated crystal field components of the ground state of acceptor ions. If not, the energy mismatch has to be assisted by lattice phonons while the temperature influences the rate of the cross relaxation [4]. The decrease of the 1D_2 lifetime with increasing temperature between 8 K and 300 K cannot be assigned to non-radiative decay through multi-phonon relaxation, but rather to contribution from non-resonant cross relaxation process as the

rate of multi-phonon decay of 1D_2 level is negligible in most of the hosts matrices compared to that of radiative decay due to the large energy gap between 1D_2 and 1G_4 [2,4]. The cross relaxation mechanism involved during self-quenching process is believed to proceed through intermediate 1G_4 and 3F_4 levels.

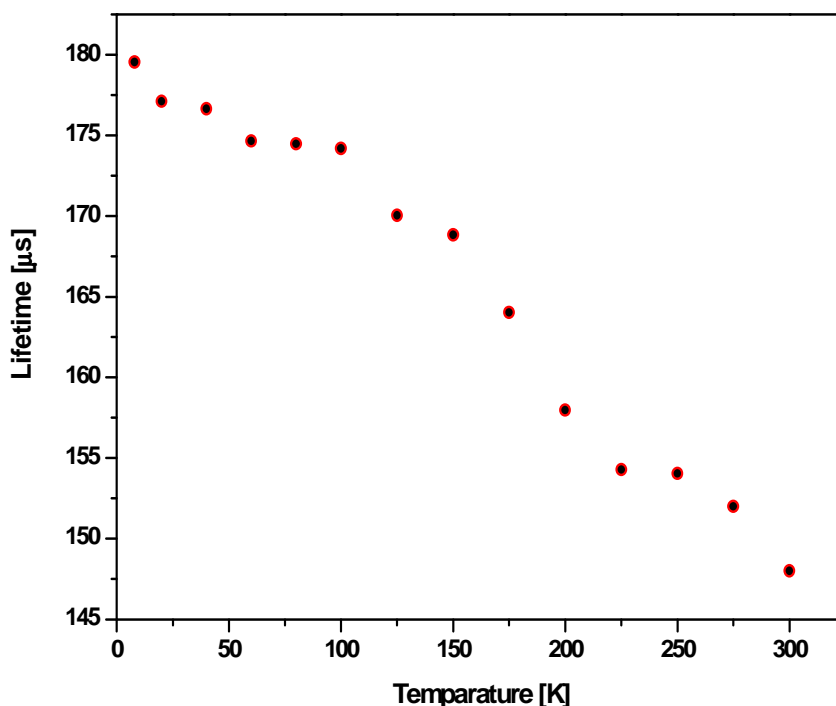


Fig. 5.7 Lifetimes of the $^1D_2 \rightarrow ^3H_4$ transition of Pr^{3+} (0.2 mol%) doped in SiO_2 plotted against the temperature in the 8-300 K regions.

5.4 Energy transfer from ZnO nanoparticles to Pr^{3+} ions in SiO_2 .

Figure 5.8 presents the PL emission spectra of $SiO_2:0.2 \text{ mol\% } Pr^{3+}$ and $ZnO.SiO_2:0.2 \text{ mol\% } Pr^{3+}$ phosphors under excitation at 90 nm using synchrotron radiation. It was observed that upon VUV excitation on the $4f5d$ state of Pr^{3+} , only characteristic emissions from Pr^{3+} ion with the main red emission centred at 605 nm could be detected from both $SiO_2:Pr^{3+}$ and $ZnO.SiO_2:Pr^{3+}$ phosphors. The green emission from ZnO nanoparticles was suppressed in $ZnO.SiO_2:Pr^{3+}$ and the intensity

of the Pr^{3+} emission was approximately twice the intensity of the $\text{SiO}_2:\text{Pr}^{3+}$ despite lower Pr^{3+} concentration. The quenching of green emission from ZnO as a result of enhanced Pr^{3+} emission demonstrates sensitization of Pr^{3+} emission centres by ZnO nanoparticles.

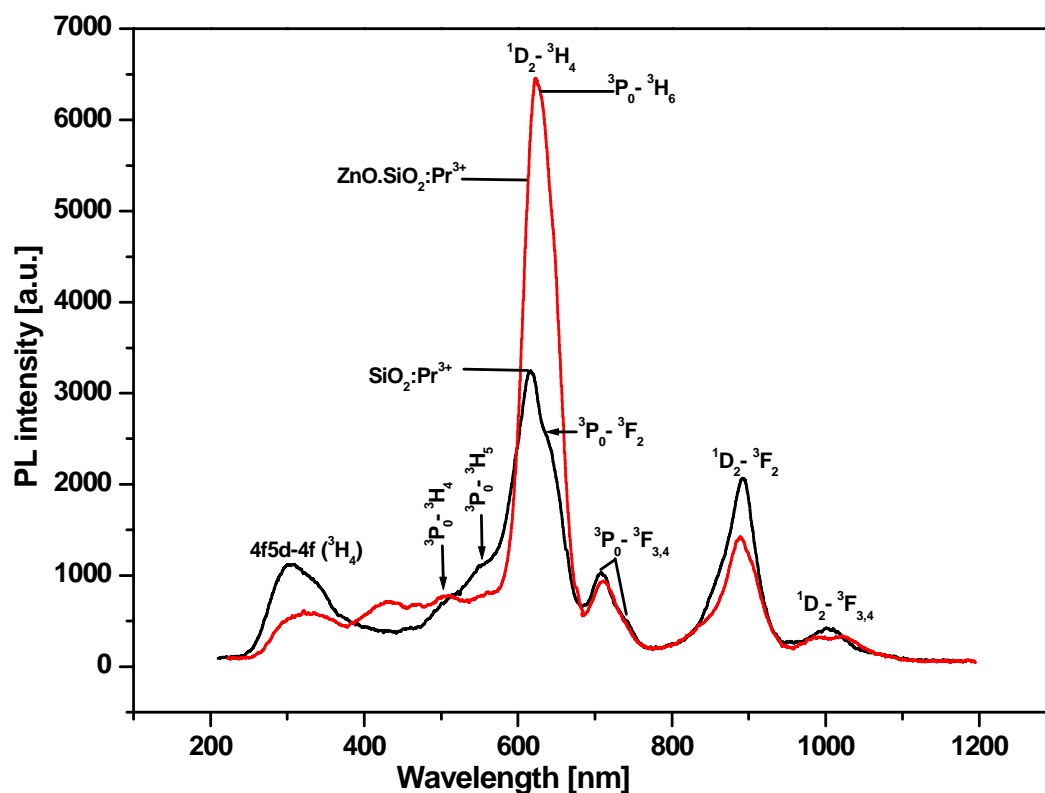


Fig. 5.8 PL emission spectra of $\text{SiO}_2:\text{Pr}^{3+}$ and $\text{ZnO}:\text{SiO}_2:\text{Pr}^{3+}$ after VUV excitation at 90 nm using synchrotron radiation.

The PL excitation spectra of $\text{ZnO}:\text{SiO}_2:\text{Pr}^{3+}$ presented in figure 5.9 showed much stronger bands compared to pure $\text{SiO}_2:\text{Pr}^{3+}$, confirming the energy transfer effect of ZnO on the excitation of the 4f electrons in Pr^{3+} ions.

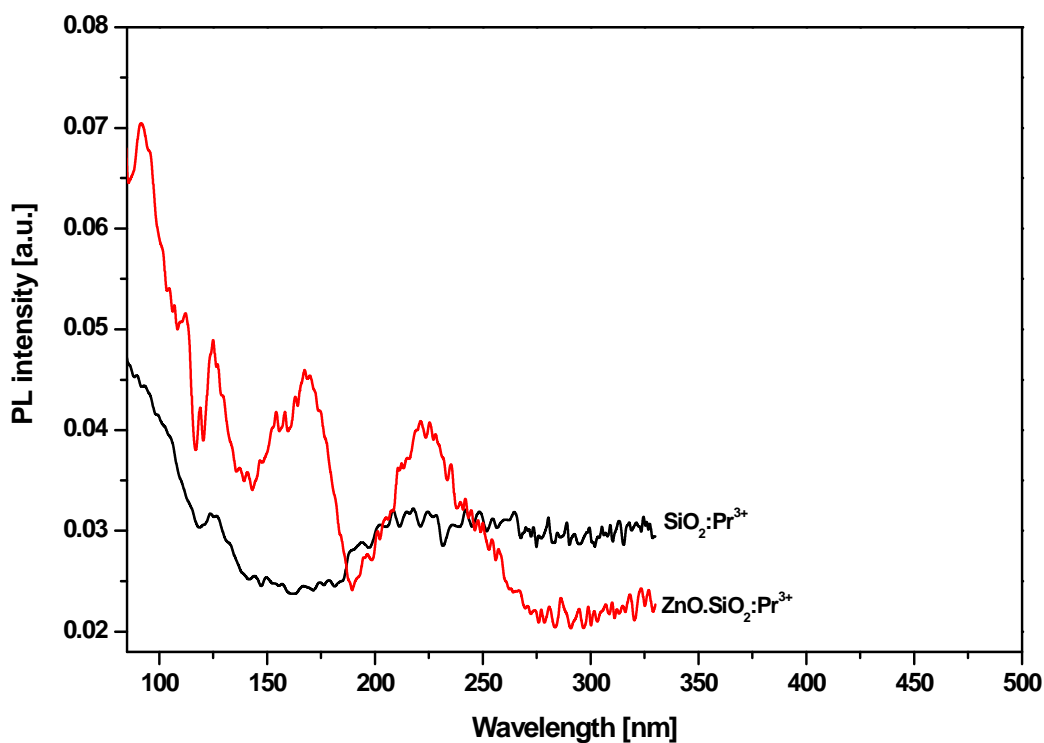


Fig. 5.9 PL excitation spectra of $\text{SiO}_2:\text{Pr}^{3+}:0.2 \text{ mol\%}$ with and without ZnO nanophosphors monitoring the emission peak at 605 nm.

Luminescence decay curves of $\text{SiO}_2:0.2 \text{ mol\% Pr}^{3+}$, $\text{ZnO.SiO}_2:0.2 \text{ mol\% Pr}^{3+}$ and ZnO emissions were recorded at room temperature and are presented in figures 5.10 (a) and (b). It can be seen from figure 5.10 (a) that the $\text{Pr}^{3+} \ ^1\text{D}_2 \rightarrow \ ^3\text{H}_4$ emission from $\text{SiO}_2:\text{Pr}^{3+}$ decayed faster with the lifetime of 144 μs which is almost twice shorter than that of $\text{ZnO.SiO}_2:\text{Pr}^{3+}$ which had lifetime of 236 μs . For pure ZnO nanoparticles, the decay curve also followed the first order exponential profile and the lifetime was determined to be 2 μs as shown in figure 5.10 (b) which is even much shorter than that of $\text{SiO}_2:\text{Pr}^{3+}$ with and without ZnO.

These results compare well with the results observed by Hayakawa *et al.* [18] and Chen *et al.* [19]. In principle, the radiative recombination rate should be similar before and after ZnO incorporation in $\text{SiO}_2:\text{Pr}^{3+}$. Moreover, when the non-radiative decay time remains the same, the decay time should be shorter indicating that the

energy transfer exists due to additional non-radiative pathways [18,20]. In the present results, the longer lifetime observed from ZnO.SiO₂:Pr³⁺ may be explained by formation of defects at the surface or boundaries of ZnO nanocrystals which can serve as energy trap centres thus supporting the energy transfer in the system. It cannot be ignored that for pure ZnO nanocrystals, electron-or hole- trapped surface levels exists due to widening of the bandgap (365 nm) with smaller particle sizes. Also, in ZnO some intrinsic defects such as oxygen vacancies exist. Such defects create some sites which can then trap free electrons and serve as non-radiative recombination centres. However, incorporation of ZnO into SiO₂:Pr³⁺ decreases the non-radiative decay rate significantly as photogenerated trapped electron or hole at the surface strongly interact with the Pr³⁺ ion located close to the boundary between ZnO and SiO₂. Hence the longer lifetime for SiO₂:Pr³⁺ with ZnO was observed irrespective of additional nonradiative decay pathways.

An energy level scheme of Pr³⁺ and ZnO presented in figure 5.11 shows the transitions involved in the energy transfer from ZnO to Pr³⁺ and the emission processes involved. When the ZnO.SiO₂:Pr³⁺ nanocomposite phosphor is exposed to VUV radiation, the excitation energy absorbed by ZnO promotes the electrons from the valence band to the conduction band resulting in the creation of an exciton and the subsequent non-radiative relaxation to the defect states.

Quenching of ZnO emission leading to enhanced red emission from Pr³⁺ indicates that the energy transfer process from ZnO to Pr³⁺ was faster than hole trapping and recombination with electrons in the valence band. This therefore means that part of the recombination energy was transferred to Pr³⁺ ions to promote their electrons from the ground states ($4f^2$) to the higher lying excited ones (3P_2 states) which then decay non-radiatively to the 3P_0 and 1D_2 followed by radiative relaxation

to the 3H_6 and 3H_4 with red line emission at 605 and 614 nm, respectively. The energy transfer from ZnO to Pr^{3+} is speculated to be through phonon mediated processes since the spectral overlap between the emission of the donor (ZnO) and the excitation of the acceptor (Pr^{3+}) that could result in energy transfer from ZnO to Pr^{3+} was not observed. Bang *et al.* [5] also proposed similar mechanism for Eu^{3+} doped SiO_2 with embedded ZnO nanoparticles.

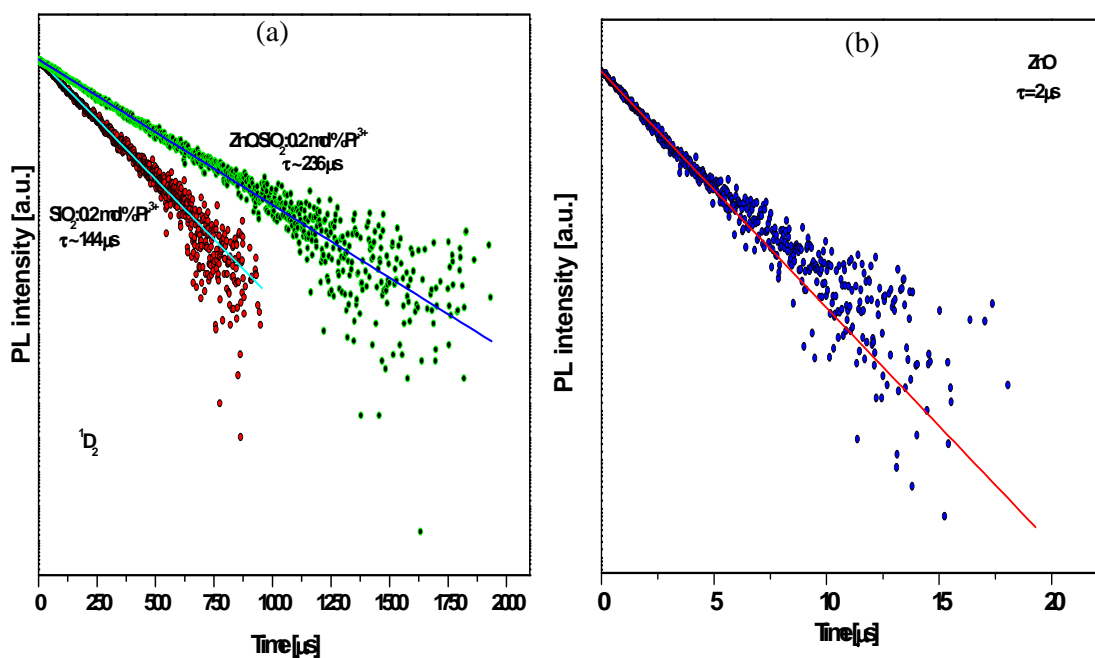


Fig. 5.10 Luminescence decay curves of (a) $SiO_2:Pr^{3+}$, $ZnO.SiO_2:Pr^{3+}$ nanophosphors and (b) ZnO nanocrystals.

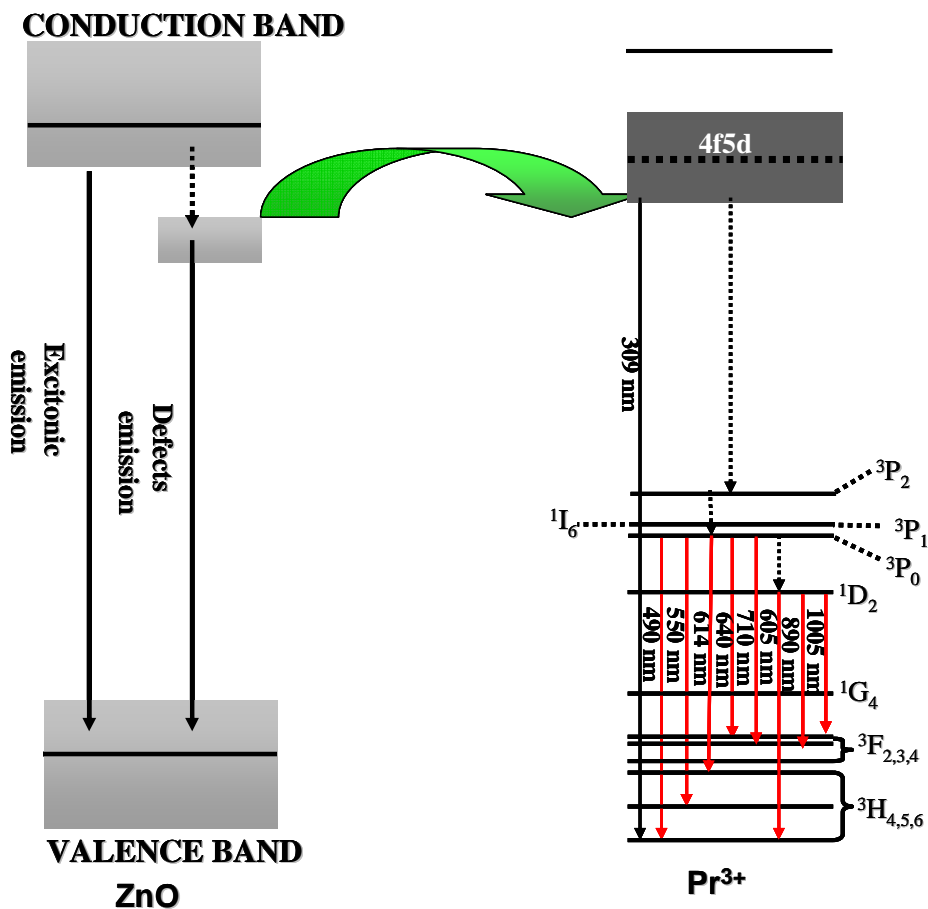


Fig. 5.11 Schematic energy level diagram showing the transition localized within Pr^{3+} ions and ZnO nanoparticles.

5.5 CONCLUSION

Red emission originating from both $^3\text{P}_0$ and $^1\text{D}_2$ emitting levels of Pr^{3+} was observed from both $\text{SiO}_2:\text{Pr}^{3+}$ with and without embedded ZnO nanoparticles. $^1\text{D}_2$ level showed the longer lifetime compared to the $^3\text{P}_0$ level as observed from luminescence decay data. Investigation of the luminescence of Pr^{3+} in SiO_2 as a function of Pr^{3+} concentration revealed the shortening of $^1\text{D}_2$ lifetime with increasing Pr^{3+} concentration i.e above 0.2 mol%. The concentration quenching effect due to migration of excitation energy among Pr^{3+} ions was speculated to be the main effect

of self-quenching of the 1D_2 level. The 1D_2 level was also found to be influenced by temperature as its lifetime slowly decreased with increasing temperature from 8 to 300 K. Enhanced red emission from Pr^{3+} doped SiO_2 was achieved by incorporating ZnO nanoparticles indicating that ZnO act as an effective sensitizer for Pr^{3+} emission. The luminescence enhancement from Pr^{3+} with quenching of green emission from ZnO was attributed to energy transfer from ZnO to Pr^{3+} .

5.6 REFERENCES

- [1] L. Del Longo, M. Ferrari, E. Zanghellini, M. Bettinelli, J. A. Capobianco, M. Montagna, F. Rossi, *J. Non-Cryst. Solids* 231 (1998) 178-188.
- [2] R. Balda, J. Fernandez, I. Saez de Ocariz, J.L. Adam, A. Mendioroz, E. Montoya, *Opt. Mater.* 13 (1999) 159-165.
- [3] Z. Mazurak, W.A. Pisarski, J. Gabrys-Pisarska, M. Zelechower *Phys. Status Solidi B* 237 [2] (2003) 581-591
- [4] M.A. Guwoski, G. Dominiak-Dzik, P. Solarz, R. Lisiecki, W. Ryba-Romanowski, *J. Alloys Compd.* 438 (2007) 72-76
- [5] J. Bang, H. Yang, P. H. Holloway *J. Chem. Phys.* 123 (2005) 084709.
- [6] A.P. Vink, E. van der Kolk, P. Dorenbos, C.W.E van Eijk *Alloys Compd.* 341 (2002) 338-341
- [7] W. Ryba-Romanowski, G. Dominiak-Dzik, P. Solarz, B. Klimesz, M. Zelechower, *J. Non-Cryst. Solids* 348&346 (2004) 391-395
- [8] E. van der Kolk, P. Dorenbos, A.P. Vink, R.C. Perego, C.W.E. van Eijk, *Phys. Rev. B* 64, 195129
- [9] Y. Fu, G. Zhang, Z. Qi, W. Wu, C. Shi, *J. Lumin.* 124 (2007) 370-374
- [10] K.V. Ivanovskikh, A. Meijerink, F. Piccinelli, A. Speghini, E.I.; Zinin, C. Ronda, M. Bettinelli, *J. Lumin.* 130 (2010) 893-901
- [11] L. Bo, S. Chao-Shu, Q. Ze-Ming, T. Ye, *Chin. Phys. Lett.* 22 (2005) 2677-2679
- [12] F. You, S. Huang, C. Meng, D. Wang, J. Xu, Y. Huang, G. Zhang, *J. Lumin.* 122 (2007) 58-61
- [13] K. Annapurna, R. Chakrabarti, S. Buddhudu, *J. Mater. Sci.* 42 (2007) 6755-6761
- [14] V.K. Rai, K. Kumar, S.B. Rai *Opt. Mater.* 29 (2007) 873-878.
- [15] A. Biswas, S. Chakrabarti, H.N. Acharya, *Mater. Sci. Eng. B* 49 (1997) 191.

- [16] Huang, Y.; Tsuboi, T.; Seo, H.J., *J. Phys. Chem. A* 112 (2008) 5839-5845
- [17] Solarz, P; Gajek, Z., *J. Phys. Chem. C* 114 (2010) 10937-10946
- [18] Hayakawa, T.; Selvan S. T.; Nogami, M., *J. Sol-Gel Sci. Tech.* 19 (2000) 779-783
- [19] R. Chen, Y. Q. Shen, F. Xiao, B. Liu, G. G. Gurzadyan, Z .L. Dong, X. W. Sun, X. W. Sun, *J. Phys. Chem. C* 114 (2010) 18081-18084
- [20] P. Vergeer, V. Babin, A. Meijerink, *J. Lumin.* 114 (2005) 267-274

EFFECTS OF Ce³⁺ CONCENTRATION, BEAM VOLTAGE AND CURRENT ON THE CL INTENSITY OF SiO₂:Pr³⁺-Ce³⁺ NANOPHOSPHOR

6.1 INTRODUCTION

Field Emissive Display (FED) technology is an excellent model for the next generation of display market due to its anticipated high brightness, high contrast ratio, light weight, and low-power consumption [1-3]. Phosphors with high luminous efficiency and thermal stability are regarded as the best candidates for application in FED technology. Recently, red emitting CaTiO₂, BaTi₄O₉ and SrTiO₃ activated with Pr³⁺ phosphors were investigated for application in FEDs [2,4,5]. The increase of brightness with an increase in beam voltage (i.e. 1 to 5 kV) and current (i.e. 11 to 45 μ A) is attributed to deeper penetration of electrons into the phosphor surface and the larger electron beam current density. Such increase in the CL intensity at such low voltages is a good indication that such phosphor may be used in FEDs. This chapter focuses on the effects of Ce³⁺ concentration, beam voltage and current on the CL intensity of SiO₂:Pr³⁺-Ce³⁺ nanophosphor.

6.2 EXPERIMENTAL

SiO₂ co-doped with different concentrations of Pr³⁺-Ce³⁺ ion pairs samples were prepared by mixing 0.05 mol of TEOS, 0.1 mol of H₂O, 0.1 mol of ethanol, and 0.145 mol of dilute nitric acid.

The mixture was stirred at room temperature for 1 hour to get a clear solution. Desired concentration of Pr(NO)₃.6H₂O dissolved in 5 ml of ethanol was added and

the solution was stirred for 30 minutes. Finally, the desired amount of $\text{Ce}(\text{NO})_3 \cdot 6\text{H}_2\text{O}$ dissolved in 5 ml of ethanol was also added to the solution and stirred for another 30 minutes until a gel formed. The gel was then transferred to a petri dish for drying at room temperature for eight days and then annealed in air at $600\text{ }^\circ\text{C}$ for 2 hrs.

The particle morphology and size were analysed using a JEOL JSM-7500F, Field Emission SEM and JEOL 2100, High Resolution Transmission Electron Microscopy (HRTEM). The chemical composition of the samples was analyzed using Energy Dispersive Spectrometer (EDS). The optical absorption properties of the samples were studied by a Spotlight 400 FTIR imaging system using the diffuse reflectance mode. The CL measurements were conducted using an Ocean Optics S2000 spectrometer attached to an ultra high vacuum chamber Physical Electronics PHI 549 Auger spectrometer. The first CL data were collected from the set of samples with different concentration (0.2, 1, 1.5, and 2 mol %) of Ce^{3+} while the Pr^{3+} was fixed at 0.2 mol %. Further measurements were conducted from $\text{SiO}_2:\text{Pr}^{3+}$ (0.2 mol %)- Ce^{3+} (1 mol %) whose CL intensity was comparatively the highest. The second set of CL data were recorded when the accelerating voltage was varied from 1 to 5 kV while keeping the beam current constant at $8.5\text{ }\mu\text{A}$. The last sets of data were collected when the beam current was varied from 5 to $30\text{ }\mu\text{A}$ while the beam voltage was kept constant at 2 kV.

6.3 RESULT AND DISCUSSION

EDS and HRTEM data confirmed the presence of rare earth clusters inside the silica matrix. As shown in figure 6.1(a), the HRTEM image revealed a high amorphous structure of SiO₂. This compares well with the XRD results which showed one broad diffraction peak at 22° corresponding to amorphous SiO₂ (see fig. 4.2). Figures 6.1 (a), (b) and (c) present the HRTEM images of SiO₂ nanoparticles, SiO₂:Pr³⁺, and SiO₂:Pr³⁺-Ce³⁺, respectively. From figures 6.1 (b) and (c), it can be seen that black spots are uniformly dispersed in amorphous silica matrix. These were not observed in pure silica matrix as shown in figure 6.1(a). The chemical analyzes of the samples confirmed the presence of Si, O, Ce, and Pr as indicated in the EDS figures 6.1 (d) and (e). Therefore based on these observations it was then concluded that the black spots represent clusters of rare earth ions with the size ranging from ~2 to 5 nm in diameter inside the SiO₂ matrix. These observations compare well with the results of Prakash *et al.* [6] and Fasoli *et al.* [7] where they observed clusters of Co doped NiAl₂O₄ in SiO₂, and Ce³⁺ in SiO₂, respectively.

Figure 6.2 shows FTIR spectra of SiO₂, SiO₂:Pr³⁺, SiO₂:Ce³⁺ and SiO₂:Pr³⁺-Ce³⁺ all calcined at 600 °C for 2hrs. The two absorption bands at 1160 and 1056 cm⁻¹ corresponding to the LO and TO modes of Si-O-Si asymmetric stretching vibration (ν_{as}), respectively [8,9] were observed for all the samples. The weak absorption band at 945 cm⁻¹ associated with Si-OH stretching mode was also present [8,9]. The presence of this absorption band can be due to the very strong Si-O-Si asymmetric stretching, ν_{as} (Si-O) absorptions in this region [8]. In addition, it was also realized that this band increased with incorporation of the activator ions into the SiO₂ matrix. Another absorption band associated with Si-O-Si symmetric stretching (ν_s) at 795 cm⁻¹ was observed [8,9].

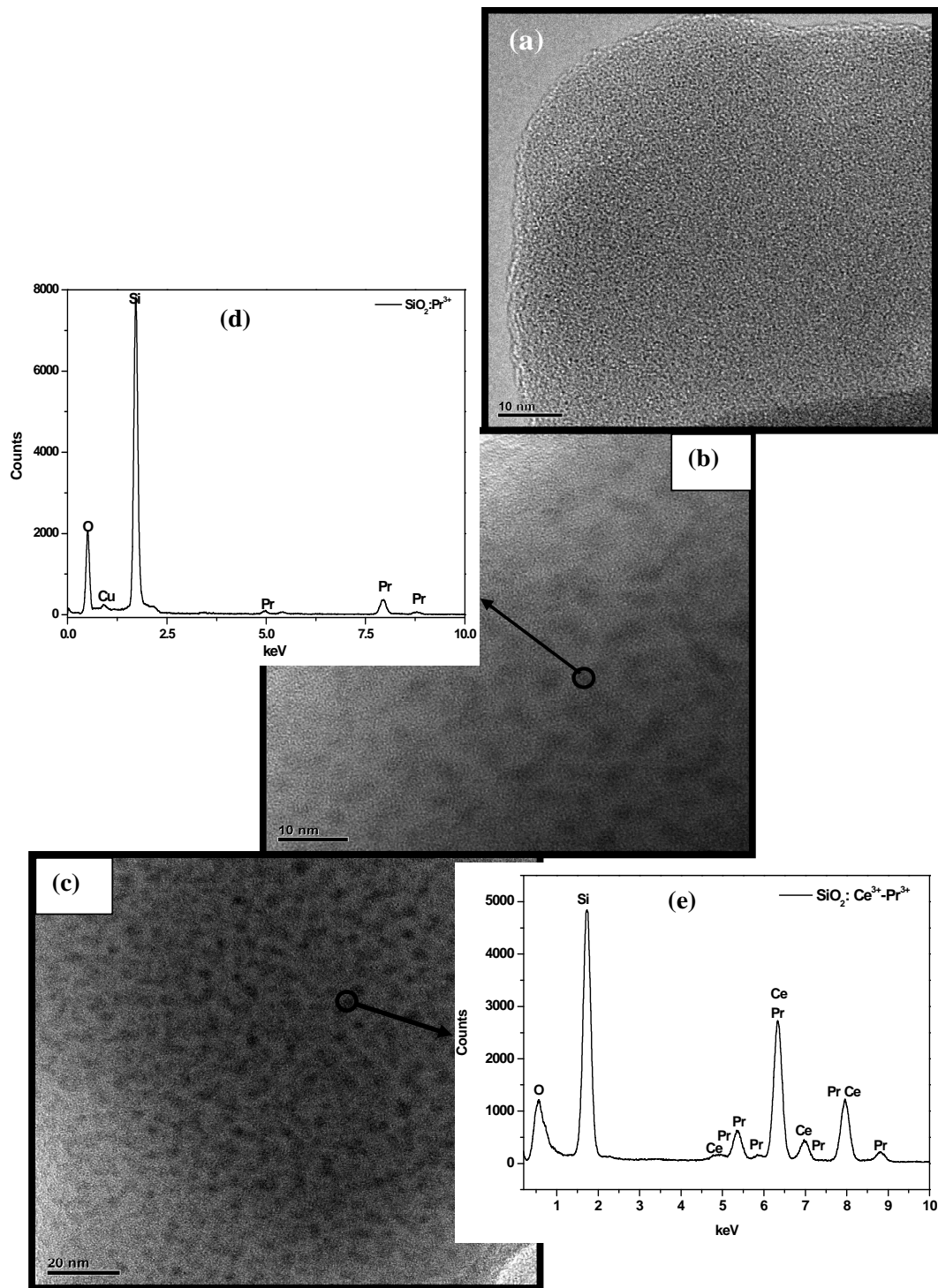


Fig. 6.1 HRTEM images of (a) SiO₂ nanoparticles, SiO₂:Pr³⁺, and (b) SiO₂:Pr³⁺-Ce³⁺ and EDS spectra of (d) SiO₂:Pr³⁺, and (e) SiO₂:Pr³⁺-Ce³⁺.

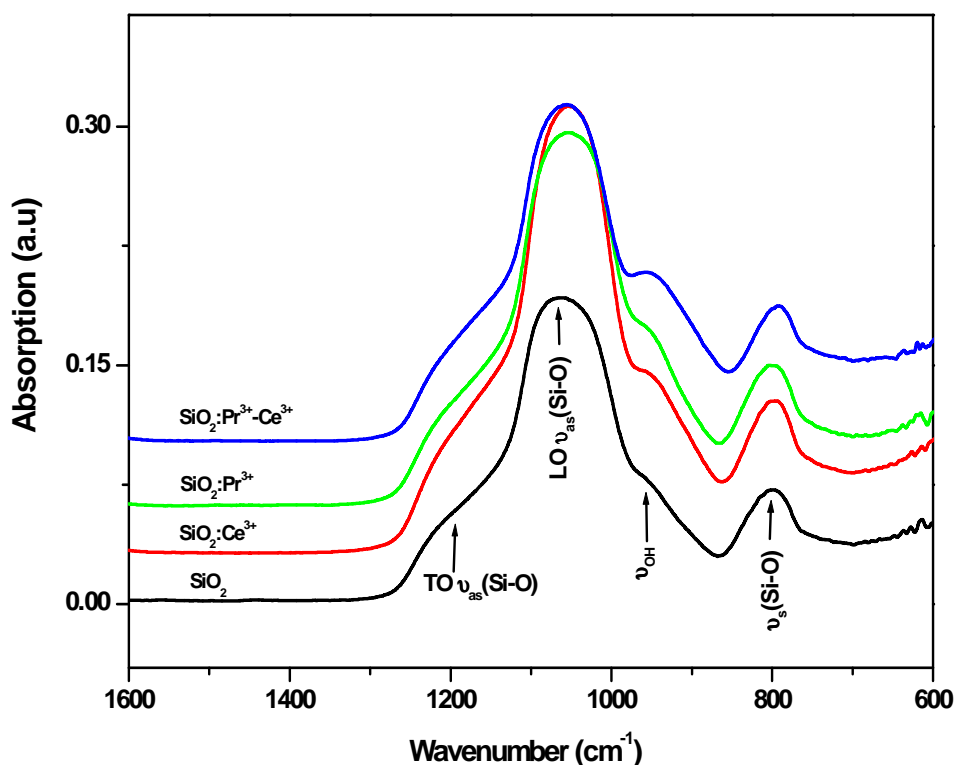


Fig. 6.2 FTIR absorption spectra of SiO_2 , $\text{SiO}_2:\text{Pr}^{3+}$, $\text{SiO}_2:\text{Ce}^{3+}$, $\text{SiO}_2:\text{Pr}^{3+}-\text{Ce}^{3+}$ phosphor powders.

The CL emission spectrum of SiO_2 shown on figure 6.3 presents the broad emission band centred in the blue region at 445 nm which can be ascribed to either structural defects in the SiO_2 network or charge transfer between O and Si atoms [10].

The CL emission spectrum of the $\text{SiO}_2:\text{Ce}^{3+}$ phosphor powders under irradiation of 2 kV electrons, 8.5 μA beam current in a high vacuum chamber at a base pressure of 1.2×10^{-8} Torr is shown in figure 6.4. The CL emission spectrum from $\text{SiO}_2:\text{Ce}^{3+}$ consists of two blue bands located at 452 nm (weak) and 494 nm (strong). The peak positions were determined from Gaussian fits as clearly shown in the figure. The two bands at 452 nm and 494 nm can be associated with ${}^2\text{D}_{3/2} \rightarrow {}^2\text{F}_{7/2}$ and ${}^2\text{D}_{3/2} \rightarrow {}^2\text{F}_{5/2}$ of Ce^{3+} , respectively.

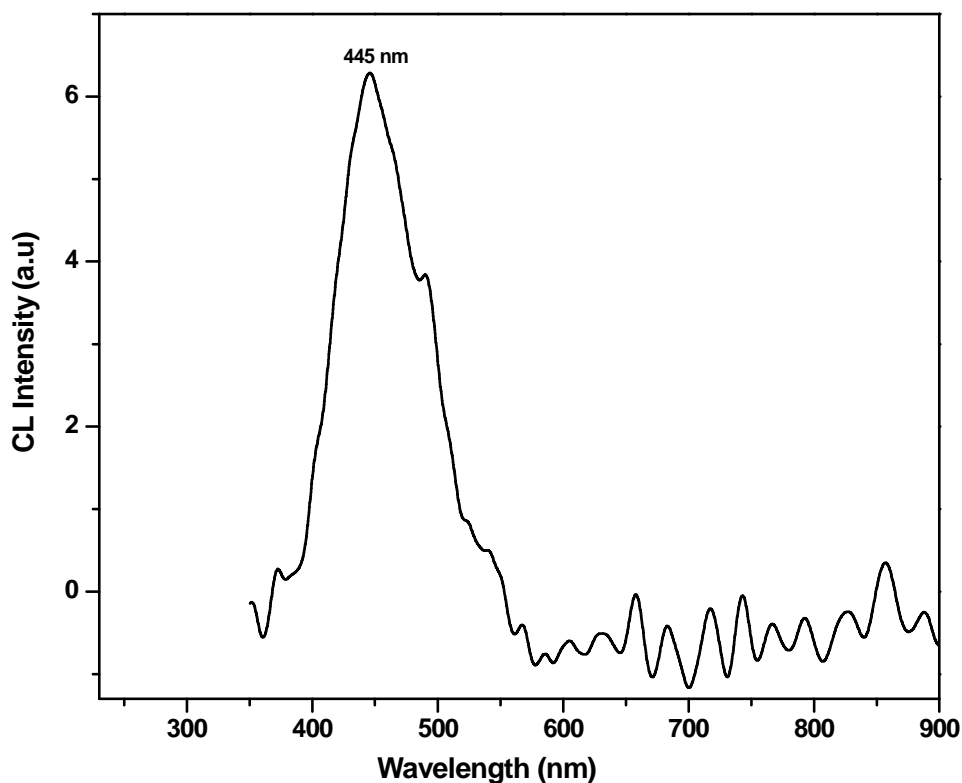


Fig. 6.3 CL emission spectra of SiO₂ nanoparticles irradiated with 2 kV, 8.5 μA beam of electrons in a high vacuum chamber containing 1.2×10^{-8} Torr.

Trivalent Ce ion has only one electron in the 4f state. The 4f electron of the $4f^1$ ground state configuration yields two components, $^2F_{5/2}$ and $^2F_{7/2}$ due to spin-orbit interaction and 5d electron of the excited $4f^0 5d^1$ configuration forms a 2D term which is then split by crystal field into two Stark components, $^2D_{3/2}$ and $^2D_{5/2}$ states [10, 11].

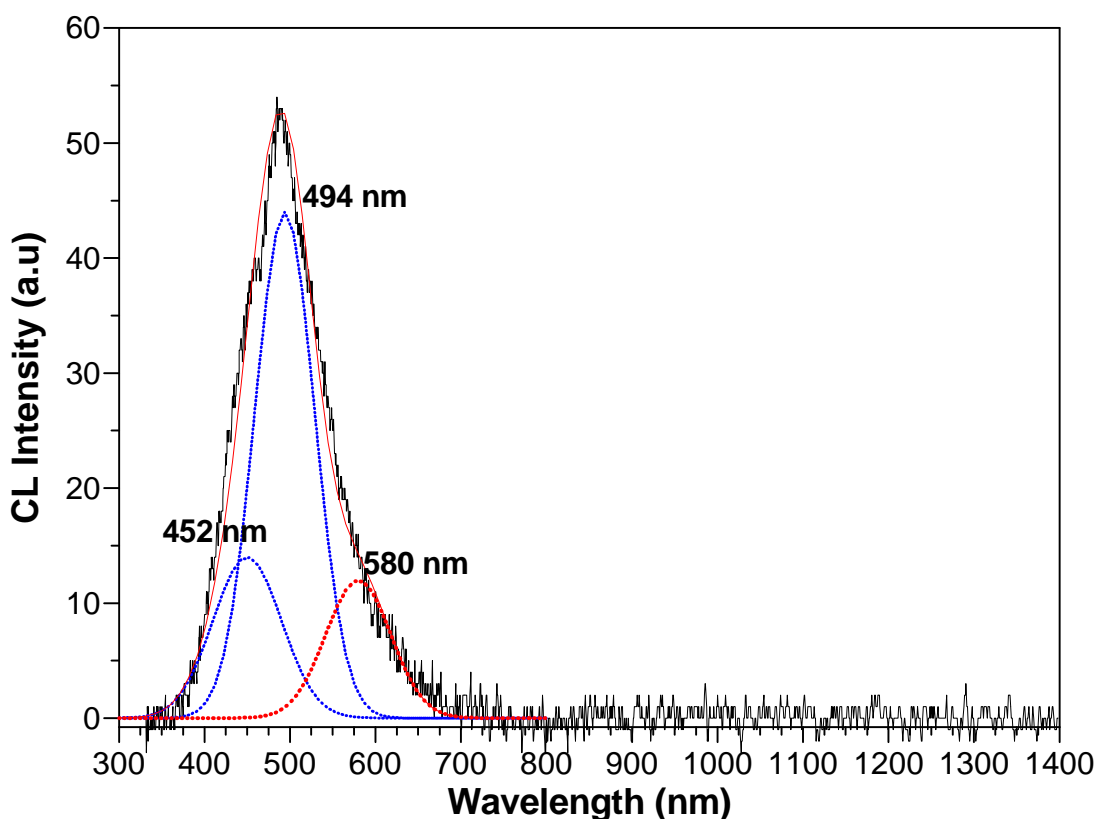


Fig. 6.4 CL emission spectrum of $\text{SiO}_2:\text{Ce}^{3+}$ after irradiation with 2 kV, 8.5 μA beam of electrons in a high vacuum chamber containing a base pressure of 1.2×10^{-8} Torr.

The CL emission spectra of the $\text{SiO}_2:\text{Pr}^{3+}$, $\text{SiO}_2:\text{Ce}^{3+}$, and $\text{SiO}_2:\text{Pr}^{3+} \cdot \text{Ce}^{3+}$ phosphor powders under irradiation with 2 kV electrons, 8.5 μA beam current in a high vacuum chamber at a base pressure of 1.2×10^{-8} Torr are shown in figure 6.5. The CL emission spectrum from $\text{SiO}_2:\text{Pr}^{3+}$ showed the characteristic emission peaks of Pr^{3+} that can be associated with the transitions originating from the $^3\text{P}_0$ and $^1\text{D}_2$ multiplets to the $^3\text{H}_{(J=6,5,4)}$ and $^3\text{F}_{(J=2,3,4)}$ energy levels all localized in the $4f_2$ intra-configuration of the Pr^{3+} ions. The broad red emission at 580-700 nm which could be due to both $^3\text{P}_0 \rightarrow ^3\text{H}_6$ and $^1\text{D}_2 \rightarrow ^3\text{H}_4$ transitions with dominant emission from $^3\text{P}_0$ level of Pr^{3+} was also observed.

The CL emission spectra of $\text{SiO}_2:\text{Ce}^{3+}\text{-Pr}^{3+}$ showed both bands from Ce^{3+} in the blue spectral region and a small shoulder from Pr^{3+} in the red spectral region when the

amount of Pr^{3+} and Ce^{3+} were both 0.2 mol%. The small shoulder from Pr^{3+} was slowly quenched with increasing Ce^{3+} concentration and only blue emission from Ce^{3+} could be observed. Blue emission from Ce^{3+} was slightly enhanced with addition of 1 mol% Ce^{3+} into 0.2 mol% Pr^{3+} compared to singly doped $\text{SiO}_2:\text{Ce}^{3+}$. These results suggest the energy transfer from Pr^{3+} ions to its nearest neighbouring Ce^{3+} ions. The energy transfer from Pr^{3+} to Ce^{3+} may be explained by the non-radiative relaxation from excited $4f^15d$ state to higher 3P level of Pr^{3+} ion to $5d$ state of Ce^{3+} ion, followed by the radiative relaxation of excited $5d$ electrons of Ce^{3+} ion.

The energy level diagram presented in figure 6.6 shows the energy transfer pathways between Pr^{3+} and Ce^{3+} ions. The main radiative transitions of Pr^{3+} and Ce^{3+} are designated with downward arrows. It is also important to mention that there is a competition between Pr^{3+} radiative process and energy transfer between Pr^{3+} and Ce^{3+} , however, the energy transfer from Pr^{3+} to Ce^{3+} takes place faster. In addition, for the process of energy transfer to dominate, the Ce^{3+} and Pr^{3+} neighbouring ions must be near enough in the host matrix. The quenching of luminescence with increasing Ce^{3+} ions may be due to formation of clusters of Ce^{3+} ions with Pr^{3+} in the host matrix. This could be due to self-quenching of Ce^{3+} neighbouring ions. At 1 mol% Ce^{3+} , the Ce^{3+} neighbouring ions may be near enough to transfer the energy from one to another. However, an increase in Ce^{3+} concentration led to the shortening of the distance between its neighbouring ions as a result of non-radiative loss of excitation energy between Ce^{3+} ions favouring quenching effect and decreasing luminescence intensity.

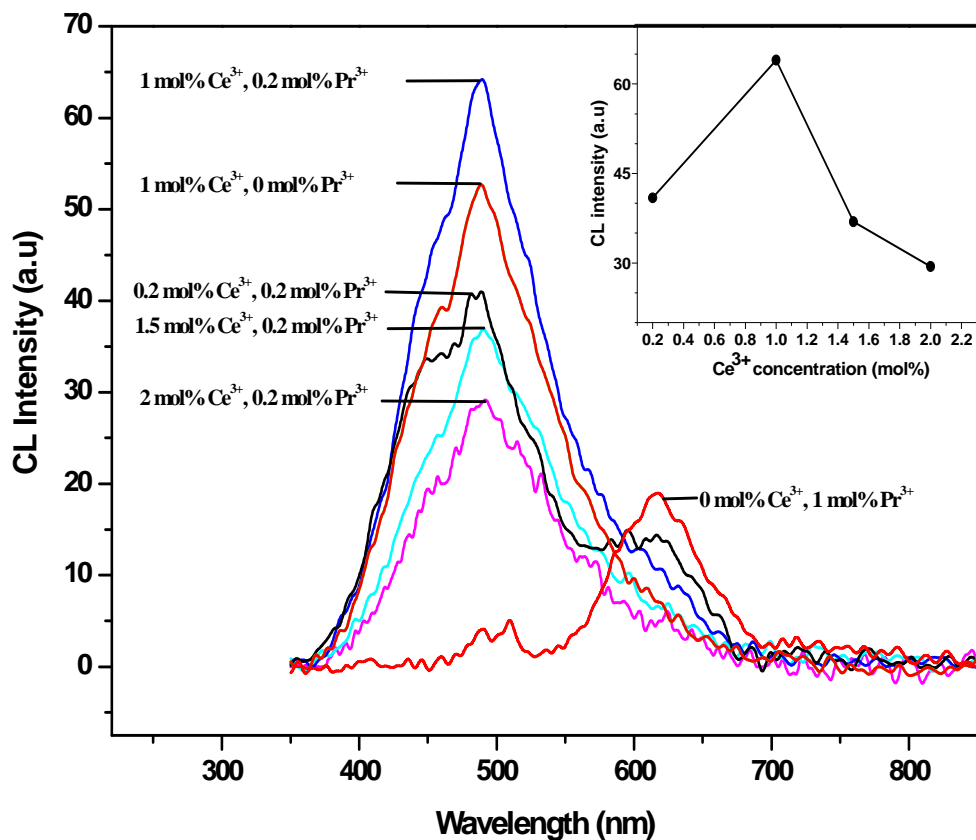


Fig. 6.5 CL emission spectra of the SiO₂:Pr³⁺ (1 mol %), SiO₂:Ce³⁺ (1 mol %) and SiO₂:Pr³⁺ (0.2 mol %) - Ce³⁺ (0.2, 1, 1.5, 2 mol %) irradiated with 2 kV, 8.5 μA beam of electrons in a high vacuum chamber containing a base pressure of 1.2 x 10⁻⁸ Torr. The insert shows the CL intensity as a function of different Ce³⁺ concentrations.

Jang *et al.* [11] observed the energy transfer between Pr³⁺ and Ce³⁺, as well as between Pr³⁺ and Tb³⁺ co-doped in Y₃Al₅O₁₂ (YAG). Nie *et al.* [12], on the other hand, reported the energy transfer between Pr³⁺ and Cr³⁺ in SrAl₁₂O₁₉.

Vergeer *et al.* [13] and Meijerink *et al.* [14] found it difficult to find the efficient energy transfer from Pr³⁺ to Eu³⁺ irrespective of the fulfilment of an important condition for energy transfer which is the presence of resonance between Pr³⁺ and Eu³⁺ ions. The luminescence intensities were compared for different gels with and without Mg particles by varying the different concentrations of Mg [15]. Silica containing Mg²⁺ and Ce³⁺ ions had broad blue emission due to the energy

transfer from Mg^{2+} to Ce^{3+} . An increase in luminescence intensity was observed as the Mg^{2+} to Ce^{3+} ratio increases for the range investigated.

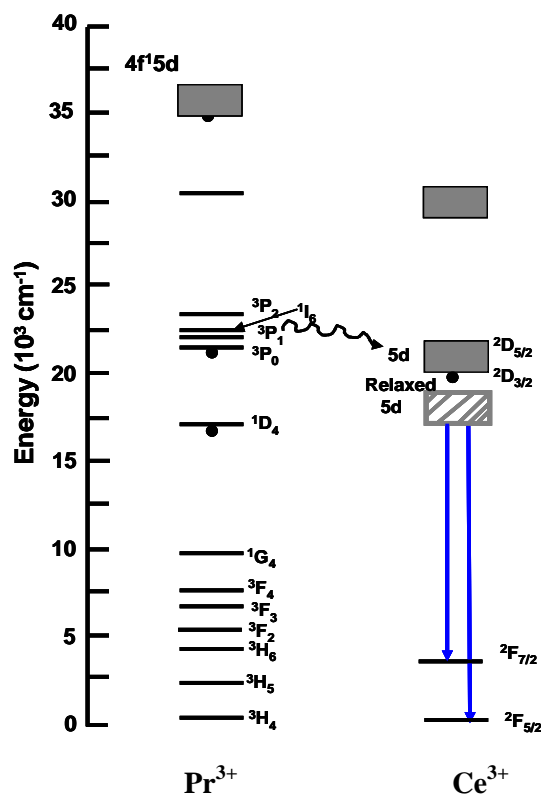


Fig. 6.6 Schematic energy level diagram showing the transition localized within Pr^{3+} and Ce^{3+} ions.

The dependence of the CL intensity of $\text{SiO}_2:\text{Pr}^{3+}\text{-Ce}^{3+}$ on different beam voltages from 1 to 5 kV while the beam current was fixed at $8.5 \mu\text{A}$ was investigated as shown in figure 6.7. When the beam current was fixed at $8.5 \mu\text{A}$, the CL intensity of this phosphor increased upon increasing beam voltage from 1 to 5 kV. This indicates that saturation could not be reached up to 5 kV which is a good prospect for FEDs. Similarly, the CL intensity was observed to increase with an increase in the beam current from 5 to $30 \mu\text{A}$ while the beam voltage was kept constant at 2 kV.

Figure 6.8 shows the beam current plotted against the maximum CL intensity of $\text{SiO}_2:\text{Pr}^{3+}\text{-Ce}^{3+}$ at 488 nm. Again, no saturation was observed up to $30 \mu\text{A}$.

The increase of CL intensity with an increase in beam voltage and beam current can be attributed to deeper penetration of electrons into the phosphor surface and the larger electron beam current density [16]. The electron penetration depth can be estimated using equation 2.2. Figure 6.9 shows the normalized calculated penetration depth plotted against the electron beam voltage.

It can be clearly observed from this figure that the penetration of the energetic electrons into the phosphor was shown to increase with increasing beam voltage. The deeper penetration of electrons into the phosphor results in an increase on the electron-solid interaction volume in which excitation of Ce^{3+} and Pr^{3+} activator ions takes place [17]. Therefore, an increase in interaction volume, which effectively determines the generation of light emission with an increase in electron energy, resulted in an increase in the CL intensity of $SiO_2:Pr^{3+}-Ce^{3+}$.

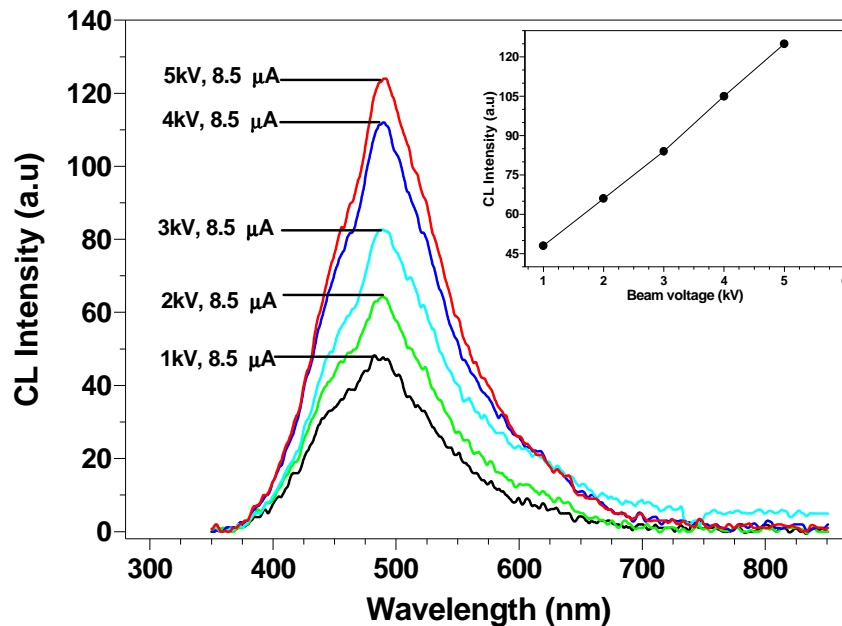


Fig. 6.7 CL emission intensities of Ce^{3+} in $SiO_2: Pr^{3+}-Ce^{3+}$ phosphor as a function of different beam voltages.

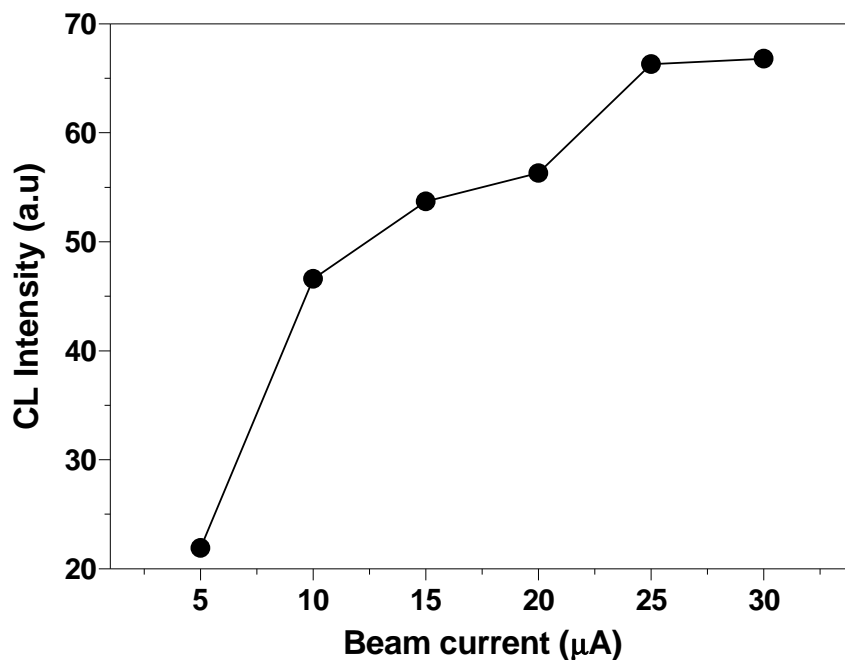


Fig. 6.8 CL emission intensities of Ce^{3+} in $\text{SiO}_2: \text{Pr}^{3+}\text{-Ce}^{3+}$ phosphor as a function of different beam currents.

Furthermore, with an increase of accelerating voltage, more plasmons are being produced by incident electrons resulting in a large number of excited Ce^{3+} and Pr^{3+} ions, thus yielding higher CL intensity [16]. The size of the nanoparticles may, however, play a significant role in the CL intensity at different excitation beam voltages due to the electron excitation volume involved [18], especially when the penetration depth equals the particle size. It is assumed that the CL emission from the boundaries/surface of the nanoparticles is less than that of the inside of the particle due to surface states that may lead to non-radiative decay of the excited electrons.

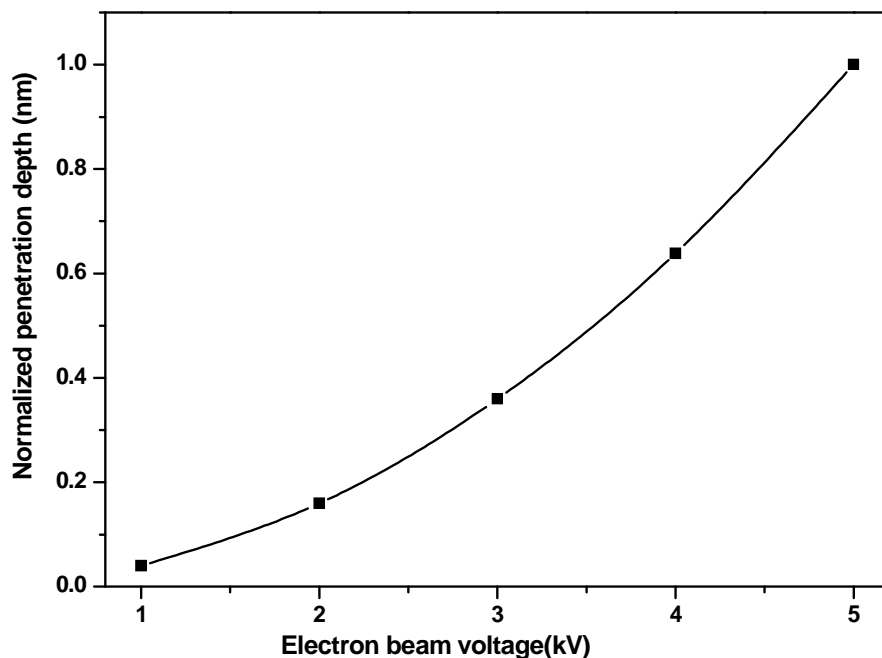


Fig. 6.9 The calculated penetration depth as a function of electron beam voltage.

The CL spectra before and after 50 C/cm^2 electron bombardment are shown in figure 6.10. The CL intensity of the main broad peak at 488 nm with a small shoulder at 450 nm decreased by 80% under 2 kV, $8.5 \mu\text{A}$ electron beam exposure.

Figure 6.11 shows the Auger peak-to-peak heights (APPHs) of O, Si and C elements on the surface of the $\text{SiO}_2:\text{Pr}^{3+}-\text{Ce}^{3+}$ phosphor as a function of electron dose. The CL intensity is plotted on the same figure for comparison. The Auger peak intensity of O was shown to decrease with prolonged electron bombardment of the SiO_2 while that of Si was rather constant. It was also noticed that prolonged electron bombardment led to a significant decrease in the CL intensity and this corresponds to the decrease in the Auger peak intensity of O. This correlation between the decrease of CL intensity and that of the Auger peak intensity from O can be attributed to desorption of O from the surface following the electron-beam dissociation of SiO_2 as a result of the formation of an oxygen-deficient surface dead or non luminescent layer

of SiO_x , where $x < 2$ on the surface [19, 20]. The colour also changed more to the red region, indicated that the Pr^{3+} is still contributing to the light emission.

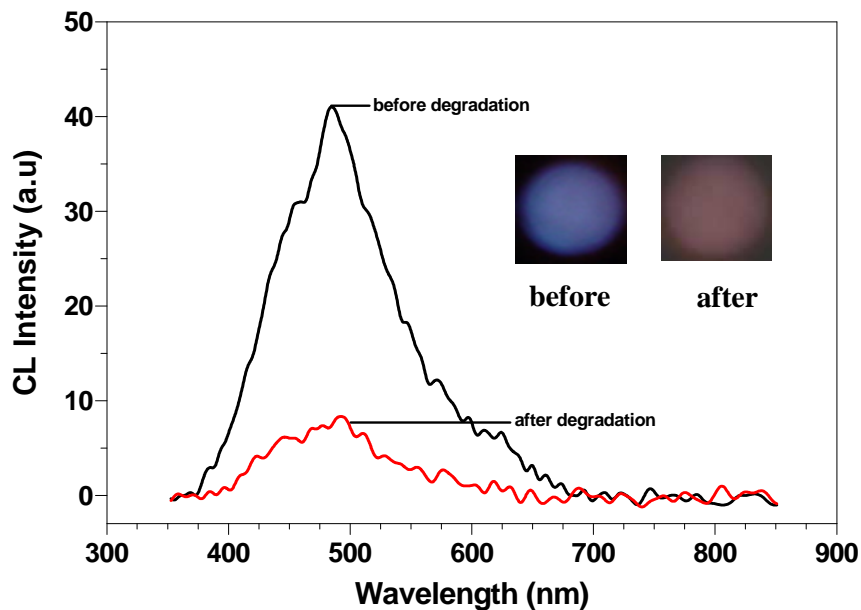


Fig. 6.10 CL emission spectra of $\text{SiO}_2:\text{Pr}^{3+},\text{Ce}^{3+}$ powder phosphors before and after exposure to 2 kV, 8.5 μA electrons in 1×10^{-7} Torr of O_2 backfilled from the base pressure of 1.2×10^{-8} Torr.

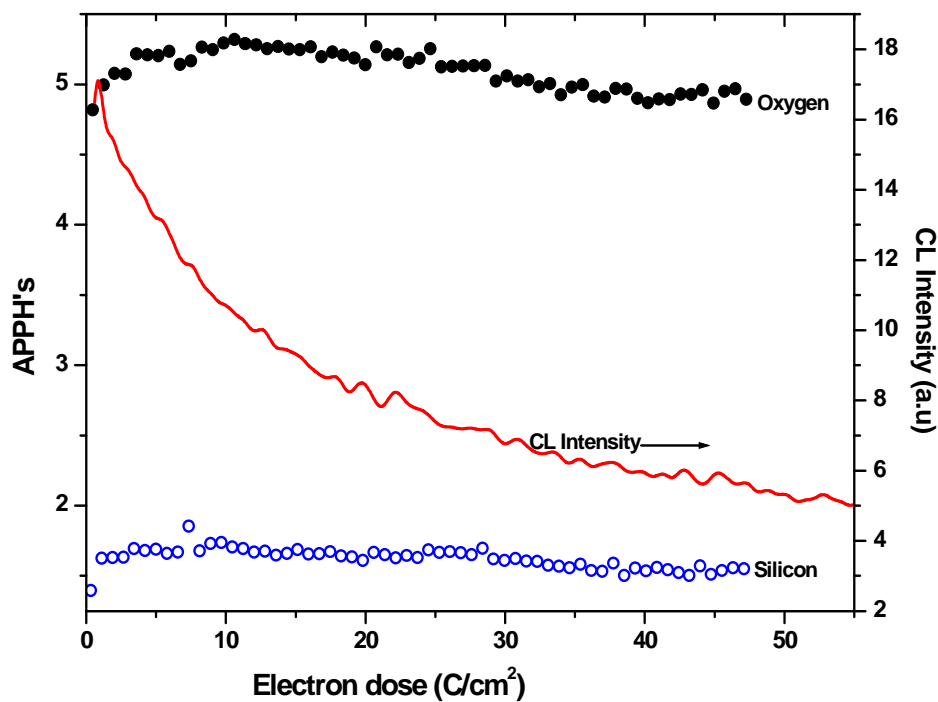


Fig. 6.11 Auger peak-to-peak heights of O and Si versus 2 kV electron dose at 1×10^{-7} Torr O_2 backfilled from the base pressure of 1.2×10^{-8} Torr.

6.4 CONCLUSION

The CL intensity behavior of the $\text{SiO}_2: \text{Pr}^{3+} - \text{Ce}^{3+}$ nanophosphor at different concentrations of Ce^{3+} co-doped in $\text{SiO}_2: \text{Pr}^{3+}$, beam voltages and beam currents was presented. The CL emission from Ce^{3+} (blue) and Pr^{3+} (red) ions was observed when the concentration of these ions 0.2 mol %, with the blue emission from Ce^{3+} dominating. However, for addition of 1 mol % Ce^{3+} to 0.2 mol % Pr^{3+} led to quenching of Pr^{3+} emission and enhanced blue emission from Ce^{3+} was observed as compared to $\text{SiO}_2: \text{Ce}^{3+}$. Energy transfer from Pr^{3+} to Ce^{3+} was discussed. An increase in the CL intensity was observed with increasing beam voltage up to 5 kV and beam current up to 30 μA and no saturation was observed.

6.5 REFERENCES

- [1] X. Liu, J. Lin, *Solid State Sci.* 11 (2009) 2030-2036
- [2] S. Tan, P. Yang, C. Li, W. Wang, J. Wang, M. Zhang, X. Jing, J. Lin, *Solid State Sci.* 12 (2010) 624-629
- [3] H.C. Swart, L. Oosthuizen, P.H. Holloway, G.L.P. Berning. *Surf. Interface Anal.* 26 (1998) 337-342
- [4] L. Tian, S-I. Mho, Z. Jin, *J. Lumin.* 129 (2009) 797-800
- [5] Q. Pang, J. Shi, and M. Gong, *J. Am. Ceram. Soc.* 90 [12] (2007) 3943-3946
- [6] I. Prakash, P. Muralidharan, N. Nallamuthu, and N. Satyanarayana, *J. Am. Ceram. Soc.* 89 [7] (2006) 2220-2225
- [7] M. Fasoli, A. Vedda, A. Lauria, F. Moretti, E. Rizzelli, N. Chiodini, F. Meunardi, M. Nikl, *J. Non-Cryst. Solids* 355 (2009) 1140-1144
- [8] G. De, D. Kundu, B. Karmakar and D. Ganguli, *J. Non-Cryst. Solids* 155 (1993) 253-258
- [9] H. Yoshino, K. Kamiya, and H. Nasu, *J. Non-Cryst. Solids* 126 (1990) 68-78
- [10] O. M. Ntwaeaborwa, H. C. Swart, R. E. Kroon, J. M. Ngaruiya, J. R. Botha, P. H. Holloway, Enhanced Photoluminescence of rare-earth activators in sol-gel derived SiO₂ by energy transfer from ZnO nanoparticles and co-activators, *Nova Science Publishers* (2008) 287-306.
- [11] H. S. Jang, W. B. Im, D. C. Lee, D. Y. Jeon, S. S. Kim, *J. Lumin.* 126 (2007) 371-377
- [12] Z. Nie, K-S. Lim, J. Zhang, X. Wang, *J. Lumin.* 129 (2009) 844-849
- [13] P. Vergeer, V. Babin, A. Meijerink, *J. Lumin.* 114 (2005) 267-274
- [14] A. Meijerink, R. Wegh, P. Vergeer, T. Vlugt, *Opt. Mat.* 28 (2006) 575-581

- [15] L.F Koao, H.C Swart, E Coetsee, M.M Biggs and F.B Dejene, *Phys. B: Phys. Condens. Matter* 404 (2009) 4499 – 4503.
- [16] X. Liu, and J. Lin, *J. Nanopart. Res.* 9 (2007) 869-875
- [17] C. Lin, H. Wang, D. Kong, M. Yu, X. Liu, Z. Wang, and J. Lin, *Eur.J. Inorg. Chem.* (2006) 3667-3675
- [18] V.Kumar, V. Mishra, S. S. Pitale, I. M. Nagpure, E. Coetsee, O. M. Ntwaeaborwa and H. C. Swart, *J. Appl. Phys.* 107 [12] (2010) 123533 (1-6).
- [19] G. H. Mhlongo, O. M. Ntwaeaborwa, M. S Dhlamini, H. C. Swart, K. T. Hillie, *J Mater. Sci.* 45 (2010) 5228-5236
- [20] O.M. Ntwaeaborwa, H.C. Swart, R.E. Kroon, P.H. Holloway and J.R. Botha *J. Phys. Chem. Sol.* 67 (2006) 1749–1753

THE INFLUENCE OF Pr³⁺ CO-DOPING ON THE PL AND CL PROPERTIES OF SiO₂:Eu³⁺/Tb³⁺**7.1 INTRODUCTION**

Enhanced luminescence induced by energy transfer between trivalent rare earth ions co-activators (co-dopants) in a matrix has been demonstrated in nanophosphors for potential application in light emitting devices. Such studies have provided information about the interaction between the activators and the host matrix, as well as insight into long-range interactions and energy transfer between the activator ions. In some cases, co-activators tend to quench the luminescence intensity instead of enhancing it. This is due to the fact that co-doped ions form clusters in a host matrix thus lowering the fluorescence efficiency.

This chapter deals with the synthesis of Pr³⁺ co-activated SiO₂:Eu³⁺/Tb³⁺ using the sol-gel method. The effects of Pr³⁺ co-doping in the luminescence properties under excitation of ultraviolet (UV) light and high energy electrons were demonstrated. Fluorescence quenching effects due to Pr³⁺ co-doping will also be discussed. Further studies on luminescence decay behavior of Tb³⁺-Pr³⁺ and Eu³⁺-Pr³⁺ ion pairs were conducted.

7.2 EXPERIMENTAL**7.2.1 Preparation of SiO₂: Tb³⁺-Pr³⁺ and SiO₂: Eu³⁺-Pr³⁺**

SiO₂ co-doped with different concentrations of Pr³⁺-Tb³⁺ ion pairs samples were prepared by mixing 0.05 mol of TEOS, 0.1 mol of H₂O, 0.1 mol. of ethanol, and 0.145 mol of dilute nitric acid were stirred at room temperature for 1 hour resulting in

a clear sol. The sol was then mixed with a desired amount of $\text{Pr}(\text{NO})_3 \cdot 6\text{H}_2\text{O}$ dissolved in 5 ml of ethanol and stirred for 30 minutes. A desired amount of $\text{Tb}(\text{NO})_3 \cdot 6\text{H}_2\text{O}$ dissolved in 5 ml of ethanol was also added to the mixture and stirred further for 30 minutes until a gel formed. The gel was then transferred into a petri dish and was dried at room temperature for 8 days. The dried gel was ground and then heat treated at $600\text{ }^\circ\text{C}$ for 2hrs in ambient air. A similar procedure was followed for preparation of $\text{SiO}_2:\text{Pr}^{3+}\text{-Eu}^{3+}$ samples.

The CL data were recorded using an Ocean Optics S2000 Spectrometer attached to an ultra high vacuum chamber of the Physical Electronics PHI 549 Auger Electron Spectrometer. The phosphor powders were irradiated with an electron beam accelerated at 2 kV and beam current of $20\text{ }\mu\text{A}$ at a high vacuum base pressure of 1.6×10^{-8} Torr. The excitation and emission data of the SiO_2 co-doped $\text{Tb}^{3+}\text{-Pr}^{3+}$ and $\text{Eu}^{3+}\text{-Pr}^{3+}$ were carried out at room temperature using a DongWoo Optron Co. setup, consisting of DM711 and DM152i monochromators equipped with a Xe Arc lamp DL180-Xe. The decay curves of the phosphor samples were obtained from an optical parametric oscillator (OPO Continuum Surelite) pumped by third harmonics of Nd:YAG laser as an excitation source. The decay signals were detected, and stored with a Tektronix TDS 3052 digital oscilloscope. The particle morphology was analyzed by JEOL 2100 High Resolution Transmission Electron Microscopy (HRTEM) and Field Emission-Scanning Electron Microscope (FE-SEM) while the chemical composition of the phosphor powders was analyzed by Energy Dispersive Spectrometer (EDS). The X-Ray Diffraction data were collected using X-Ray diffractometer (Phillips Xpert) using a $\text{Cu K}\alpha$ ($\lambda=1.5405\text{ \AA}$) radiation to study the crystal structure of phosphor samples.

7.3 RESULT AND DISCUSSION

7.3.1 Phase and structure analysis (XRD)

The XRD patterns from SiO_2 :1 mol% Tb^{3+} -0.2 mol% Pr^{3+} and SiO_2 :1 mol% Eu^{3+} -0.2 mol% Pr^{3+} phosphor powders did not show any detectable diffraction peaks from Tb^{3+} , Pr^{3+} , and Eu^{3+} either before or after calcining at 600°C . Instead, their diffraction peaks resembled that of pure SiO_2 which showed one well known broad diffraction peak of amorphous SiO_2 at $2\theta = 22^\circ$ similar to the patterns shown in Fig. 4.2.

7.3.2 Elemental analysis (EDS)

The EDS spectra obtained from SiO_2 :1 mol% Eu^{3+} -0.2 mol% Pr^{3+} and SiO_2 :1 mol% Tb^{3+} -0.2 mol% Pr^{3+} in figure 7.1 (a) and (b), respectively, showed some traces of Si, O, Pr, Eu, and Tb ions [1]. HRTEM images (results not shown) from these phosphor powders on the other hand confirmed the successful incorporation of Pr^{3+} , Eu^{3+} , Tb^{3+} , and Ce^{3+} ions. These were evidenced by the presence of some black spots with irregular shape randomly distributed inside the amorphous structure of SiO_2 which were not observed from pure SiO_2 image. The FE-SEM images (see fig.4.3) revealed the agglomeration of mostly spherical SiO_2 particles with an average particle size in the range of ~20 to 120 nm in diameter [1].

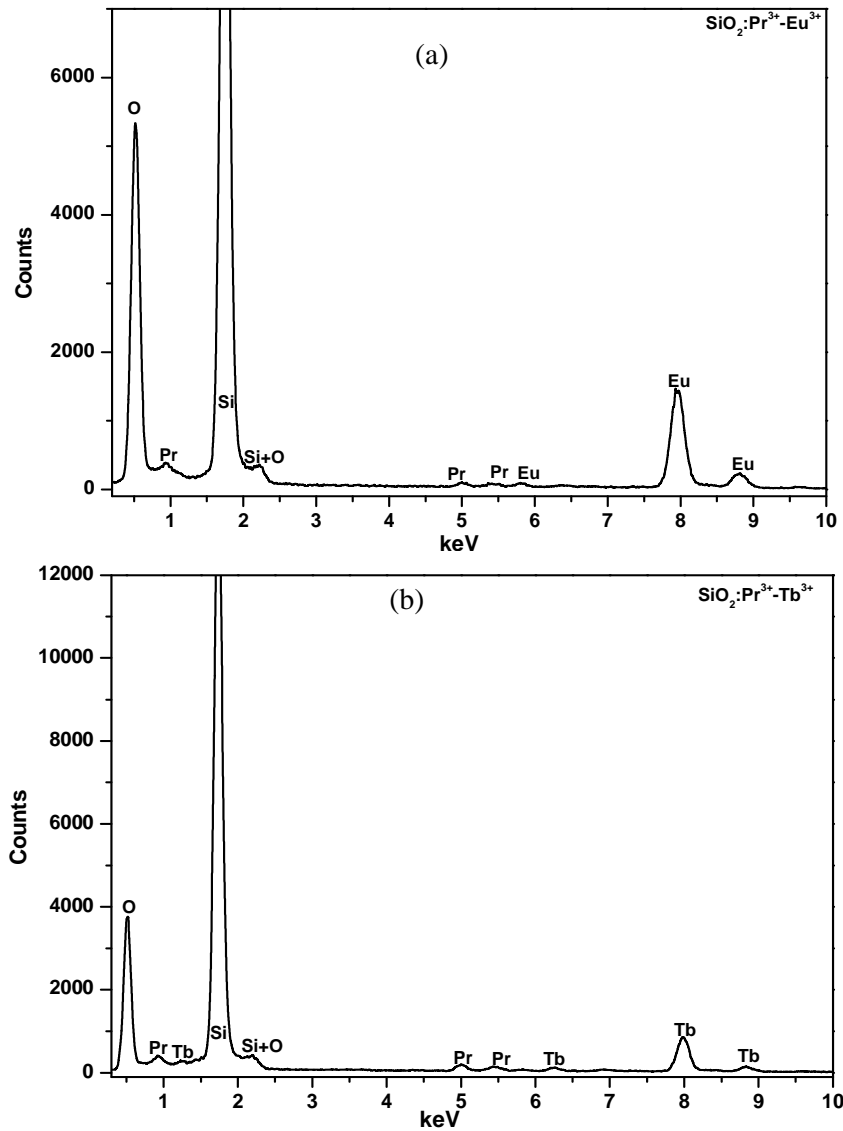


Fig. 7.1 EDS spectra of (a) $\text{SiO}_2:1 \text{ mol}\% \text{Eu}^{3+}-0.2 \text{ mol}\% \text{Pr}^{3+}$ and (b) $\text{SiO}_2:1 \text{ mol}\% \text{Tb}^{3+}-0.2 \text{ mol}\% \text{Pr}^{3+}$.

7.3.2 PL properties of $\text{SiO}_2:\text{Eu}^{3+}-\text{Pr}^{3+}$ and $\text{SiO}_2:\text{Tb}^{3+}-\text{Pr}^{3+}$

In order to evaluate the effect of Pr^{3+} co-doping in $\text{SiO}_2:\text{Eu}^{3+}$, the photoluminescence properties were investigated. In figure 7.2, the PL emission spectra of $\text{SiO}_2:1 \text{ mol}\% \text{Eu}^{3+}$ and $\text{SiO}_2:1 \text{ mol}\% \text{Eu}^{3+}-0.2 \text{ mol}\% \text{Pr}^{3+}$ obtained after excitation at 395 nm are compared. It can be seen from the spectra that the emission associated with ${}^5\text{D}_0 \rightarrow {}^7\text{F}_J$ ($J=0, 1, 2, 3, 4$) transitions of Eu^{3+} with the intense red emission

corresponding to ${}^5D_0 \rightarrow {}^7F_2$ transition were observed. The emission peaks around 580 and 590 nm are due to ${}^5D_0 \rightarrow {}^7F_0$ and ${}^5D_0 \rightarrow {}^7F_1$ transition of Eu^{3+} , respectively. The other emission peaks centred at 650 and 700 nm arises from the ${}^5D_0 \rightarrow {}^7F_3$ and ${}^5D_0 \rightarrow {}^7F_4$, respectively.

The assignment of these emission peaks is in accordance with the previous work reported by Changqing *et al.* [2] and Wang *et al.* [3] for $\text{SiO}_2:\text{Eu}^{3+}$ phosphors. It can be noticed from the figure 7.2 that these emissions were quenched after Pr^{3+} co-doping and no transitions of Pr^{3+} were detected. Above all, no change in the peak shape was observed, which indicates no contribution from Pr^{3+} . These results confirm the observation of Kandpal *et al.* [4] for $\text{Pr}^{3+}\text{-Eu}^{3+}$ ion pairs co-doped in dimethylsulphoxide (DMSO) system where the significant decrease with Pr^{3+} co-doping and increasing Pr^{3+} concentration was reported.

The supporting evidence of the luminescence quenching due to Pr^{3+} co-doping was also observed by comparing the excitation spectra of $\text{SiO}_2:1 \text{ mol\% Eu}^{3+}$ and $\text{SiO}_2:1 \text{ mol\% Eu}^{3+}\text{-}0.2 \text{ mol\% Pr}^{3+}$ monitoring the emission peak at 614 nm as shown in figure 7.3. Both excitation spectra exhibited a series of peaks in the region of 300 and 540 nm corresponding to ${}^7F_0 \rightarrow {}^5D_J$ ($J=1, 2, 3, 4$), ${}^7F_0 \rightarrow {}^5G_J$, ${}^7F_0 \rightarrow {}^5H_3, {}^5H_6$, with the intense absorption band at 395 nm attributed to ${}^7F_0 \rightarrow {}^5L_6$ of Eu^{3+} . The assignment of these peaks compares well with the results of Wang *et al.* [3] and Dejneka *et al.* [5] for Eu^{3+} in SiO_2 and fluoride glasses, respectively. It was noted that the excitation spectra of $\text{SiO}_2:1 \text{ mol\% Eu}^{3+}\text{-}0.2 \text{ mol\% Pr}^{3+}$ emission is very similar to that of singly doped Eu^{3+} in SiO_2 except that it is 90 % less intense in comparison with $\text{SiO}_2:\text{Eu}^{3+}$. Similar observations were also reported by Meijerink *et al.* [6] for $\text{Tb}^{3+}\text{-Yb}^{3+}$ ion pairs in YPO_4 system.

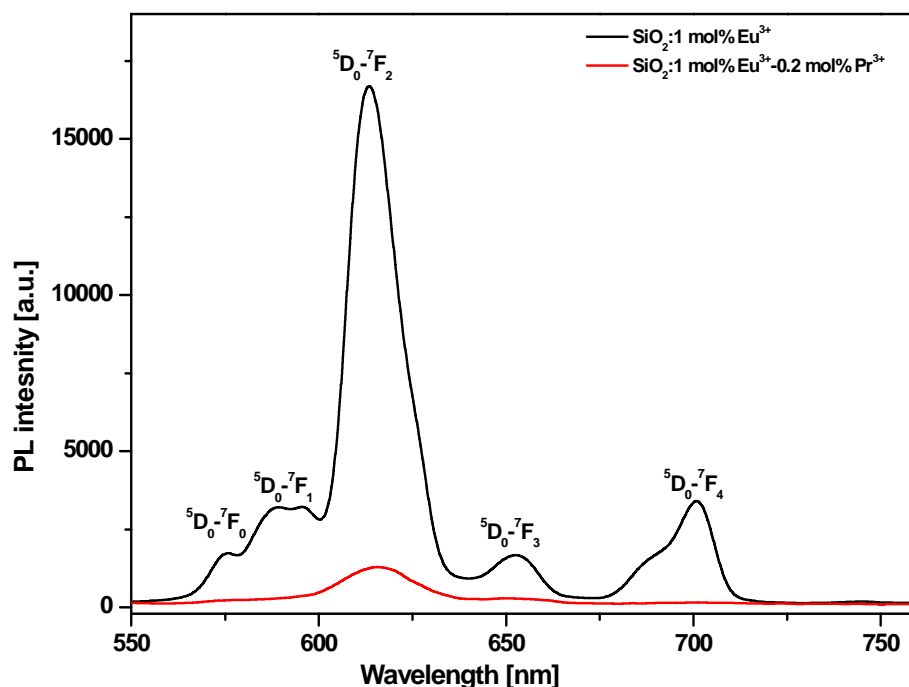


Fig.7.2 Emission spectra of $\text{SiO}_2:1 \text{ mol\% Eu}^{3+}$ and $\text{SiO}_2:1 \text{ mol\% Eu}^{3+}-0.2 \text{ mol\% Pr}^{3+}$ nanophosphors after excitation at 395 nm at room temperature using a Xenon lamp.

We also investigated the effects of Pr^{3+} co-doping in luminescence intensity of $\text{SiO}_2:\text{Tb}^{3+}$. In this case it was expected that an increase in Pr^{3+} concentration from 0.2 to 1 mol% will further reduce the $\text{Tb}^{3+} \ ^5\text{D}_4$ emission lines and the $\text{Pr}^{3+} \ ^1\text{D}_2$ or $^3\text{P}_0$ emission will be pronounced due to energy transfer from Tb^{3+} to Pr^{3+} . Such results were reported by Mahato *et al.* [7] for $\text{Tb}^{3+}-\text{Pr}^{3+}$ ions co-doped into oxyfluoroborate glass. The emission spectra of $\text{SiO}_2:1 \text{ mol\% Tb}^{3+}$ and $\text{SiO}_2:1 \text{ mol\% Tb}^{3+}-0.2 \text{ mol\% Pr}^{3+}$ were compared and are shown in figure 7.4. These spectra were collected after excitation at 379 nm at room temperature. Both spectra consist of the green emission which can be attributed to the $^5\text{D}_4 \rightarrow ^7\text{F}_J$ ($J=4, 5, 6$) transitions of Tb^{3+} and the emission peaks appear at 489, 543, 549, 584, 622 nm, respectively. These results agrees well with results reported elsewhere [7,8-10].

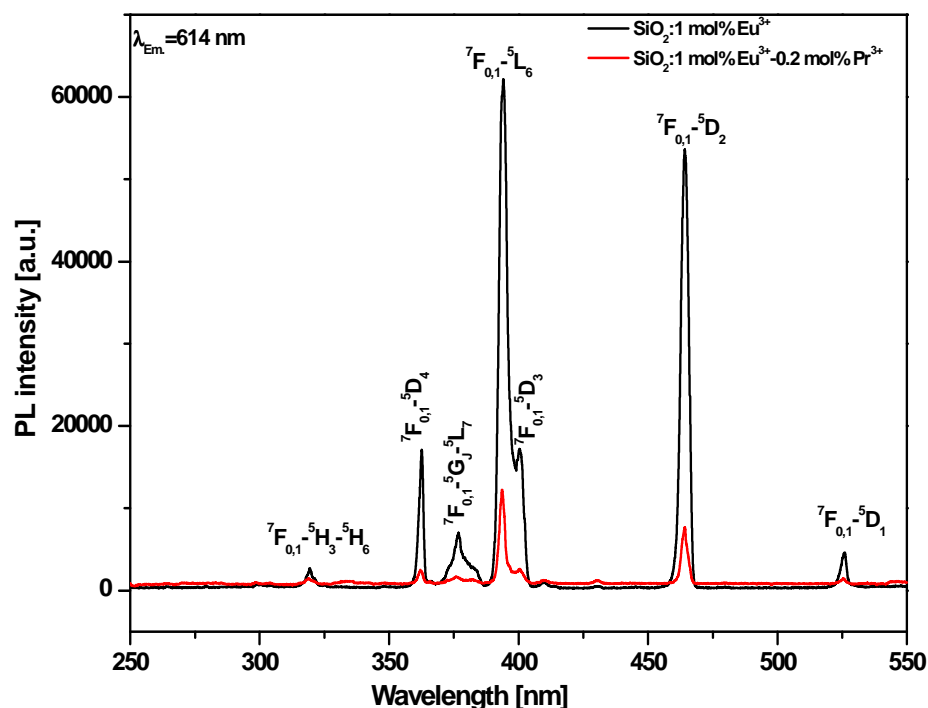


Fig. 7.3 Excitation spectra of $\text{SiO}_2:1 \text{ mol}\% \text{Eu}^{3+}$ and $\text{SiO}_2:1 \text{ mol}\% \text{Eu}^{3+}-0.2 \text{ mol}\% \text{Pr}^{3+}$ after monitoring the emission peak at 614 nm at room temperature.

The strongest emission is centred at 543 nm and it corresponds to the ${}^5\text{D}_4 \rightarrow {}^7\text{F}_5$ transition of Tb^{3+} . Again, when adding the Pr^{3+} ion, the luminescence intensity from Tb^{3+} is significantly quenched.

Figure 7.5 shows the excitation spectra of $\text{SiO}_2:1 \text{ mol}\% \text{Tb}^{3+}$ and $\text{SiO}_2:1 \text{ mol}\% \text{Tb}^{3+}-0.2 \text{ mol}\% \text{Pr}^{3+}$ obtained while monitoring the green emission at 543 nm. The excitation peaks are assigned according to previous reports [7,11]. As shown in both spectra, no excitation peaks from Pr^{3+} could be observed and the Tb^{3+} excitation peaks are quenched with Pr^{3+} co-doping.

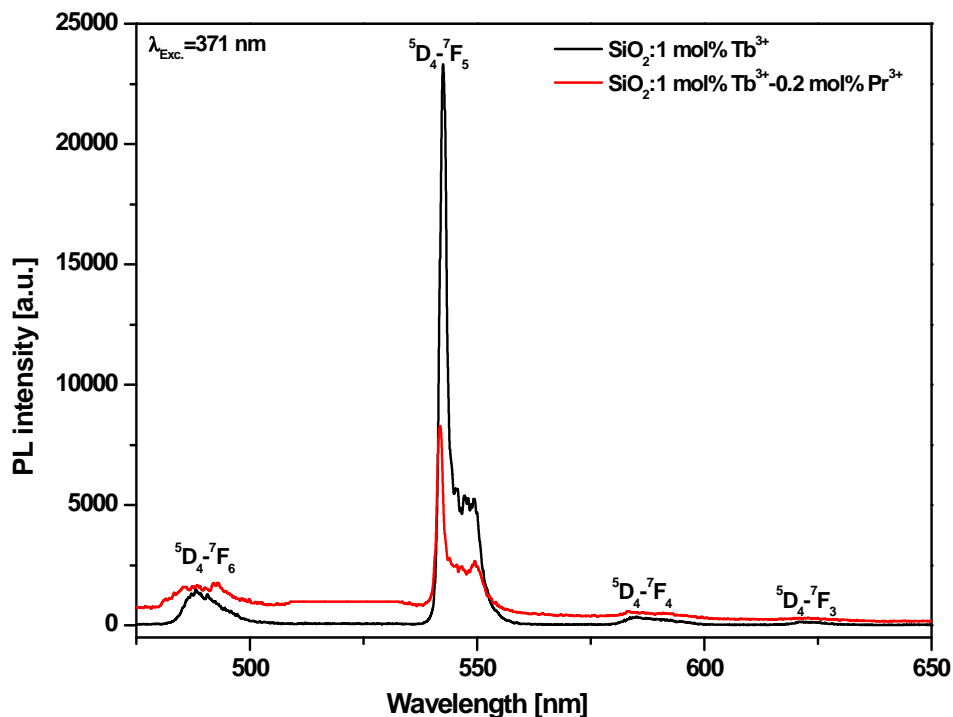


Fig. 7.4 Emission spectra of $\text{SiO}_2:1 \text{ mol\% Tb}^{3+}$ and $\text{SiO}_2:1 \text{ mol\% Tb}^{3+}-0.2 \text{ mol\% Pr}^{3+}$ nanoposphor powders obtained after excitation at 379 nm at room temperature.

The strong quenching is apparent from all Pr^{3+} co-doped $\text{SiO}_2:\text{Eu}^{3+}/\text{Tb}^{3+}$ phosphors powders. There two possible reasons which may be the cause of this. First, the aggregation of Pr^{3+} ions or pairing Pr^{3+} ions with $\text{Eu}^{3+}/\text{Tb}^{3+}$ ions. Such process leads to migration of excitation energy from one activator ion to its nearest ion by non-radiative transitions and via a large number of transfer steps, before the energy is released. During the transfer process, the energy can be transferred to defects which act as energy sinks within a transfer chain thus leading to a significant decrease on the PL intensity. In this case, it is most likely to happen that the energy may be exhausted by Killer or/and defect during the energy process among one kind of Pr^{3+} ions prior to the other kind of $\text{Eu}^{3+}/\text{Tb}^{3+}$ ion. Secondly, it is also possible that the interaction between $\text{Pr}^{3+}-\text{Eu}^{3+}$ and $\text{Pr}^{3+}-\text{Tb}^{3+}$ ion pairs is through a $\text{Pr}^{4+}-\text{Eu}^{2+}$ and $\text{Pr}^{4+}-\text{Tb}^{2+}$ metal-metal charge transfer state and this energetically overlaps the Tb^{3+} ($^5\text{D}_4$) level and Eu^{3+} ($^5\text{D}_0$) level hence the strong quenching.

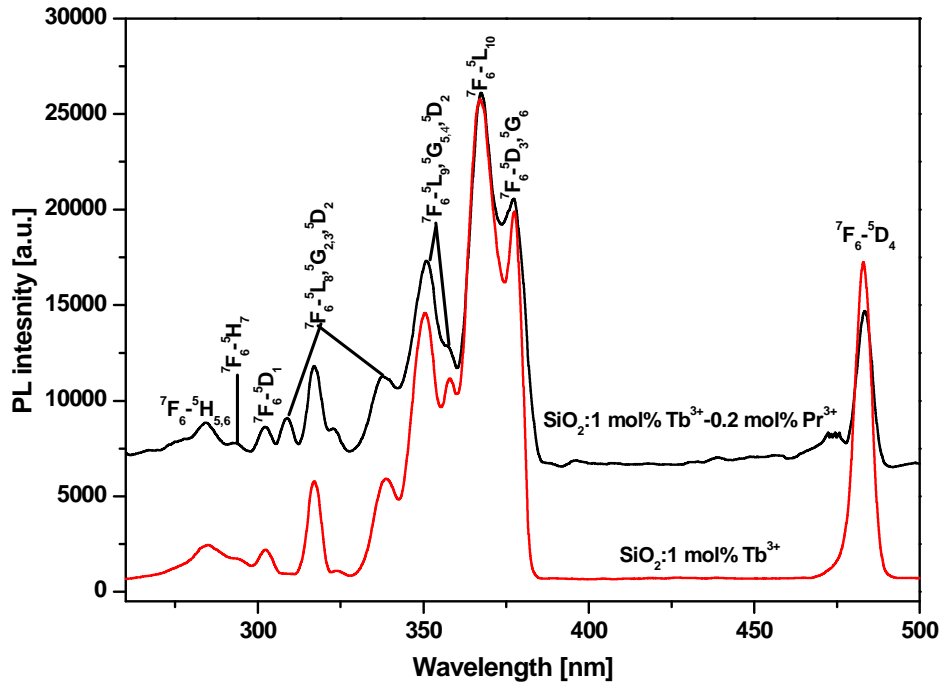


Fig. 7.5 Excitation spectra of $\text{SiO}_2:1 \text{ mol}\% \text{ Tb}^{3+}$ and $\text{SiO}_2:1 \text{ mol}\% \text{ Tb}^{3+}-0.2 \text{ mol}\% \text{ Pr}^{3+}$ obtained after monitoring Tb^{3+} emission at 543 nm at room temperature.

The quenching of luminescence with Pr^{3+} addition can also be caused by cross relaxation between Pr^{3+} ions. This process is described by energy transfer from one Pr^{3+} to another Pr^{3+} neighbouring ion by transition that matched in energy. In this case of Pr^{3+} , the $^3\text{P}_0$ and $^1\text{D}_2$ emission can be quenched with $^1\text{D}_2$ level of Pr^{3+} ion through cross-relaxation patterns such as (i) $^5\text{D}_0 \rightarrow ^7\text{F}_{0,1,2} = ^3\text{H}_4 \rightarrow ^1\text{D}_2$ (ii) $^5\text{D}_1 \rightarrow ^7\text{F}_{2,3,4} = ^3\text{H}_4 \rightarrow ^1\text{D}_2$ as these transitions are resonant with emission of phonons [12]. Previous studies revealed that, at low Pr^{3+} concentrations, the most intense emission corresponds to the $^1\text{D}_2 \rightarrow ^3\text{H}_4$ transition. However, this transition shows a strong quenching with increasing Pr^{3+} or at high Pr^{3+} concentrations and the most prominent emission from the $^3\text{P}_0$ transition. This strong quenching of the $^1\text{D}_2$ emission is often observed in the emission spectra of Pr^{3+} and has been attributed to cross-relaxation between Pr^{3+} ions [12,13]. Blasse and Gabmaier [14] put forward some theoretical explanations of the concentration quenching effect and they suggested that when the

concentration of doped ions is higher than a threshold, the nonradiative energy transfer between neighbouring dopant ions will kill the fluorescence. Since the probability of the energy transfer is proportional to R^{-6} , where R is the distance between the dopant ions [14], the formation of pairs of dopant ions is the major cause of fluorescence quenching.

The other major reason which might have an impact on the quenching of fluorescence is presence of residual hydroxyl groups (OH) in SiO₂ glass even after annealing at higher temperatures. Most of sol gel derived rare earth doped glasses have been reported to suffer from this process due to the abundance of OH⁻ groups in the material which are formed due to the presence of water in the starting sol, and water generated during condensation reactions in the sol-gel process. The OH ions have strong absorption band from 2000 to 4000 cm⁻¹ and their presence near the rare earth ions provides non-radiative decay paths for the excited rare earth ion thus decreasing fluorescence yield [9].

In order to obtain additional information on the luminescence properties of Pr³⁺ co-doped SiO₂:Eu^{3+/Tb}³⁺, the luminescence decay curves of ⁵D₃ and ⁵D₄ levels of Eu³⁺ and Tb³⁺ were investigated. Figure 7.6 shows the room temperature luminescence decay curves of the PL emission (a) at 614 nm from ⁵D₃→⁷F₂ transition of Eu³⁺ and Eu³⁺-Pr³⁺ in SiO₂, and (b) at 543 nm from ⁵D₄→⁷F₅ transition of Tb³⁺ and Tb³⁺-Pr³⁺ in SiO₂. In general, if one kind of luminescence centre exists in a phosphor material, then the decay function can be fitted by the first order exponential equation. If two centres exist in a phosphor then the decay function can be fitted by the second order exponential equation and so on. In addition, the behavior of the decay function can also be influenced by the presence of energy transfer and impurities in the host matrices. In the current study, the luminescence decay curves were all fitted using the

first order exponential profile. The fitted lifetime of Tb^{3+} ($^5\text{D}_4$ level) singly doped SiO_2 was determined to be 3.3 ms while that of Pr^{3+} co-doped $\text{SiO}_2:\text{Tb}^{3+}$ was 0.9 ms. The similar behavior was observed for $\text{SiO}_2:\text{Eu}^{3+}-\text{Pr}^{3+}$ whose lifetime was 0.9 ms and also shorter than that of Eu^{3+} singly doped SiO_2 which had a lifetime of 2.3 ms. These results compare very well with the observations of Jie *et al.* [15] who observed the lifetime of 1.30 ms for $\text{Lu}_2\text{O}_3:5 \text{ mol\% Eu}^{3+}$ film which was reduced by 3/4 due to addition of 0.1 mol% Pr^{3+} . The decay was even faster with increasing Pr^{3+} concentration (0.3 and 0.5 mol%). For $\text{Tb}^{3+}-\text{Pr}^{3+}$ ion pairs in oxyfluoroborate glass, Mahato *et al.* [7] reported that the lifetime of the $^5\text{D}_4$ level of Tb^{3+} was reduced to 1.1 ms from 1.7 ms for the sample having 1 mol% $\text{Tb}^{3+}-1 \text{ mol\% Pr}^{3+}$ and further reduced to 0.8 ms for 1 mol% $\text{Tb}^{3+}-3 \text{ mol\% Pr}^{3+}$. It is obvious from our results that the luminescence from Eu^{3+} ($^5\text{D}_3$ level) and Tb^{3+} ($^5\text{D}_4$ level) decay faster with Pr^{3+} co-doping as evidenced by shortening of lifetimes. Such phenomenon confirms the quenching effect of Pr^{3+} ions.

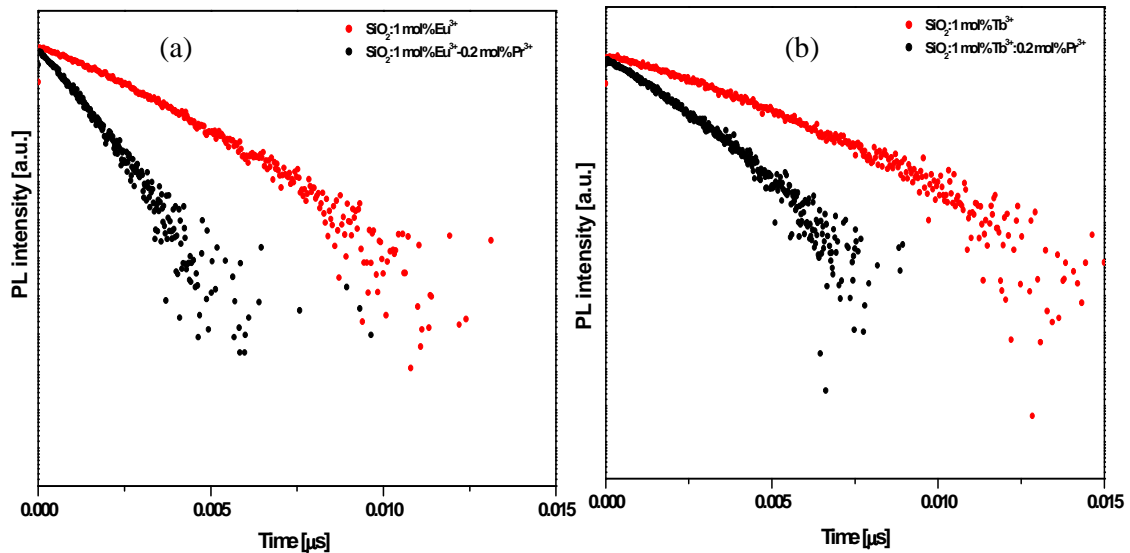


Fig. 7.6 Decay curves for the $^5\text{D}_4-^7\text{F}_5$ transition of Tb^{3+} in SiO_2 for 0.2, 0.5, and 1 mol% concentrations of Pr^{3+} while the Tb^{3+} concentration was kept at 0.2 mol%.

7.3.3 CL properties of $\text{SiO}_2:\text{Eu}^{3+}\text{-Pr}^{3+}$ and $\text{SiO}_2:\text{Tb}^{3+}\text{-Pr}^{3+}$

In order to verify our observations from PL, the CL properties of Pr^{3+} co-doped in $\text{SiO}_2:\text{Eu}^{3+}/\text{Tb}^{3+}$ phosphors powders were investigated. Figure 7.7 presents the CL spectra of $\text{SiO}_2:1 \text{ mol}\% \text{ Tb}^{3+}$, $\text{SiO}_2:1 \text{ mol}\% \text{ Tb}^{3+}\text{-}0.2 \text{ mol}\% \text{ Pr}^{3+}$ phosphor powders under irradiation of 2 kV, 20 μA beam current in a high vacuum chamber containing a base pressure of $\sim 1.6 \times 10^{-8}$ Torr. It was noticed that under low-voltage electron beam excitation, both $\text{SiO}_2:\text{Tb}^{3+}$, $\text{SiO}_2:\text{Tb}^{3+}\text{-Pr}^{3+}$ phosphor powders exhibited typical emission lines of Tb^{3+} located 410 nm ($^5\text{D}_3 \rightarrow ^7\text{F}_4$), 433 nm ($^5\text{D}_3 \rightarrow ^7\text{F}_3$), 488 nm ($^5\text{D}_4 \rightarrow ^7\text{F}_6$), 543 nm ($^5\text{D}_4 \rightarrow ^7\text{F}_5$), 588 nm ($^5\text{D}_4 \rightarrow ^7\text{F}_4$), and 622 nm ($^5\text{D}_4 \rightarrow ^7\text{F}_3$). The strongest green emission originates from the $^5\text{D}_4 \rightarrow ^7\text{F}_5$ transition at 543 nm. The CL intensity from $\text{SiO}_2:\text{Tb}^{3+}\text{-Pr}^{3+}$ was 95% less than that of $\text{SiO}_2:\text{Tb}^{3+}$.

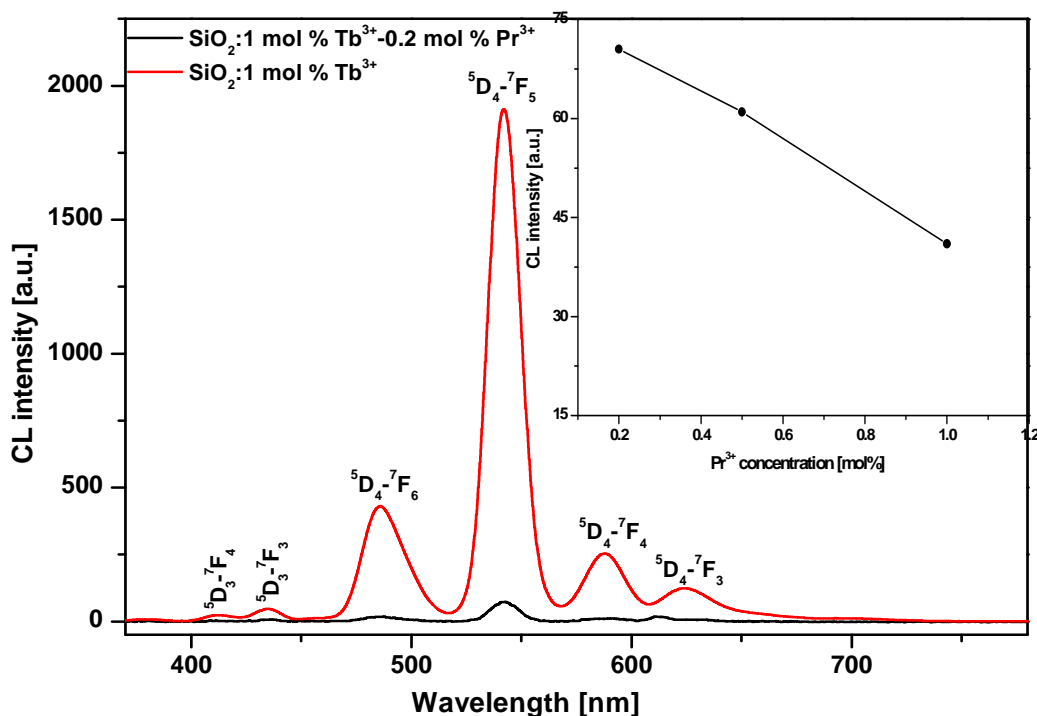


Fig. 7.7 CL spectra of $\text{SiO}_2:1 \text{ mol}\% \text{ Tb}^{3+}$, and $\text{SiO}_2:1 \text{ mol}\% \text{ Tb}^{3+}\text{-}0.2 \text{ mol}\% \text{ Pr}^{3+}$ samples irradiated with 2kV, 20 μA beam of electrons in a high vacuum chamber containing a base pressure of $\sim 1.6 \times 10^{-8}$ Torr. The insert shows the CL intensity from $\text{SiO}_2:\text{Pr}^{3+}\text{-Tb}^{3+}$ as a function of 0.2, 0.5, and 1 mol% Pr^{3+} concentrations.

Similar results were observed where the same phosphor samples were excited using UV light. However, we also observed that the 5D_3 emission lines can be hardly observed in the PL emission spectrum under UV light excitation, but they can be seen in CL spectrum for the identical samples. Significant decrease in Tb^{3+} emission with increasing Pr^{3+} concentration was observed as clearly indicated in the insert of figure 7.7.

Figure 7.8 presents the CL spectra of $SiO_2:1 \text{ mol\% } Eu^{3+}$, $SiO_2:1 \text{ mol\% } Eu^{3+}-0.2 \text{ mol\% } Pr^{3+}$ phosphor powders under irradiation of 2 kV, 20 μA beam current in a high vacuum chamber containing a base pressure of $\sim 1.6 \times 10^{-8}$ Torr. For $SiO_2:Pr^{3+}$, the emission lines which correspond to the $f-f$ transitions of Pr^{3+} from $^3P_0 \rightarrow ^3H_4$, 3H_6 , 3F_2 , $^3F_{3,4}$, and $^1D_2 \rightarrow ^3H_4$, 3H_5 , 3F_4 with the main red emission at 614 nm assigned to $^1D_2 \rightarrow ^3H_4$ were observed. When Eu^{3+} is co-doped with Pr^{3+} , the Pr^{3+} emission was still present and no emission from Eu^{3+} was observed. These results confirm the observations of Zachau *et al.* [16]. The CL intensity kept on dropping with increasing concentrations of Pr^{3+} (0.5 and 1 mol%) as shown in the insert of figure 7.8. It was noticed that both the CL emission spectra from $SiO_2:Eu^{3+}/Tb^{3+}$ with co-doped Pr^{3+} exhibited strong quenching from Tb^{3+} emission and Pr^{3+} emission.

However, we observed an obvious difference between the CL and PL emission spectra obtained from phosphor samples and such difference may be attributed to two possible factors. First, the difference of excitation mechanisms involved in the PL and CL. During the PL process, the photons used for excitation have energy less than the bandgap of the host matrix so that no electron-hole pairs are generated. The luminescent centre is excited using a wavelength lying in the absorption band which will then non-radiatively relax to the ground state after a short while by emitting photons corresponding to specific transitions localized within the centre itself. In the

case of CL, the generation of charge carriers (electrons and holes) under irradiation by energetic electrons occurs through impact ionization. As a result, the accelerated electrons create a multiplicity of charge carriers and the excitation energy is transferred by excitons to luminescent centres.

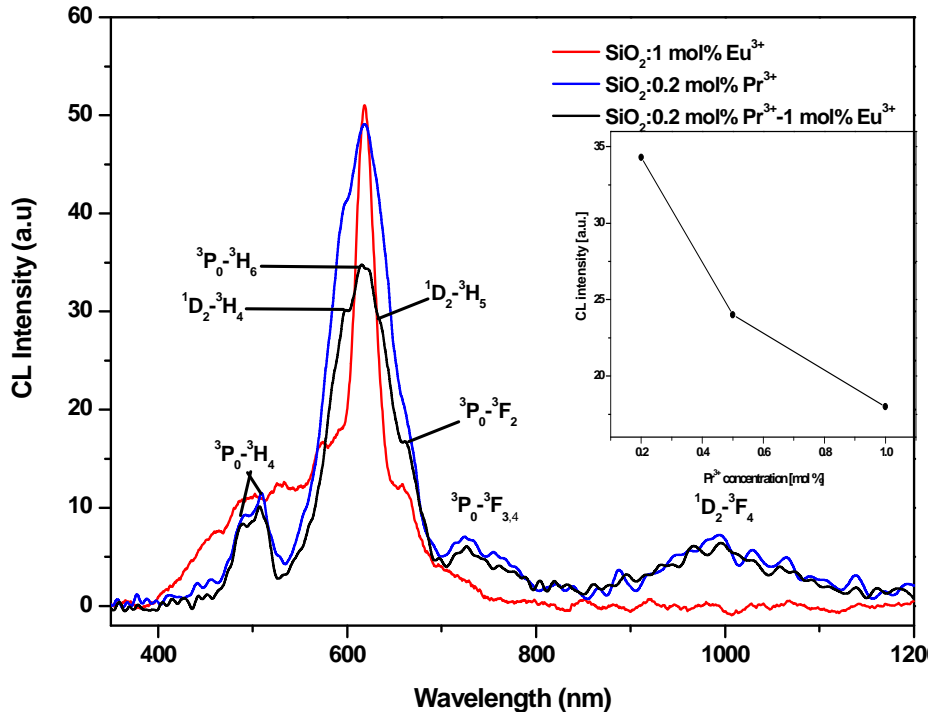


Fig. 7.8 CL intensities of $\text{SiO}_2:1 \text{ mol}\% \text{Eu}^{3+}$ - $0.2 \text{ mol}\% \text{Pr}^{3+}$ and $\text{SiO}_2:0.2 \text{ mol}\% \text{Pr}^{3+}$ at 2kV, 20 μA in 1×10^{-7} Torr, O_2 as a function of electron dose. The insert shows the CL intensity from $\text{SiO}_2:\text{Pr}^{3+}\text{-Eu}^{3+}$ as a function of 0.2, 0.5, and 1 mol% Pr^{3+} concentrations.

The second factor is associated with the presence of local saturation effect. In comparison with the UV excitation, the excitation intensity and excitation density of luminescence centres are very high under low-voltage electron beam bombardment. As a result, in the case of Tb^{3+} doped samples, the cross relaxation ${}^5\text{D}_3 + {}^7\text{F}_6 \rightarrow {}^5\text{D}_4 + {}^7\text{F}_0$ may be suppressed, hence, the appearance of the ${}^5\text{D}_3$ emission from the CL emission spectra. In the case of $\text{SiO}_2:\text{Eu}^{3+}\text{-Pr}^{3+}$ the strong quenching from Pr^{3+} emission was observed and this behavior is different from the PL spectra of identical samples. This

can be due to the fact that when this phosphor sample is excited with energetic electrons, the radiative process from Pr^{3+} occurs faster than that of Eu^{3+} .

7.4 CONCLUSION

The CL and PL properties of $\text{SiO}_2:\text{Tb}^{3+}/\text{Eu}^{3+}$ co-doped with Pr^{3+} derived from sol gel method were studied by varying the concentration of Pr^{3+} . The strong fluorescence quenching with Pr^{3+} addition was observed from both $\text{SiO}_2:\text{Tb}^{3+}/\text{Eu}^{3+}$ co-doped with Pr^{3+} nanophosphor powders. The possible reasons which might have been the main cause of this quenching are discussed in detail. The decay measurements of $\text{SiO}_2:\text{Tb}^{3+}/\text{Eu}^{3+}$ co-doped with Pr^{3+} exhibited shorter lifetimes.

7.5 REFERENCES

- [1] G.H. Mhlongo, O.M. Ntwaeaborwa, M.S. Dhlamini, H.C. Swart, K.T. Hillie, *J. Alloys Compd.* 509 (2011) 2986-2992.
- [2] H. Changqing, S. Ting, T. Weijian, Z. Baoping, *J. Rare Earths* 24 (2006) 134-137
- [3] R. Y. Wang, *J. Lumin.* 106 (2004) 211-217
- [4] H. C. Kandpal and H. B Tripathi, *Solid State Comm.* 29 (1979) 139-142
- [5] M. Dejneka, E. Snitzer, R. E. Riman, *J. Lumin.* 65 (1995) 227-245
- [6] A. Meijerink, R. Wegh, P. Vergeer, T. Vlugt, *Opt. Mater.* 28 (2006) 575-581
- [7] K. K. Mahato, S. B. Rai, *Spectrochim. Acta Part A* 56 (2000) 2333-2340
- [8] X. Liu, R. Pang, Q. Li, J. Lin, *J. Solid State Chem.* 180 (2007) 1421-1430
- [9] A. J. Silversmith, D. M. Boye, K. S. Brewer, C. E Gillespie, Y. Lu, D. L. Campbell, *J. Lumin.* 121 (2006) 14-20
- [10] G. Wakefield, H. A. Keron, P. J. Dobson, J. L. Hutchison, *J. Phys. Chem. Sol.* 60 (1999) 503-508
- [11] K. Binnemans, C. Gorller-Walrand, *Chem. Phys. Lett.* 235 (1995) 163-174
- [12] P. Solarz, W. Ryba-Ramanowski, *Radiat. Meas.* 42 (2007) 759-762
- [13] R. Balda, J. Fernandez, I. Saez de Ocariz, J.L. Adam, A. Mendioroz, E. Montoya, *Opt. Mater.* 13 (1999) 159-165.
- [14] G. Blasse, B.C Grabmaier, Luminescence materials, *Springer-Verlag Berlin*, (1994)
- [15] X. Jie, D. Lianyun, S. Ying, X. Jianjun, Q. Huajun, S. Guoxin, *J. Lumin.* (2011)
- [16] M. Zachau, F. Zwaschka, and F. Kummer, *Proc. Electrochem. Soc.* 97-29

SUMMARY AND CONCLUSION

The CL and PL properties of $\text{SiO}_2:\text{Tb}^{3+}/\text{Eu}^{3+}$ co-doped with Pr^{3+} derived from sol gel method were studied. It was found that co-doping Pr^{3+} into $\text{SiO}_2:\text{Tb}^{3+}/\text{Eu}^{3+}$ phosphors strongly quenches the CL and PL intensities of $\text{SiO}_2:\text{Pr}^{3+}-\text{Eu}^{3+}$ and $\text{SiO}_2:\text{Pr}^{3+}-\text{Tb}^{3+}$ nanophosphor powders. Possible reasons which might be the major cause of this fluorescence quenching were discussed in detail. The luminescence decay measurements exhibited shorter lifetimes from $\text{SiO}_2:\text{Tb}^{3+}/\text{Eu}^{3+}$ co-doped with Pr^{3+} samples which indicates the introduction of extra radiative channels due the presence of energy transfer between these ion pairs.

The CL intensity behavior of the $\text{SiO}_2:\text{Pr}^{3+}-\text{Ce}^{3+}$ nanophosphor at different Ce^{3+} concentrations, beam voltages and currents was also presented. The CL emission from Ce^{3+} (blue) together with a small shoulder from Pr^{3+} (red) with the blue emission from Ce^{3+} dominating was observed when the concentration of both ions was 0.2 mol%. However, when the Ce^{3+} concentration was increased to 1 mol% Ce^{3+} while that of Pr^{3+} was kept to 0.2 mol%, the red Pr^{3+} emission was quenched and enhanced blue emission from Ce^{3+} was more pronounced than that of singly doped Ce^{3+} . Such behavior was attributed to energy transfer from Pr^{3+} to Ce^{3+} . An increase in the CL intensity was found to increase with increasing beam voltage and current. No saturation was observed which is good for field emission display technology.

Red emission originating from both $^3\text{P}_0$ and $^1\text{D}_2$ emitting levels of Pr^{3+} was observed from both $\text{SiO}_2:\text{Pr}^{3+}$ with and without embedded ZnO nanoparticles. Enhanced red emission from Pr^{3+} doped SiO_2 was achieved by incorporating ZnO nanoparticles and this indicates that ZnO act as an effective sensitizer for Pr^{3+} emission. The luminescence enhancement from Pr^{3+} with quenching of green

emission from ZnO was attributed to energy transfer from ZnO to Pr^{3+} . $^1\text{D}_2$ level showed the longer lifetime compared to the $^3\text{P}_0$ level as observed from luminescence decay data. Investigation of the luminescence of Pr^{3+} in SiO_2 as a function of Pr^{3+} concentration revealed the shortening of $^1\text{D}_2$ lifetime with increasing Pr^{3+} concentration i.e above 0.2 mol%. The concentration quenching effect due to migration of excitation energy among Pr^{3+} ions was speculated to be the main effect of self-quenching of the $^1\text{D}_2$ level. The $^1\text{D}_2$ level was also found to be influenced by temperature as its lifetime slowly decreased with increasing temperature from 8 to 300 K.

The CL intensity degradation from the $\text{SiO}_2:\text{Pr}^{3+}-\text{Ce}^{3+}$, $\text{SiO}_2:\text{Pr}^{3+}$ and $\text{ZnO}:\text{SiO}_2:\text{Pr}^{3+}$ nanophosphors powders corresponds to the decrease of the Auger peak intensity of O after electron bombardment of the phosphor surface for several hours. Formation of an oxygen-deficient surface dead or non luminescent layer of SiO_x , where $x < 2$ on the surface is believed to be the main cause of CL degradation of $\text{SiO}_2:\text{Pr}^{3+}-\text{Ce}^{3+}$, $\text{SiO}_2:\text{Pr}^{3+}$ and $\text{ZnO}:\text{SiO}_2:\text{Pr}^{3+}$ nanophosphors powders.

FUTURE PROSPECTS

Trivalent Pr^{3+} has been specially found to be attractive as it offers the effective infrared emission for optical amplification at 1.3- μm and the possibility of simultaneous blue-green-red emission for laser action, information display and optical imaging, as well as infrared to short wavelength emission through an up-conversion emission process. However, self-quenching of the luminescence from the emitting levels of Pr^{3+} is a commonly observed phenomenon and because of that it has been a challenge to optimize the luminescence efficiency resulting from transitions in these levels. It is therefore very important to further investigate the luminescent properties of Pr^{3+} at different host matrices. In that case, we can also investigate ways of optimizing the luminescence efficiency originating from different emitting levels of Pr^{3+} . Furthermore, it would be interesting to investigate up-conversion luminescent properties of Pr^{3+} when is co-doped with other rare earth ions or directly doped into quantum dots.

To fully understand why Pr^{3+} acts as a quenching centre for many trivalent rare earth ions emission, it would be important to first investigate if there is any energy transfer between Pr^{3+} and that particular ion. Theoretical energy transfer expressions can be used to calculate the kind of interaction taking place between the two ions. Otherwise, Pr^{3+} can be co-doped with transition metals in a search for energy transfer partner of Pr^{3+} .

PUBLICATIONS

- *G.H. Mhlongo*, M.S. Dhlamini, O. M. Ntwaeaborwa, K. T. Hillie. Dependence of photoluminescence (PL) emission intensity on Eu^{3+} and ZnO concentrations in $\text{Y}_2\text{O}_3:\text{Eu}^{3+}$ and $\text{ZnO}:\text{Y}_2\text{O}_3:\text{Eu}^{3+}$ nanophosphors. *J. Opt. Mater.* 33 (2011) 1495-1499.
- *G.H. Mhlongo*, O.M. Ntwaeaborwa, M.S. Dhlamini, H.C. Swart and K.T. Hillie. Effects of Ce^{3+} concentration, beam voltage and current on the Cathodoluminescence intensity of $\text{SiO}_2:\text{Pr}^{3+}-\text{Ce}^{3+}$ nanophosphor. *J. Alloys Compd.* 509 (2011) 2986-2992
- M.S. Dhlamini, *G.H. Mhlongo*, H.C. Swart, K.T. Hillie. Energy transfer between doubly doped Er^{3+} , Tm^{3+} , and Ho^{3+} rare earth ions in SiO_2 nanoparticles. *J. Lumin.* 131 (2011) 790-794
- *G.H. Mhlongo*, O.M. Ntwaeaborwa, M.S. Dhlamini, H.C. Swart, K.T. Hillie, Cathodoluminescence properties of $\text{SiO}_2:\text{Pr}^{3+}$ and $\text{ZnO}:\text{SiO}_2:\text{Pr}^{3+}$ phosphor powders. *J. Mater. Sci.* (2010) 45:5228-5236
- M.S. Dhlamini, *G.H. Mhlongo*, K.T. Hillie. Effects of accelerating beam voltage on luminescence of Er^{3+} and Tm^{3+} doped SiO_2 phosphor prepared by sol-gel process. *Opt. Mater.* 33 (2010) 79-83
- *G. H. Mhlongo*, O. M. Ntwaeaborwa, H. C. Swart, R. E. Kroon, P. Solarz, W. Ryba-Romanowski, K. T. Hillie. Luminescence dependence of Pr^{3+}

activated SiO₂ nanophosphor on Pr³⁺ concentration, temperature and ZnO incorporation. *J. Phys. Chem. B*, *accepted*

- *G.H. Mhlongo*, M.S. Dhlamini, O.M. Ntwaeaborwa, H.C. Swart, P. Solarz, W. Ryba-Romanowski, K.T. Hillie. The influence of Pr³⁺ co-doping on the photoluminescence and cathodoluminescence properties of SiO₂:Eu³⁺/Tb³⁺. *In progress*.

INTERNATIONAL CONFERENCES

- **G.H Mhlongo**, O.M. Ntwaeaborwa, and T. K. Hillie.
PL properties of Y₂O₃:Eu³⁺ nanopowders synthesized by sol gel method.
The 5th International Conference on Semiconductor Quantum Dots-11-16
May 2008, Gyeongju, Korea.
- **G.H Mhlongo**, O.M. Ntwaeaborwa, M.S Dhlamini, H.C Swart, K.T Hillie.
1. Cathodoluminescence degradation of SiO₂:Pr³⁺-Eu³⁺ nanophosphor and quenching of Pr³⁺ (³H₆→³P₀) emission due to Eu³⁺ co-doping.
- **G.H Mhlongo**, O.M. Ntwaeaborwa, K.T Hillie
2. Fluorescence properties of sol-gel derived nanoparticulate ZnO. Y₂O₃:Eu³⁺ powder phosphors.
Excited States of Transition Elements and Workshop on Luminescence.
04-09 September 2010, Wroclaw, Poland.

NATIONAL CONFERENCES

- **G H Mhlongo**, M S Dhlamini, O M Ntwaeaborwa, H C Swart, P Solarz, W Ryba-Romanowski, K T Hillie
1. The influence of Pr³⁺ co-doping on the photoluminescence and cathodoluminescence properties of SiO₂:Eu³⁺/Tb³⁺.
- **G H Mhlongo**, M S Dhlamini, O M Ntwaeaborwa, H C Swart, R.E Kroon, P Solarz, W Ryba-Romanowski, K T Hillie.
2. Effects of ZnO and Ce³⁺ incorporation on the photoluminescence and cathodoluminescence intensity of Pr³⁺ doped SiO₂.
56th Annual Conference of the South African Institute of Physics (SAIP) conference, 13 to 15 July 2011, Univ. of South Africa (UNISA).
- 54th Annual Conference of the South African Institute of Physics (SAIP) conference, October 2010, National Laser Centre.
In attendance
- International Workshop on Advanced Materials and Technologies for global Energy and Environmental challenges, 6-8 December 2010, CSIR
In attendance
- **G.H Mhlongo**, O.M. Ntwaeaborwa, K.T Hillie.
Luminescence enhancement of Pr³⁺ doped SiO₂ silica glass by energy transfer from ZnO nanoparticles.

54th Annual Conference of the South African Institute of Physics (SAIP)
conference, 06 to 10 July 2009, Univ. of Kwa-Zulu Natal.

- **G.H Mhlongo**, O. M Ntwaeaborwa, T.K Hillie

Optical properties and energy transfer of the sol-gel derived rare earths
nanophosphors.

3rd NanoAfrica conference, 1-4 February 2009, CSIR

- **G.H Mhlongo**, S. Mohlala, O.M. Ntwaeaborwa, K.T Hillie.

PL properties of $\text{Y}_2\text{O}_3:\text{Eu}^{3+}$ nanopowders synthesized by sol-gel method.

53rd Annual Conference of the South African Institute of Physics (SAIP)
conference, 08 to 11 July 2008, Univ. of Limpopo.